# Computational advances and challenges in simulations of turbulence and star formation

Christoph Federrath  $^{1*}$  and Stella Offner  $^{2\dagger}$ 

1\*Research School of Astronomy and Astrophysics, Australian National University, Cotter Road, Canberra, 2611, ACT, Australia.
 2Astronomy Department, The University of Texas at Austin, 2515
 Speedway, Stop C1400, Austin, 78712-1205, TX, USA.

\*Corresponding author(s). E-mail(s): christoph.federrath@anu.edu.au; Contributing authors: soffner@astro.as.utexas.edu; †These authors contributed equally to this work.

#### Abstract

We review recent advances in the numerical modeling of turbulent flows and star formation. An overview of the most widely used simulation codes and their core capabilities is provided. We then examine methods for achieving the highest-resolution magnetohydrodynamical turbulence simulations to date, highlighting challenges related to numerical viscosity and resistivity. State-of-the-art approaches to modeling gravity and star formation are discussed in detail, including implementations of star particles and feedback from jets, winds, heating, ionization, and supernovae. We review the latest techniques for radiation hydrodynamics, including ray tracing, Monte Carlo, and moment methods, with comparisons between the flux-limited diffusion, moment-1, and variable Eddington tensor methods. The final chapter summarizes advances in cosmic-ray transport schemes, emphasizing their growing importance for connecting small-scale star formation physics with galaxy-scale evolution.

 $\textbf{Keywords:} \ \text{fluid dynamics, high performance computing, magnetic fields, numerical methods, star formation, turbulence}$ 

# Contents

1	Introduction 4									
	1.1	Numerical codes for turbulence and star formation								
	1.2	Parallel scalability and code optimization								
2	Hvd	rodynamics and boundary conditions 7								
_	2.1	Magnetohydrodynamics (MHD)								
		2.1.1 MHD equations								
		2.1.2 Thermodynamics and equation of state								
	2.2	Initial and boundary conditions								
3	Tur	bulence 11								
•	3.1	Challenges in modeling turbulent flows								
	3.2	Turbulence initialization and driving								
	3.3	Physical shear and bulk viscosity								
	3.4	Sub-resolution models for turbulence								
	0.4	3.4.1 Numerical viscosity and resistivity								
		3.4.2 Local kinetic energy dissipation rate								
	3.5	Numerical advances and challenges								
	0.0	3.5.1 Positivity-preserving schemes								
		3.5.2 Hybrid precision								
		3.5.3 GPU acceleration								
	26	Summary of challenges and future directions								
	3.6 Summary of challenges and future directions									
4	Gra									
	4.1	Discrete mass distributions								
	4.2	Continuous mass distributions								
	4.3	Combining the gravitational effects of gas and stars								
	4.4	Methods for solving the Poisson equation								
		4.4.1 FFT methods								
		4.4.2 Multi-grid methods								
		4.4.3 Tree-based methods								
	4.5	Summary of challenges and future directions								
5	Star	formation 27								
	5.1	Jeans resolution criterion								
	5.2	Star particles								
		5.2.1 Sink particle formation								
		5.2.2 Sink particle accretion								
		5.2.3 Sink particle dynamics								
		5.2.4 Sink particle merging								
	5.3	Summary of challenges and future directions								
6	Stel	lar feedback 34								
-	6.1	Stellar and protostellar evolution								

R	References								
9	Cor	nclusions	68						
	8.5	Summary of challenges and future directions	68						
	8.4	Monte Carlo CR transport	67						
	8.3	Multi-bin spectral formalisms	66						
		8.2.2 Two-moment methods	65						
		8.2.1 One-moment methods	64						
	8.2	Moment methods for CRHD	63						
	8.1	Uncertainties in CR propagation	62						
8	Cos	mic-ray hydrodynamics (CRHD)	61						
	7.7	Summary of challenges and future directions	61						
	7.6	Comparison of RT methods	59						
	7.5	Monte Carlo radiation transfer	59						
		7.4.5 Variable Eddington tensor (VET) method	57						
		7.4.4 Moment-1 (M1) closure	55						
		7.4.3 Flux-limited diffusion (FLD)	54						
		7.4.2 Complete set of RHD moment equations	53						
		7.4.1 Moments of the radiation transport equation	51						
	7.4	Moment methods	51						
	7.3	Ray-based methods	50						
		7.2.2 Time-independent radiation transfer	49						
	2	7.2.1 Time-dependent radiation transfer	48						
	7.2	Basic equations of radiation transfer	48						
		7.1.2 Laboratory, co-moving, and mixed reference frames	48						
	1.1	7.1.1 Opacities	47						
1	7.1	Optically-thin vs. optically-thick regimes	46						
7	Dod	liation hydrodynamics	46						
	6.7	Summary of challenges and future directions	45						
	6.6	Supernova feedback	44						
	6.5	Ionization feedback	44						
	6.4	Stellar wind feedback	43						
	6.3	Protostellar heating feedback	40						
		6.2.6 Comparison of jet/outflow implementations	40						
		6.2.5 Implementation, code validation, and access	39						
		6.2.4 Outflow angular momentum transfer	38						
		6.2.2 Outflow mass transfer	$\frac{36}{38}$						
		6.2.1 Geometry of the outflow launching region	36						
	6.2	Protostellar jet and outflow feedback	35						
	6.0	Durate et allem interest and another of allem in	25						

## 1 Introduction

Star formation is a critical component of many astrophysical phenomena: the life cycle of stars drives the formation and evolution of galaxies, regulates the abundance and distribution of metals in the Universe, and sets the initial conditions for planet formation. Despite being governed by fundamentally 'classical' physics processes—magnetized gas dynamics, gravity, thermodynamics, and radiation—the complex, nonlinear interactions defy analytic description. Star formation also spans vast spatial scales, from the kpc interstellar medium (ISM) down to stellar radii, and occurs across regimes ranging from ultra-low densities, approaching laboratory vacuum limits, to stellar densities. Observations are further limited by resolution, sensitivity, and optical depth effects. Consequently, numerical simulations powered by high-performance computing have become indispensable tools for studying star formation.

Over the past decade, numerical developments have greatly expanded the scope of star formation studies by extending dynamic range, improving computational efficiency, and introducing new methods. Modern codes now routinely resolve gas dynamics across many orders of magnitude in scale while incorporating key physical processes. This has yielded important insights into how these processes shape central metrics such as the star formation rate (SFR) and the initial mass function (IMF). Despite these advances, major challenges remain. Current simulations still fall short of achieving the physical parameters associated with magnetized turbulence, or of spanning the full range of scales required to capture both individual star formation and the impact of stellar feedback. The long timescales (>Myr) and stochastic nature of star formation demand large computational domains evolved over many timesteps. Moreover, the interplay between large and small scales calls for holistic approaches in which physics and chemistry across wide ranges are modeled simultaneously, with minimal sensitivity to initial and boundary conditions.

Numerical advances over the past decade have focused on developing magneto-hydrodynamical (MHD) methods (Sect. 2) that robustly capture high-Mach number turbulence—a cornerstone of the star-formation process (Sect. 3). A second fundamental requirement is modeling the gravity of gas and stars (Sect. 4). Despite significant progress, simulations still rely heavily on prescriptions for unresolved physics, so-called *sub-resolution* models<sup>1</sup>. These encompass treatments of dissipation and unresolved turbulence, star formation itself (Sect. 5), and a variety of stellar feedback processes—stellar evolution, protostellar jets and outflows, heating, winds, ionization, and supernovae. Such models often depend on ad-hoc parameters and remain among the least benchmarked areas of development (Sect. 6). Other important advances include more accurate radiative transfer methods coupled to MHD, which can capture shadows and remain valid across the difficult transition between optically thin and thick regimes (Sect. 7). Finally, growing recognition of the role of cosmic rays has driven the development of cosmic-ray transport (CRT) methods (Sect. 8).

In this review we present new approaches to modeling turbulence, gravity, star formation, feedback, radiation, and cosmic rays, with a particular focus on code capabilities, their numerical treatments, and parameterizations. We assess the strengths

 $<sup>^{1}</sup>$ Sometimes referred to as 'sub-grid' models; however, the term 'sub-resolution' is more general and includes particle-based methods.

and weaknesses of these methods and highlight current limitations. The remainder of the Introduction lists the codes most widely applied in turbulence and star-formation studies (Sect. 1.1) and highlights recent advances in code optimization and parallel scaling (Sect. 1.2).

## 1.1 Numerical codes for turbulence and star formation

Over the past two decades, more than a dozen powerful codes for turbulence and star-formation applications have been developed and continuously refined. Table 1 summarizes the most widely used codes and their capabilities. These methods can be broadly divided into two categories: *grid* methods, which discretize flows by volume, and *particle* methods, which discretize flows by mass. Grid-based approaches typically model hydrodynamics using elements fixed in the reference frame of a stationary observer, while particle-based approaches adopt a Lagrangian framework, with mass elements moving with the fluid. Hybrid approaches, such as moving-mesh and meshless finite mass/volume methods, aim to combine the strengths of both.

Most of these codes have publicly available versions, promoting transparency and broad community use. Links to the available releases are provided in the Table notes. However, not all features listed in Table 1 are implemented in the public versions.

## 1.2 Parallel scalability and code optimization

Although physical and numerical accuracy are paramount, efficient parallel scaling to large core counts is also essential to perform high-resolution simulations within practical computational budgets. Strong scaling tests evaluate the time-to-solution for fixed problem sizes: the total amount of calculation 'work' remains constant as the number of cores is increased. Weak scaling tests increase the problem size and resolution proportionally with the number of compute cores, i.e., the amount of work per core is fixed. Good strong and weak scaling performance are both essential for advancing astrophysical applications, while also ensuring environmentally responsible use of supercomputing resources. Continuous code optimization and scaling improvements are therefore indispensable, for example, through the development of optimized techniques for load balancing (e.g., DISPATCH; see Nordlund et al. 2018).

Figure 1 highlights some of the recent developments in code optimization and weak scaling in three of the codes listed in Table 1. Good weak scaling performance is particularly relevant for turbulence and star-formation simulations, where higher resolution, and thus larger problems, is always desired. Because the tests in Fig. 1 involve different setups, physics, and machines, only the relative speed-up for a given code can be directly compared.

Overall, all three codes show excellent parallel efficiency up to thousands or even tens of thousands of cores. For pure MHD, both athena<sup>++</sup> and flash retain efficiencies above 90% up to  $10^4$ – $10^5$  cores, i.e., very close to ideal scaling. Even the more challenging are tests, which combine hydrodynamics, self-gravity, and radiation transport (RT) (Zier et al. 2024), achieve 60–70% efficiency up to nearly 5,000 cores—impressive given the inherently non-local nature of gravity (Sect. 4) and RT (Sect. 7).

Table 1 Popular astro-simulation codes used for turbulence and star formation modeling.

Name	Type	Hydro	Self-Gravity	Feedback	Radiation	CRT
(1)	(2)	(3)	(4)	(5)	(6)	(7)
AREPO <sup>1</sup>	MM	NI	TPM	R/S	M1/RT/MC	<u> </u>
$ART^2$	AMR	Η	FFT/MG	R/W/S	OT-VET	1
$ATHENA^3$	UG/SMR	NI	FFT/MG	X	M1/RT	X
ATHENA <sup>++4</sup>	AMR	NI	FFT/MG	×	VET	/
$ENZO^5$	AMR	I	FFT/MG	R/S	FLD/RT	1
$FLASH^6$	AMR	NI	FFT/MG/TPM	O/R/S	FLD/M1/VET/RT/MC	1
$GADGET^7$	SPH	I	TPM	R/S	OT-VET/RT	1
$\rm GIZMO^8$	MLFMV	NI	TPM	O/R/W/S	FLD/M1/OT-VET/RT	/
IDEFIX <sup>9</sup>	$\overline{\mathrm{UG}}$	NI	$_{ m MG}$	X	×	X
NIRVANA <sup>10</sup>	AMR	NI	MG	×	×	X
$ORION^{11}$	AMR	I	MG	O/R/W	FLD/RT	X
PENCIL <sup>12</sup>	$\overline{\mathrm{UG}}$	NI	FFT	$\mathbf{S}$	RT	1
$PHANTOM^{13}$	SPH	NI	TPM	R/W/S	FLD/MC	X
$PLUTO^{14}$	AMR	NI	×	X	M1/RT	/
$QUOKKA^{15}$	AMR	H	$_{ m MG}$	$\mathbf{S}$	M1	X
RAMSES <sup>16</sup>	AMR	NI	$_{ m MG}$	O/R/W/S	M1	1
SEREN <sup>17</sup>	SPH	H	TPM	R/S	FLD/RT	X
TORUS <sup>18</sup>	AMR	H	$_{ m MG}$	R/W/S	$\overline{MC}$	X
ZEUS <sup>19</sup>	UG	NI	×	X	VET	X

Notes: Column 1: code name. Column 2: code type: UG = uniform grid, SMR = static mesh refinement, AMR = adaptive mesh refinement (Berger and Colella 1989) (includes UG capability), SPH = smoothed particle hydrodynamics (e.g., Benz 1988; Monaghan 1988; Price et al. 2018), MM = moving mesh, MLFMV = mesh-less finite mass/volume (Hopkins 2013a). Column 3: type of gas dynamics: H = hydrodynamics, I = ideal MHD (includes H capability), NI = non-ideal MHD (Ohmic dissipation, ambipolar diffusion, Hall effect; or all three; includes I capability). Column 4: self-gravity treatment: FFT = fast Fourier transform (Sect. 4.4.1), MG = multi-grid (Sect. 4.4.2), TPM = tree particle-mesh (Sect. 4.4.3). Column 5: feedback processes: O = protostellar outflows (Sect. 6.2), R = radiative feedback in the form of pressure, ionization and/or heating (Sect. 6.3), W = stellar winds (Sect. 6.4, 6.5), and S = supernova feedback (Sect. 6.6). Column 6: radiation transfer methods: FLD = fluxlimited diffusion (Sect. 7.4.3), M1 = moment-1 (Sect. 7.4.4), VET = variable Eddington tensor (Sect. 7.4.5), OT-VET = optically-thin VET, RT = ray tracing (Sect. 7.3), MC = Monte Carlo (Sect. 7.5). Column 7: cosmic ray transport (CRT; Sect. 8). A ✓ indicates availability of a certain functionality (without specifying further details), while X indicates missing functionality. References/Links: 1 https://gitlab.mpcdf.mpg.de/vrs/arepo (Springel 2010), <sup>2</sup>https://bitbucket.org/cartamr/cart/src/master (Kravtsov et al. 1997, 2002; Rudd et al. 2008), <sup>3</sup>https://princetonuniversity.github.io/Athena-Cversion, <sup>4</sup>https://www.athena-astro.app (Stone et al. 2020), <sup>5</sup> https://github.com/enzo-project (Bryan et al. 2014), <sup>6</sup>https://flash.rochester.edu/ site/flashcode (Fryxell et al. 2000; Dubey et al. 2008), <sup>7</sup>https://wwwmpa.mpa-garching.mpg. de/gadget4, 8https://github.com/pfhopkins/gizmo-public(Hopkins 2015), 9 https://github.com/ idefix-code/idefix (Lesur et al. 2023), <sup>10</sup>https://gitlab.aip.de/ziegler/NIRVANA(Ziegler 2008), <sup>11</sup>Li et al. (2021), <sup>12</sup>Pencil Code Collaboration et al. (2021), <sup>13</sup>https://phantomsph.github.io (Price et al. 2018), <sup>14</sup>https://plutocode.ph.unito.it, <sup>15</sup>https://github.com/quokka-astro/quokka (Wibking and Krumholz 2022), <sup>16</sup>https://github.com/ramses-organisation/ramses (Teyssier 2002), <sup>17</sup>Hubber et al. (2011a,b), <sup>18</sup>Harries et al. (2019), <sup>19</sup>https://www.astro.princeton.edu/ ~jstone/zeus.html (Stone and Norman 1992).

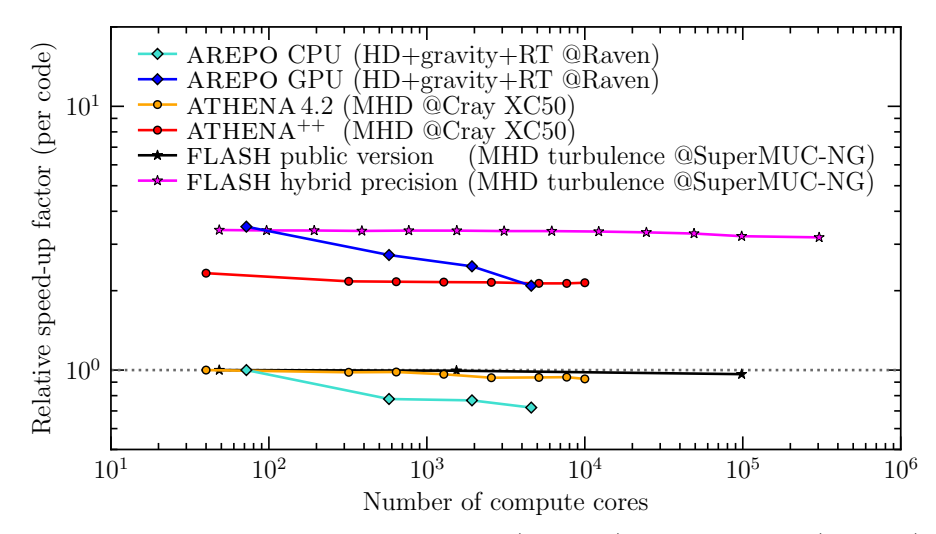


Fig. 1 Weak-scaling tests for three codes: AREPO (diamonds), comparing CPU (turquoise) and GPU (blue) implementations of radiation transport (RT) in simulations including hydrodynamics and gravity, run on the 'Raven' system; ATHENA (circles), comparing ATHENA 4.2 (orange) with the modernized ATHENA++ (red) for pure MHD on a Cray XC50; and FLASH (stars), comparing the public version (black) with an optimized hybrid-precision version (magenta; Sect. 3.5.2) for MHD turbulence on 'SuperMUC-NG'. For each code, the two modes shown are directly comparable (but not across different codes). Substantial performance gains are evident: GPU acceleration (AREPO), code modernization (ATHENA), and hybrid precision (FLASH).

The individual comparisons further illustrate substantial performance gains from recent developments. Accelerating RT in AREPO with GPUs (see also Sect. 3.5.3 below) yields an overall speed-up of  $3\text{--}4\times$ , with the RT component itself running  $\sim 15\times$  faster on GPUs. Modernization of ATHENA improves performance by  $\sim 2.3\times$  from version 4.2 to ATHENA<sup>++</sup> (Stone et al. 2020). In FLASH, switching from the public version to an optimized hybrid-precision implementation (see details in Sect. 3.5.2 below) produces a  $\sim 3.3\times$  speed-up for MHD turbulence, while retaining efficiency to more than  $10^5$  cores.

These results demonstrate how continuous algorithmic and implementation improvements translate directly into higher scientific throughput. Such efforts are critical not only for enabling frontier simulations but also for maximizing the efficient and sustainable use of supercomputing resources. Future updates of this living review will include controlled scaling benchmarks for additional codes listed in Table 1, extending earlier comparative studies (Kitsionas et al. 2009; Price and Federrath 2010; Kritsuk et al. 2011).

## 2 Hydrodynamics and boundary conditions

Here we introduce the basic set of MHD equations (Sect. 2.1), which provide the foundation for the remainder of the review, and we discuss challenges associated with the choice of initial and boundary conditions for star-formation simulations (Sect. 2.2).

## 2.1 Magnetohydrodynamics (MHD)

Astrophysical fluids generally have magnetic fields. While magnetic fields couple only to charged particles, even phases of the ISM such as molecular clouds (where stars form), composed almost entirely of neutral gas, retain a small degree of ionization (ionization fraction  $\sim 10^{-7}$ ). This is sufficient to generate electric currents, and through frequent collisions the ions strongly couple to the neutrals, making magnetic fields a critical component of the gas dynamics. Magnetic fields introduce additional physical processes, including magnetic pressure, tension, MHD waves, and resistive dissipation. Owing to this complexity, many early star-formation simulations neglected magnetic fields, but their crucial role is now widely recognized, and most current simulations include them.

A fully self-consistent description of magnetized systems requires kinetic theory and particle-in-cell (PIC) simulations (e.g., St-Onge and Kunz 2018; Rincon et al. 2016; Chirakkara et al. 2024). This can, however, be reduced to a coupled set of fluid equations in which electrons, ions (protons, atomic and molecular ions), and neutrals (e.g., H, H<sub>2</sub>, CO) are treated as separate fluids—the framework usually referred to as 'non-ideal MHD'<sup>2</sup>. Some studies follow this so-called 'multi-fluid' approach (Li et al. 2008, 2012; Burge et al. 2016; Tritsis et al. 2022, 2025a,b). More commonly, however, strong ion-neutral coupling is assumed, yielding the 'ideal MHD' limit, which is well justified on cloud and core scales, though it breaks down in dense accretion disks (see e.g., Xu and Kunz 2021a,b; Mauxion et al. 2024).

Unlike most turbulence studies, star-formation simulations, to the best of current knowledge, consistently neglect explicit dissipation. By contrast, MHD turbulence studies frequently include viscosity and at least Ohmic resistivity, as we do in the following equations. Even studies that omit explicit viscosity and resistivity inevitably introduce effective small-scale viscosity and resistivity through numerical diffusion, leading to partial ion-neutral decoupling. We will examine these effects in detail in Sect. 3. With these foundations, we can now introduce the standard set of MHD equations.

#### 2.1.1 MHD equations

The standard compressible MHD equations including viscous and resistive dissipation terms can be written as

$$\frac{\partial \rho}{\partial t} = -\nabla \cdot (\rho \mathbf{v}),\tag{1}$$

$$\frac{\partial \rho}{\partial t} = -\nabla \cdot (\rho \mathbf{v}), \tag{1}$$

$$\frac{\partial (\rho \mathbf{v})}{\partial t} = -\nabla \cdot \left( \rho \mathbf{v} \mathbf{v} - \frac{1}{4\pi} \mathbf{B} \mathbf{B} \right) - \nabla p + \nabla \cdot (2\rho \nu \mathbb{S}), \tag{2}$$

$$\frac{\partial (\rho e)}{\partial t} = -\nabla \cdot \left[ (\rho e + p) \mathbf{v} - \frac{1}{4\pi} (\mathbf{B} \cdot \mathbf{v}) \mathbf{B} \right]$$

 $<sup>^2</sup>$ Non-ideal MHD is commonly divided into three categories: (i) Ohmic resistivity, (ii) ambipolar diffusion, and (iii) the Hall effect. In this review, we include only Ohmic resistivity in the MHD equations. For a comprehensive review of non-ideal MHD methods relevant to star formation, see Teyssier and Commerçon (2019). We further note that non-ideal MHD effects are tied to magnetic reconnection events, where codes primarily rely on numerical diffusion to approximate physical reconnection (see discussion in the review by Lazarian et al. 2020)

$$+\nabla \cdot \left[2\rho\nu\mathbb{S}\mathbf{v} + \frac{1}{4\pi}\mathbf{B} \times (\eta\nabla \times \mathbf{B})\right],$$
 (3)

$$\frac{\partial \mathbf{B}}{\partial t} = \nabla \times (\mathbf{v} \times \mathbf{B}) + \eta \nabla^2 \mathbf{B},\tag{4}$$

$$\nabla \cdot \mathbf{B} = 0. \tag{5}$$

Here,  $\rho$ ,  $\mathbf{v}$ ,  $p = p_{\rm th} + |\mathbf{B}|^2/(8\pi)$ ,  $\mathbf{B}$ , and  $\rho e = \rho e_{\rm int} + \rho |\mathbf{v}|^2/2 + |\mathbf{B}|^2/(8\pi)$  denote the gas density, velocity, pressure (thermal + magnetic), magnetic field, and total energy density (internal + kinetic + magnetic), respectively. Physical shear viscosity (kinematic viscosity  $\nu$ ) in Eqs. (2) and (3) is included via the traceless rate-of-strain tensor,

$$\mathbb{S} = \frac{1}{2} \left( \nabla \mathbf{v} + (\nabla \mathbf{v})^{\mathrm{T}} \right) - \frac{1}{3} \left( \nabla \cdot \mathbf{v} \right) \mathbb{I}, \tag{6}$$

where  $\mathbb{I}$  is the identity matrix. In index notation, the components of  $\mathbb{S}$  are  $\mathbb{S}_{ij} = (1/2)(\partial_i v_j + \partial_j v_i) - (1/3)(\partial_k v_k)\delta_{ij}$ . The product  $\rho\nu$  appearing in Eqs. (2) and (3) is commonly referred to as the 'dynamic viscosity'.

The evolution and diffusion of **B** are governed by the induction equation (Eq. 4), where the magnetic diffusivity is  $\eta = 1/(4\pi\sigma)$  with  $\sigma$  the electric conductivity. Finally, we note that Eqs. (2) and (3) only include the shear viscosity  $\nu$ , while the bulk viscosity is usually assumed to vanish—see Sect. 3.3 for further discussion.

## 2.1.2 Thermodynamics and equation of state

The MHD equations are closed with an equation of state (EOS). Most commonly this is the ideal gas EOS,

$$p_{\rm th} = \rho e_{\rm int}(\gamma - 1) = \frac{\rho k_{\rm B} T}{\mu m_{\rm H}},\tag{7}$$

where T is the temperature,  $k_{\rm B}$  the Boltzmann constant,  $m_{\rm H}$  the mass of a hydrogen atom,  $\mu$  the mean particle mass in units of  $m_{\rm H}$ , and  $\gamma$  the adiabatic index. The latter is given by  $\gamma = 1 + 2/f$ , where f is the number of degrees of freedom excited for a given particle type (electrons, atoms/ions, or molecules), which always includes translational modes, and may include rotational or vibrational modes for molecules (if they are excited; see e.g., Sharda et al. 2019). The sound speed is

$$c_{\rm s} = \left(\frac{\partial p_{\rm th}}{\partial \rho}\right)_s^{1/2} = \left(\frac{\gamma k_{\rm B} T}{\mu m_{\rm H}}\right)^{1/2},\tag{8}$$

where the subscript s denotes that the derivative is taken at constant entropy.

For simplicity, fundamental studies of MHD turbulence often assume an isothermal EOS,  $p_{\rm th} = \rho c_{\rm s}^2$ , with a constant  $c_{\rm s}$  fixed in space and time. This is a good approximation for molecular cloud turbulence and for the early stages of dense core formation (Wolfire et al. 1995; Omukai et al. 2005; Pavlovski et al. 2006; Glover and Mac Low 2007a,b; Glover et al. 2010). More sophisticated treatments include heating and cooling via radiative transfer (RT; Sect. 7), which is crucial to capture the transition to optically thick gas at number densities  $n = \rho/(\mu m_{\rm H}) \gtrsim 10^{10} \, {\rm cm}^{-3}$ , where the gas

heats up and fragmentation is suppressed (Jappsen et al. 2005; Guszejnov et al. 2016; Federrath et al. 2017; Guszejnov et al. 2018; Mathew and Federrath 2020; Hennebelle et al. 2020, 2022).

Intermediate approaches lie between assuming an isothermal EOS and solving full RT. One common choice is a polytropic EOS of the form  $p_{\rm th} = K \rho^{\Gamma}$  (Passot and Vázquez-Semadeni 1998; Li et al. 2003), with polytropic index  $\Gamma$  and coefficient K. These can be specified as piecewise functions to approximate the heating of gas as it becomes optically thick (see eqs. 3 and 4 in Federrath et al. 2014b). In this case the energy equation (Eq. 3) can be omitted, since the MHD system is closed without it. Other strategies include incorporating approximations for stellar heating (Sect. 6.3) or adding heating/cooling terms to Eq. (3) from pre-computed tables (Koyama and Inutsuka 2002; Vázquez-Semadeni et al. 2007; Mandal et al. 2020).

## 2.2 Initial and boundary conditions

A recurring issue in simulations of star formation is the interconnection of physical processes across vastly different scales. This coupling operates in both directions: large-scale dynamics can strongly influence the evolution of star formation on small scales, while feedback from stars can in turn affect the large-scale environment. This poses a severe challenge, as we would ideally like to include all relevant length and time scales in order to solve the star formation problem self-consistently—that is, starting from a much larger scale (e.g., the scale of an entire galaxy, or at least a significant patch thereof) than the one we ultimately wish to resolve, such as a forming star cluster, while simultaneously capturing the effects of the galactic environment and feedback from nearby star-forming regions. Achieving this at the maximum possible resolution to ensure numerical convergence and robustness of the results remains elusive with current numerical methods and supercomputing capabilities. Therefore, all calculations must adopt approximations, both in terms of the initial conditions and the boundary conditions.

Popular techniques for initializing a star formation simulation include placing a uniform sphere of gas with a chosen radial density profile (e.g., Bate et al. 2003; Federrath et al. 2010a; Girichidis et al. 2011, 2012b,a) in a box with isolated boundary conditions for hydrodynamics and gravity, and adding a turbulent velocity field at the start to promote the formation of structure reminiscent of molecular clouds. Another common approach models a sub-volume of a molecular cloud with periodic boundary conditions and drives turbulence with an idealized energy injection mechanism (Klessen et al. 2000; Jappsen et al. 2005; Federrath and Klessen 2012; Krumholz et al. 2012; Guszejnov et al. 2022; Mathew et al. 2023, e.g.,). Both techniques have advantages and disadvantages: although real molecular clouds are neither truly periodic nor completely isolated from the surrounding ISM, some approximation in boundary conditions is unavoidable. Moreover, since turbulence decays on roughly a crossing time (Stone et al. 1998; Mac Low 1999), some form of continuous driving is required to sustain realistic turbulent motions.

A recent method combines the advantage of continuous turbulence driving with the ability to use isolated gas and gravity boundaries by imposing an external gravitational potential that confines the cloud during the driving phase (Lane et al. 2022). This

and the aforementioned idealized approaches allow for controlled parameter studies, as properties such as the sonic Mach number, mean density, and size of the target cloud or region can be set explicitly via the initial conditions. However, these methods still suffer from artificial boundary and initial conditions<sup>3</sup>.

Finally, a method that avoids the use of artificial turbulence driving altogether involves initializing the simulation on a much larger scale than the ultimate scale of interest, and then 'zooming in' on that region by selectively adding higher resolution elements or by re-simulating an extracted subdomain. This technique has been employed for both large-scale cloud simulations of star formation (e.g., Zamora-Avilés and Vázquez-Semadeni 2014; Seifried et al. 2017; Ibáñez-Mejía et al. 2017; Kim and Ostriker 2017; Grisdale et al. 2018; Vázquez-Semadeni et al. 2019; Haid et al. 2019; Zhao et al. 2024; Hopkins et al. 2024; Pillsworth et al. 2025), as well as for smallerscale simulations of individual accretion disks (e.g., Offner et al. 2009; Kuffmeier et al. 2017; Bate 2018; Lebreuilly et al. 2021; He and Ricotti 2023; Yang and Federrath 2025; Mayer et al. 2025). Ideally, once the zoom-in region is sufficiently refined, the scales of interest are far enough removed from the numerical boundaries of the parent simulation that boundary effects are negligible within the region of interest, allowing for re-simulation of this subregion. In the case of zoom-ins, the high-resolution region is no longer treated as isolated and it continues to exchange mass and energy with the larger environment via accretion and feedback effects as it evolves. Likewise, the initial conditions are more 'natural' in this approach, as they emerge self-consistently from the larger-scale flows in the parent simulation, such as from the formation of the dense, collapsing part of the cloud itself. While this is certainly a more realistic approach to initializing a star-formation simulation, it comes at the cost of making parameter studies considerably harder, as there is little direct control over the cloud parameters, apart from selecting different zoom-in regions from the larger parent simulation.

## 3 Turbulence

Turbulence is a fundamental ingredient of star formation, with its properties shaping the structure and dynamics of molecular clouds, the birthplaces of stars (Scalo and Elmegreen 2004; Elmegreen and Scalo 2004; Mac Low and Klessen 2004; McKee and Ostriker 2007; Hennebelle and Falgarone 2012; Padoan et al. 2014). The statistical nature of turbulent gas, including MHD (e.g., Beresnyak and Lazarian 2019), its density probability distribution function and power spectra, provides essential input for theories of the star formation rate (SFR) (Krumholz and McKee 2005; Padoan and Nordlund 2011; Hennebelle and Chabrier 2011; Federrath and Klessen 2012; Burkhart 2018; Hennebelle et al. 2024) and the stellar initial mass function (IMF) (Padoan and Nordlund 2002; Hennebelle and Chabrier 2008, 2009, 2011, 2013; Hopkins 2012, 2013b; Guszejnov et al. 2017; Lee et al. 2020). Capturing turbulence is therefore critical for numerical simulations of star formation, and we begin this review by examining the main challenges and current state-of-the-art in turbulence modeling.

<sup>&</sup>lt;sup>3</sup>Periodic boundary conditions may appear particularly unrealistic, but given the large spatial extent of the ISM in a galaxy, a cloud patch of a few parsecs in size can be regarded as a specific realization of a much larger turbulent medium. In this sense, periodic boundaries can be viewed as mimicking the tidal effects and gas flows induced by surrounding, similar cloud regions.

## 3.1 Challenges in modeling turbulent flows

Using  $N_{\rm Re}=1.5$  and  $p_{\rm Re}=4/3-3/2$ , we find Re  $\sim (2.7-5.4)\times 10^2$ ,  $(8.5-17)\times 10^3$ , and  $(1.2-5.4)\times 10^5$  for N=100, 1,000, and 10,000, respectively. Thus, fully turbulent flows with Re  $\gtrsim 1,000$  require  $N\gtrsim 270$ . Much higher resolution is necessary, however, to establish a turbulent cascade with sufficient dynamic range to measure inertial-range statistics such as scaling exponents and correlation functions.

The primary challenge in modeling supersonic turbulence lies in capturing the dynamic range required to achieve fully-developed turbulent flows — that is, to reproduce the self-similar characteristics and statistics of turbulence across the relevant density, velocity, and spatial scales. For molecular clouds, the turbulence spans more than six orders of magnitude in scale, from the cloud size of  $\sim 10{\text -}100\,\mathrm{pc}$  down to the dissipation scale around  $\sim 1\,\mathrm{AU}$  inside protostellar accretion disks. Importantly, this may not be a single universal 'cascade' (or spectrum) — although often approximated as such — because different energy injection mechanisms can drive turbulence on different scales within molecular clouds. Turbulence continues to play a crucial role in fragmentation and in shaping the dynamics of accretion disks.

The difficulty can be quantified by the Reynolds number, a dimensionless parameter measuring the ratio of advective transport to viscous diffusion. It is defined as

$$Re = \frac{L_{\text{driv}} v_{\text{turb}}}{\nu}, \tag{9}$$

where  $v_{\rm turb}$  is the characteristic turbulent velocity at the largest scale (here, the cloud scale  $L_{\rm driv}$ ), and  $\nu$  is the kinematic viscosity (cf. Sect. 2.1). For Re  $\lesssim$  10, flows remain laminar. At Re  $\sim$  100, a Kármán vortex street appears, marking the transition toward turbulence, which becomes fully developed for Re  $\gtrsim$  1,000 (Frisch 1995).

In the ISM, Re typically ranges from  $\sim 10^5$  to  $10^{10}$ , confirming that it is in a state of ubiquitous, fully developed turbulence. However, even the most powerful current supercomputers only achieve simulations with effective Re  $\sim 10^5$  (see below). The challenge is the enormous dynamic range required, which demands either extremely high grid resolution or, in particle-based methods, very large numbers of particles.

As discussed in detail in Sect. 3.4.1 below, for grid-based codes, Re depends on the linear grid resolution N, as Re =  $(N/N_{\rm Re})^{p_{\rm Re}}$ , where  $N_{\rm Re}$  is the number of grid cells resolving the viscous scale (where Re = 1), and  $p_{\rm Re} = 1 + \zeta$  is determined by the scaling of the turbulent velocity dispersion with size  $\ell$ . In general,  $v_{\rm turb}(\ell) \propto \ell^{\zeta}$ , with  $\zeta = 1/3$  and  $p_{\rm Re} = 4/3$  for Kolmogorov (incompressible) turbulence (Kolmogorov 1941), and  $\zeta = 1/2$  and  $p_{\rm Re} = 3/2$  for Burgers (shock-dominated) turbulence (Burgers 1948). Intuitively, one expects  $N_{\rm Re} \sim 1$ , since eddies smaller than a grid cell cannot be resolved. Early numerical studies suggested  $N_{\rm Re} \sim 0.5$  (Benzi et al. 2008), but more recent, higher-resolution simulations indicate  $N_{\rm Re} \sim 1.5$  for subsonic and  $\sim 3$  for supersonic turbulence (Shivakumar and Federrath 2025).

The current state of the art has reached resolutions of  $\sim 10,000^3$ . For example, Ishihara et al. (2020) achieved 12,288<sup>3</sup> grid cells in incompressible hydrodynamic turbulence. Dong et al. (2022) ran subsonic MHD turbulence with  $10,000 \times 10,000 \times 5,000$  grid cells to study magnetic reconnection in the cascade, while Kempski et al. (2025) reached  $10,240^3$  for subsonic MHD turbulence. Such extreme resolutions are

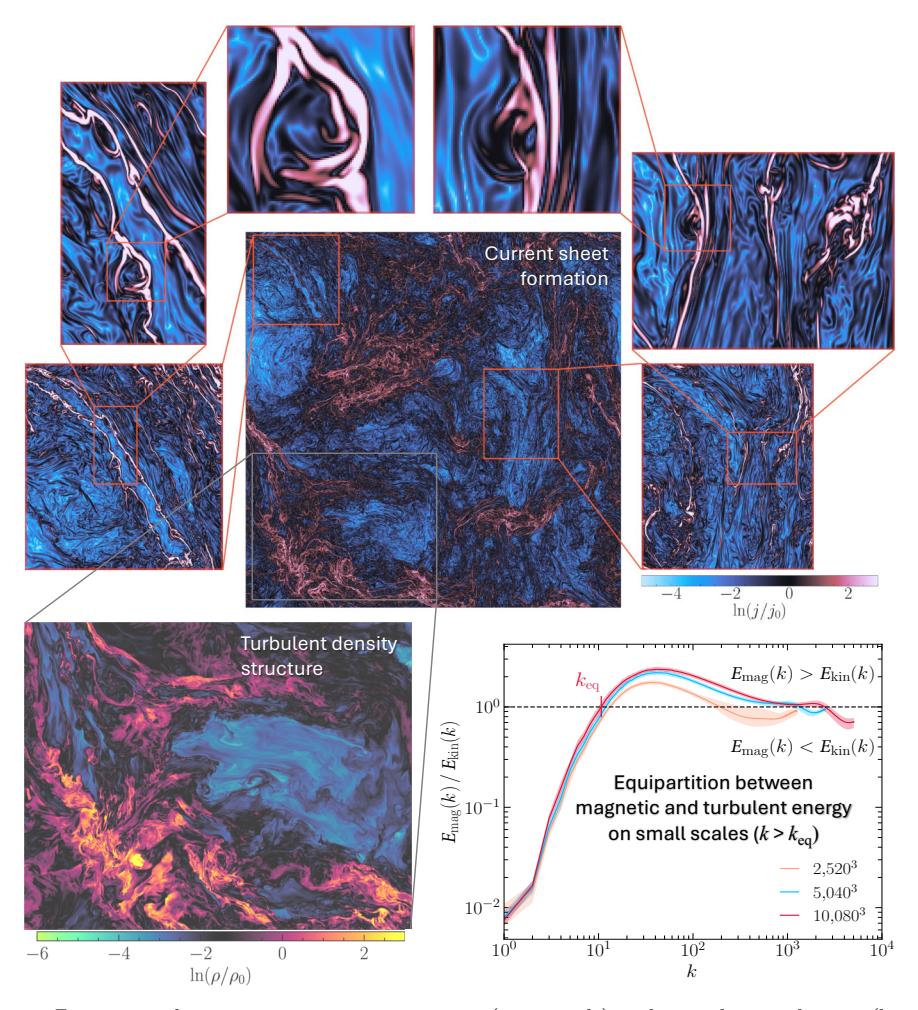


Fig. 2 Zoom into the magnetic current structures (top panels) and into the gas density (bottom left), together with the power spectrum of the magnetic-to-kinetic energy ratio  $E_{\rm mag}/E_{\rm kin}$  (bottom right) in a supersonic MHD turbulence simulation with  $10,080^3$  grid cells from Beattie et al. (2025a). Supersonic turbulence produces density contrasts spanning several orders of magnitude and intricate current structures across scales, ultimately forming strongly magnetized plasma structures on small scales. Accurately modeling these requires powerful numerical schemes and extreme resolution. A key finding is that while the magnetic field has only a modest impact on large scales (low k), magnetic energy always approaches equipartition with kinetic energy on small scales ( $k > k_{\rm eq}$ ). Numerical convergence of the energy content below  $k_{\rm eq}$  requires resolutions  $\gtrsim 5,000^3$ . Adapted from Figs. 1 and 2, and Suppl. Fig. 3 in Beattie et al. (2025a).

required to capture the geometry of magnetic current sheets at the smallest scales. In the supersonic regime relevant for molecular clouds and star formation, Federrath et al. (2021) and Beattie et al. (2025a) performed turbulence simulations with  $\gtrsim 10,000^3$  grid cells to resolve the transition from supersonic to subsonic turbulence. This 'sonic scale' may be a critical ingredient for star formation (Vázquez-Semadeni et al. 2003; Krumholz and McKee 2005; Federrath and Klessen 2012) and filament formation

(Arzoumanian et al. 2013; Federrath 2016; Federrath et al. 2016; Arzoumanian et al. 2018). A visualization of the Beattie et al. (2025a) simulation is shown in Fig. 2. A critical outcome of this is that the magnetic field always tends to be at least as strong as the kinetic field on sufficiently small scales, likely associated with the transition from supersonic to subsonic turbulence.

## 3.2 Turbulence initialization and driving

Since there is no closed-form description of turbulence, simulations must begin with an initialization phase to establish a fully-developed turbulent state with the correct statistical properties of density, velocity, and magnetic fields, and their correlations. This is achieved through 'turbulence driving', in which energy and momentum are injected until the statistical properties converge to a quasi-equilibrium state.

Turbulence is typically driven by applying an external acceleration field  $\mathbf{F}$  to the MHD system, as source terms  $\rho \mathbf{F}$  and  $\rho \mathbf{F} \cdot \mathbf{v}$  on the RHS of Eqs. (2) and (3). The field  $\mathbf{F}$  is usually generated via a stochastic Ornstein-Uhlenbeck (OU) process (Eswaran and Pope 1988; Schmidt et al. 2009; Federrath et al. 2010b; Price and Federrath 2010), which evolves smoothly in space and time. Its auto-correlation time is set to the turbulent (eddy) turnover time,  $t_{\text{turb}} = L_{\text{driv}}/(\mathcal{M}c_{\text{s}})$ , on the largest (integral) scales, where  $L_{\text{driv}} = L/2$  is the driving scale, L the domain size, and L0 the sonic Mach number defined by  $L_{\text{turb}} = L_{\text{cs}}$ .

The driving is usually constructed in Fourier space, injecting kinetic energy at the lowest wave numbers,  $1 < |\mathbf{k}| L/2\pi < 3$ , with the peak at k=2 (the L/2 scale). While different driving spectra can be used, a good choice is a driving amplitude that declines parabolically toward k=1 and k=3, confining direct driving to a narrow band of scales and allowing turbulence to develop naturally on  $k \geq 3$ . Some works have explored alternative injection scales, with spectra peaking at k=3-4 or 7-8 (Klessen 2001; Walch et al. 2012; Koch et al. 2019), or even across an entire power-law spectrum (Nam et al. 2021), to study the role of the driving scale in turbulence statistics, the emergence of inverse cascades (Brandenburg et al. 2023), and implications for star formation and the IMF (Klessen 2001; Bate 2009a; Girichidis et al. 2011; Nam et al. 2021).

By applying a Fourier-space projection,  ${\bf F}$  can be decomposed into solenoidal ( $\nabla \cdot {\bf F} = 0$ ) and compressive ( $\nabla \times {\bf F} = 0$ ) parts via Helmholtz decomposition. In index notation, the projection operator is

$$\mathbb{P}_{ij}^{\zeta}(\mathbf{k}) = \zeta \,\delta_{ij} + (1 - 2\zeta) \,k_i k_j / |\mathbf{k}|^2. \tag{10}$$

This yields a ratio of compressive-to-total driving power of

$$\frac{F_{\text{comp}}}{F_{\text{tot}}} = \frac{(1-\zeta)^2}{1-2\zeta+3\zeta^2}.$$
 (11)

Thus,  $\zeta = 1$  produces purely solenoidal driving, while  $\zeta = 0$  yields purely compressive driving. Intermediate  $\zeta$  values give mixtures, with  $\zeta = 1/2$  producing  $F_{\text{comp}}/F_{\text{tot}} = 1/3$  ('natural mixture'), equivalent to randomly selecting modes in three dimensions,

where on average one axis is compressive and two are solenoidal (Federrath et al. 2008). This turbulence-driving module is publicly available as a maintained C<sup>++</sup> code with MHD plugins and Python interfaces on GitHub (Federrath et al. 2022, https://github.com/chfeder/turbulence\_generator).

The effects of the driving mode on structure formation have been widely studied (e.g., Koch et al. 2017; Mohapatra et al. 2022). In particular, Federrath and Klessen (2012) and Mathew et al. (2023) show that compressive driving yields  $\sim 10 \times$  higher SFR and reduces the IMF characteristic mass by a factor of  $\sim 2$  compared to solenoidal driving.

## 3.3 Physical shear and bulk viscosity

The traceless rate-of-strain tensor  $\mathbb{S}_{ij} = (1/2)(\partial_i v_j + \partial_j v_i) - (1/3)\delta_{ij}(\nabla \cdot \mathbf{v})$  (Eq. 6), used in the MHD momentum and energy equations (Eqs. 2 and 3), accounts only for shear viscosity. More generally, however, viscous stresses are proportional to all components of the velocity gradient tensor  $\nabla \mathbf{v}$ , and compressible gases therefore exhibit both shear and bulk (volume) viscosity. Accordingly, the generalized Navier-Stokes equation includes not only the shear viscosity  $\nu_{\text{shear}}$ , but also the bulk viscosity coefficient  $\nu_{\text{bulk}}$ , which becomes relevant for compressible flows where  $\nabla \cdot \mathbf{v} \neq 0$  (Beattie et al. 2025b). Therefore, writing Eq. (2) (for simplicity omitting magnetic terms), including  $\nu_{\text{shear}}$  and  $\nu_{\text{bulk}}$  yields

$$\frac{\partial(\rho \mathbf{v})}{\partial t} = -\nabla \cdot (\rho \mathbf{v} \mathbf{v}) - \nabla p_{\text{th}} 
+ \nabla \cdot (2\rho \nu_{\text{shear}} \mathbb{S}) + \nabla \cdot [\rho \nu_{\text{bulk}} (\nabla \cdot \mathbf{v}) \mathbb{I}].$$
(12)

For monatomic ideal gases, the bulk viscosity is identically zero, as shown by kinetic theory (Mihalas and Mihalas 1984). In contrast, for polyatomic molecules,  $\nu_{\rm bulk}$  can be non-zero, but only if relaxation processes occur on timescales comparable to or longer than typical fluid timescales (Mihalas and Mihalas 1984). The magnitude of  $\nu_{\rm bulk}$  therefore depends strongly on the composition of the polyatomic gas, and direct measurements remain uncertain (Tisza 1942). Because turbulence studies have traditionally focused on incompressible gases, bulk viscosity is often omitted from the governing equations. However, in compressible gases and plasmas—particularly relevant for the ISM and star formation—bulk viscosity may play a significant role and thus warrants further investigation.

A recent parameter study provides new insights into the role of bulk viscosity. While the relative importance of shear and bulk viscosity depends on gas composition and remains uncertain due to laboratory measurement challenges, Beattie et al. (2025b) estimate ratios as high as  $\nu_{\rm bulk}/\nu_{\rm shear} \sim 1\text{--}100$  for the molecular phase of the ISM, where stars form. This implies measurably enhanced kinetic energy dissipation on small scales, with the strongest impact on the compressible component of the velocity field. However, Beattie et al. (2025b) also find that bulk viscosity has relatively little influence on magnetic field amplification by the turbulent dynamo. This is because the dynamo is primarily powered by vorticity, even in highly compressible

plasmas (Federrath et al. 2011b, 2014b; Achikanath Chirakkara et al. 2021), and the vortical component of the velocity field is not directly affected by bulk viscosity.

#### 3.4 Sub-resolution models for turbulence

Given the challenges of resolving turbulent flows (see Sect. 3.1), it is essential to recognize the limitations imposed by finite resolution and to develop methods for quantifying numerical dissipation. These methods can then be used to model turbulence on unresolved scales and to estimate key physical parameters on the grid scale in cosmological or galaxy-scale simulations. Such parameters include the turbulent Mach number, the virial parameter, the effective driving mode of turbulence, and the plasma beta (in the presence of magnetic fields). These sub-resolution properties provide crucial inputs for turbulence-based star formation models, for example by regulating the amount of local stellar feedback to be injected in large-scale simulations. In this way, sub-resolution turbulence models serve as a critical bridge between smallscale physics, which cannot be directly resolved, and the global dynamics of galaxies and star-forming regions, thereby enabling simulations to incorporate the essential impact of turbulence across vastly different scales.

## 3.4.1 Numerical viscosity and resistivity

The first step in sub-resolution modeling is to quantify and predict the levels of numerical viscosity and resistivity — specifically, the effective kinetic and magnetic Reynolds numbers that can be achieved for a given grid or particle resolution. To address this, Kriel et al. (2022, 2025) conducted an extensive suite of turbulence simulations in both the subsonic and supersonic regimes, explicitly including physical viscosity and resistivity terms. By systematically varying  $\nu$  and  $\eta$  while changing the grid resolution, they demonstrated that converged results are obtained only above a threshold resolution  $N_{\text{thresh}}$  (where N is the number of grid cells per dimension). If  $N < N_{\text{thresh}}$ for a target Re and/or Rm, then numerical viscosity and/or resistivity dominate over the explicit terms, such that the effective Re and Rm fall below the intended values.

Using the relations in Kriel et al. (2022, 2025) as a foundation, Shivakumar and Federrath (2025) conducted a large parameter study with varying N and purely numerical dissipation, deriving relations between the resolution N and the achievable Re and Rm,

$$Re = (N/N_{Re})^{p_{Re}}, \qquad (13)$$

$$Re = (N/N_{Re})^{p_{Re}},$$
 (13)  
 $Rm = (N/N_{Rm})^{p_{Rm}},$  (14)

where the driving scale of turbulence is taken as L/2, with L the domain side length covered by N resolution elements in each direction. The parameters  $N_{\rm Re}$ ,  $p_{\rm Re}$ ,  $N_{\rm Rm}$ , and  $p_{\rm Rm}$  were determined from high-resolution implicit large-eddy simulations (ILES) spanning  $N^3 = 144^3$  to 2,576<sup>3</sup>, using spectral fitting. Figure 3 summarizes the achievable Re and Rm as functions of N based on these relations. Solid lines show the fits from Shivakumar and Federrath (2025), with shaded regions spanning one order of magnitude to represent maximum uncertainty. Two sets of relations are displayed:

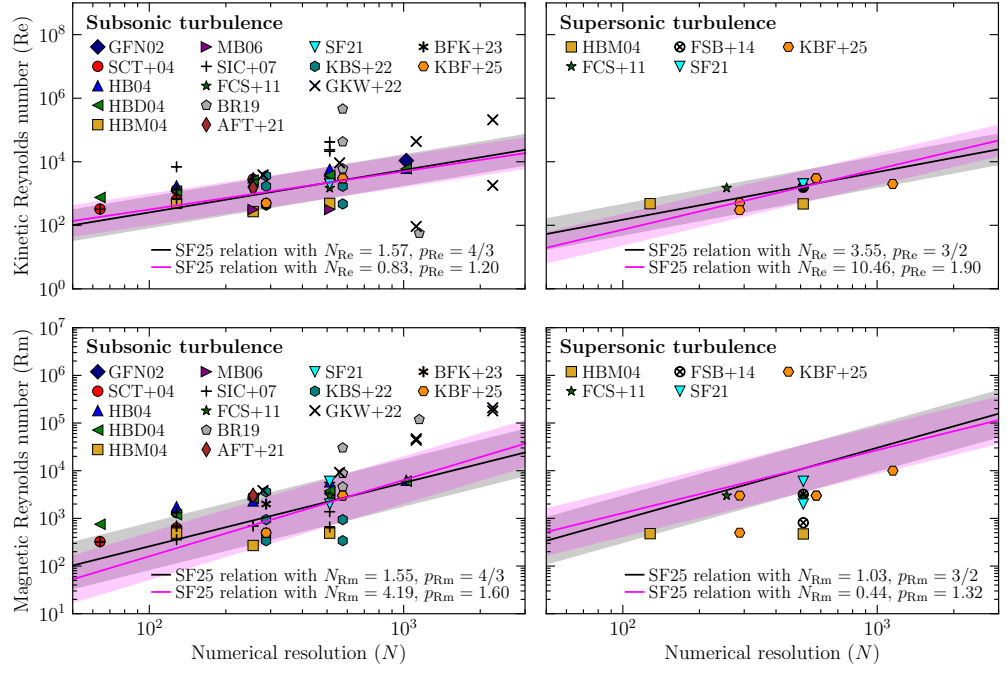


Fig. 3 Kinetic Reynolds number (Re, top) and magnetic Reynolds number (Rm, bottom) as functions of the number of resolution elements (N) along one side of a cubic domain, shown for the subsonic (left) and supersonic (right) turbulence regimes. Data points represent simulations with explicit dissipation, i.e., Re and Rm values set by the authors of the respective works (see legend): GFN02 (Gotoh et al. 2002), SCT+04 (Schekochihin et al. 2004), HB04 (Haugen and Brandenburg 2004), HBD04 (Haugen et al. 2004a), HBM04 (Haugen et al. 2004b), MB06 (Mee and Brandenburg 2006), SIC+07 (Schekochihin et al. 2007), FCS+11 (Federrath et al. 2011b), BR19 (Brandenburg and Rempel 2019), AFT+21 (Achikanath Chirakkara et al. 2021), SF21 (Seta and Federrath 2021), KBS+22 (Kriel et al. 2022), GKW+22 (Galishnikova et al. 2022), BFK+23 (Beattie et al. 2023), and KBF+25 (Kriel et al. 2025) for the subsonic regime, and HBM04, FCS+11, FSB+14 (Federrath et al. 2014a), SF21, and KBF+25 for the supersonic regime. The lines show Re-N and Rm-N relations derived by Shivakumar and Federrath (2025), with parameters listed in each panel. These relations provide estimates of the maximum Re and Rm achievable for a given N due solely to numerical dissipation. Shaded regions indicate the associated uncertainties, accounting for methodological variations as well as differences across 14 numerical schemes, including different grid-based methods and SPH.

black lines fix  $p_{\rm Re} = p_{\rm Rm} = 4/3$  for subsonic turbulence and  $p_{\rm Re} = p_{\rm Rm} = 3/2$  for supersonic turbulence, consistent with theoretical scaling expectations (Federrath et al. 2021; Shivakumar and Federrath 2025). Magenta lines, in contrast, allow  $p_{\rm Re}$  and  $p_{\rm Rm}$  to vary freely. Parameter values are reported in the figure legends. The shaded bands capture uncertainties from fitting, methodological variations, and code-to-code differences across a wide range of numerical schemes, including grid-based solvers (with/without Riemann solvers, flux limiters, etc.) and SPH (Price et al. 2018).

The data points in Figure 3 represent simulations from the literature reporting target Re and Rm values obtained with explicit viscosity and resistivity in the MHD equations (Eqs. 1-5). However, even with explicit dissipation included, numerical dissipation remains present and may dominate depending on N. Simulations lying

significantly above the SF25 relations are dominated by numerical dissipation, while those within or below the relations are converged with respect to their chosen Re and/or Rm.

In practice, this means that simulations cannot reach high Reynolds numbers simply by lowering the explicit viscosity or resistivity; sufficient resolution is also essential. For example, the SF25 relations show that at grid resolutions routinely achievable today ( $N^3 \sim 1,024^3$ ), the effective Re  $\sim 10^3 - 10^4$  for both subsonic and supersonic turbulence. While this is nominally turbulent, i.e., Re  $\gtrsim 1000$  (Frisch 1995), it remains far below the ISM values of Re  $\sim 10^9$ , which would require  $N \sim 10^6 - 10^7$  depending on turbulence regime and the uncertainties in the SF25 relations. The largest current simulations ( $N \sim 10,000$ ) reach Re  $\sim 10^5 - 10^6$  (Ishihara et al. 2020; Federrath et al. 2021; Beattie et al. 2025a; Kempski et al. 2025). Further progress will depend on improved algorithms, continued code optimization, and advances in supercomputing technology (cf. Sect. 1.2).

## 3.4.2 Local kinetic energy dissipation rate

To quantify the local viscosity (numerical and, if present, explicit), we need to determine what the kinetic energy of the system would have been in the absence of dissipation. Although this may appear elusive, it can be obtained by deriving an evolution equation for the kinetic energy itself<sup>4</sup>, analogous to the total energy equation. Applying  $\mathbf{v} \cdot (\dots)$  to Eq. (2) yields (see Troccoli and Federrath 2025),

$$\frac{\partial E_{\text{kin}}}{\partial t} = -\nabla \cdot \left[ (E_{\text{kin}} + p) \mathbf{v} - \frac{1}{4\pi} (\mathbf{B} \cdot \mathbf{v}) \mathbf{B} \right] + p_{\text{th}} (\nabla \cdot \mathbf{v}), \tag{15}$$

where  $E_{\rm kin} = \rho |\mathbf{v}|^2/2$  is the kinetic energy density, and  $p = p_{\rm th} + |\mathbf{B}|^2/(8\pi)$  the total (thermal + magnetic) pressure. Note that the last term only involves  $p_{\rm th}$ . Unlike Eq. (3), explicit viscosity terms are omitted here, since the aim is to track numerical dissipation and obtain a local, time-dependent measure of it.

Evolving Eq. (15) alongside Eqs. (1)–(5) offers a direct measure of local dissipation. Denoting post-timestep quantities with a prime, the dissipation-free kinetic energy from Eq. (15) is  $E'_{\rm kin}$ . In contrast, the kinetic energy from the standard MHD update is  $\rho'|{\bf v}'|^2/2$ , which is dissipative<sup>5</sup>. The key point is that Eq. (2) updates the velocity in a momentum-conserving, rather than energy-conserving, manner. The local kinetic energy dissipation rate is therefore

$$\varepsilon_{\rm kin} = \frac{E'_{\rm kin} - \rho' |\mathbf{v}'|^2 / 2}{\Delta t},\tag{16}$$

providing a direct measure of the kinetic energy lost through numerical discretization and solver-specific diffusion (e.g., artificial viscosity or slope limiting).

 $<sup>^4\</sup>mathrm{By}$  'perfectly evolved kinetic energy' we mean dissipation-free within the order of accuracy and limitations of the numerical scheme.

<sup>&</sup>lt;sup>5</sup>In practice, MHD codes compute the new thermal energy by subtracting  $\rho'|\mathbf{v}'|^2/2$  from the updated total energy, effectively adding dissipated kinetic energy to the thermal reservoir.

This framework also enables estimates of the sub-resolution turbulent velocity,

$$v_{\text{turb,unresolved}} = \left(2E'_{\text{kin}}/\rho' - |\mathbf{v}'|^2\right)^{1/2},\tag{17}$$

from which one can compute the sub-resolution turbulent Mach number or virial parameter. These are central inputs to turbulence-regulated star formation models that determine the star formation rate (Krumholz and McKee 2005; Padoan and Nordlund 2011; Hennebelle and Chabrier 2011; Federrath and Klessen 2012; Burkhart and Mocz 2019; Hennebelle et al. 2024) and the stellar initial mass function (Padoan and Nordlund 2002; Hennebelle and Chabrier 2008, 2009, 2013; Hopkins 2013b; Guszejnov et al. 2022; Mathew et al. 2025). Coupling such dissipation diagnostics with turbulence-based star formation prescriptions offers a promising pathway for sub-resolution star formation models in galaxy and cosmological simulations, where cloud scales are marginally resolved (e.g., Semenov et al. 2016; Kang et al. 2025). A similar approach has recently been implemented in Semenov (2024).

## 3.5 Numerical advances and challenges

## 3.5.1 Positivity-preserving schemes

A major advance in the development of robust numerical schemes for MHD has been the introduction of positivity-preserving solvers. Building on the theory of nonlinear stability for finite-volume methods, Bouchut et al. (2007) formulated a relaxation-based approximate Riemann solver that guarantees non-negative density and pressure while remaining consistent with entropy stability. The relaxation framework replaces the MHD fluxes with a multi-wave system that is easier to control numerically, yet faithfully represents the full wave structure of MHD. Practical three- and five-wave implementations (Waagan et al. 2011) demonstrated that this approach provides a computationally efficient alternative to standard approximate solvers, with the added benefit of strict positivity preservation—an essential feature for simulations involving strong shocks, rarefactions, and vacuum-like states, such as those encountered in supersonic turbulence and star-formation applications. More recent adaptations and extensions of this include works by Derigs et al. (2016) and Birke et al. (2021), with the latter allowing accurate solutions with significantly reduced dissipation in flows with low Mach numbers (see also Leidi et al. 2022; Watt et al. 2025).

For example, in simulations of supersonic turbulence with  $\mathcal{M} \sim 10$  (Lee et al. 2009), even robust solvers such as HLLD (Harten–Lax–van Leer Discontinuities) (Miyoshi and Kusano 2005) require careful tuning and the use of relatively low CFL factors (Courant et al. 1928) to maintain stability. By contrast, turbulence simulations exceeding  $\mathcal{M} \sim 20$  can be evolved stably at high resolution with the positivity-preserving HLLxR scheme (Harten–Lax–van Leer Relaxation, where the 'x' denotes the 3-wave or 5-wave implementation; see Waagan et al. 2011), even though increasing resolution steepens gradients and amplifies density contrasts in isothermal shocks, making stability more challenging (Federrath 2013). A similar advantage has been demonstrated in simulations of jet launching and propagation (e.g., Seifried et al. 2012), where the HLLxR scheme has proven highly effective.

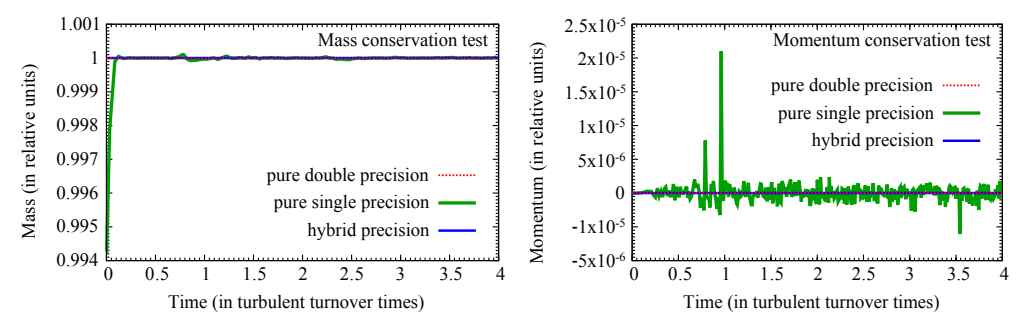


Fig. 4 Comparison of double-precision, single-precision, and hybrid-precision schemes for supersonic MHD turbulence. The hybrid scheme (blue line) matches the accuracy of double precision (red dotted line), conserving gas mass (left) and momentum (right), while single precision (green line) exhibits significant errors. At the same time, the hybrid scheme provides a computing speed-up and reduces memory use by a factor of  $\sim 2$  relative to double precision.

## 3.5.2 Hybrid precision

A promising way to accelerate future simulations while simultaneously increasing numerical resolution is to employ a 'hybrid-precision' approach. In such schemes, all hydrodynamical variables are stored in single precision (4 bytes per floating-point number), while critical operations are performed in double precision (8 bytes per floating-point number). This design retains the accuracy of full double-precision calculations while reducing memory usage and compute time. Operations that require double precision—such as summations over large numbers of resolution elements (e.g., for volume or mass averages)—are explicitly forced to run in double precision.

For example, Federrath et al. (2021) implemented a hybrid-precision algorithm for MHD turbulence simulations, achieving performance gains of  $\sim 3\text{--}4\times$  over the standard (public) version of the FLASH code (Fig. 1). Independent of other optimizations, switching to hybrid precision alone typically yields a  $\lesssim 2\times$  speed-up, provided communication is bandwidth-limited rather than latency-limited — a condition that can be met by packing MPI messages and thereby reducing communication frequency. Additional optimizations, such as removing unused 3D fields and inlining the EOS into the MHD solver, further improved runtime and memory usage, leading to the overall factor of 3–4 reported in Federrath et al. (2021). Figure 4 compares pure double-precision and single-precision runs with the hybrid scheme for a standard turbulence setup. Gas mass (left panel) and momentum (right panel) remain well conserved in the hybrid scheme, while significant errors appear in pure single-precision mode.

Hybrid-precision methods reproduce high-order statistical moments and power spectra of turbulence without significant loss of accuracy. They therefore hold strong promise for enabling very high-resolution simulations while reducing computational cost and carbon footprint. The method was recently extended to a particle-in-cell (PIC) code (Chirakkara et al. 2024), demonstrating its potential beyond grid-based hydrodynamics. Future extensions to other physics modules, such as gravity and radiation, may provide further benefits. Hybrid-precision schemes are becoming

increasingly relevant in HPC, particularly with the rise of GPU computing, where limited working memory and performance constraints often necessitate single-precision operations<sup>6</sup>.

#### 3.5.3 GPU acceleration

GPU acceleration has become central to HPC, and more codes are adapting to GPUs for MHD and other physics capabilities. However, using GPUs well hinges on performance portability across rapidly changing vendor ecosystems. Two community portability layers are often used: Kokkos<sup>7</sup> (templated C<sup>++</sup> abstractions targeting CUDA/HIP/SYCL/HPX/OpenMP) and AMReX<sup>8</sup> (GPU-aware, block-structured AMR framework). Both address common hotspots: finite-volume loops, Riemann solves, reconstruction, and divergence control, while exposing GPU-friendly iteration and memory models. Persistent challenges include bandwidth-bound kernels, AMR data motion and kernel launch overheads, multi-GPU scaling with overlap of communication/compute, and maintaining numerical reproducibility and stability when using mixed precision (cf. Fig. 4) or fast-math options.

The ATHENAK, FLASH-X, and QUOKKA astrophysics codes are a few example codes supporting GPUs. ATHENAK<sup>9</sup> (Stone et al. 2024) is a performance-portable implementation of the ATHENA<sup>++</sup> AMR framework that uses Kokkos to run MHD on CPUs and GPUs, providing a single code base for heterogeneous systems and multi-GPU capability via Kokkos backends. Under significant development, FLASH-X<sup>10</sup> (Dubey et al. 2022; Dhruv et al. 2023) aims to adopt a code-generation—driven performance-portability strategy and options for Fortran—Kokkos as well as Fortran—AMReX interoperability layers to offload selected kernels to GPUs while preserving the long-standing multiphysics architecture provided in FLASH. QUOKKA<sup>11</sup> (Wibking and Krumholz 2022) targets GPU-resident MHD as well as radiation hydrodynamics with AMR using AMReX, with strong single-GPU throughput and a unified CPU/GPU code base.

## 3.6 Summary of challenges and future directions

Turbulence remains one of the fundamental unsolved problems in physics and mathematics. Numerical methods are indispensable for advancing our understanding, but modeling truly turbulent flows, such as those in the ISM, requires Reynolds numbers of order  $\sim 10^9$ —well beyond the reach of current supercomputers. This gap between physical reality and numerical feasibility remains a central challenge for the field.

Despite these limitations, major progress has been made in recent years. Advances in code optimization, such as the hybrid-precision method (Sect. 3.5.2), now allow simulations at resolutions up to  $10,000^3$  grid cells, corresponding to effective Reynolds numbers of order  $10^5$ , based on improved understanding of how numerical viscosity

 $<sup>^6</sup>_{-} {\rm Even}$  FP64 GPUs typically run at  $2\times$  speed in single precision compared to double precision.

<sup>&</sup>lt;sup>7</sup>https://github.com/kokkos

<sup>8</sup> https://amrex-codes.github.io/amrex

<sup>&</sup>lt;sup>9</sup>https://github.com/IAS-Astrophysics/athenak

<sup>&</sup>lt;sup>10</sup>https://github.com/Flash-X

<sup>&</sup>lt;sup>11</sup>https://github.com/quokka-astro

scales with grid resolution (Sect. 3.4.1). At the same time, many codes are being modernized for GPU acceleration, opening additional opportunities to push toward higher effective Reynolds numbers in the near future. Another critical advance has been the development of positivity-preserving MHD schemes (Sect. 3.5.1), which remain robust in the presence of strong shocks and discontinuities. These solvers are particularly important for modeling the highly compressible, supersonic turbulence that dominates the star-forming ISM, enabling both fundamental turbulence studies and more reliable simulations of star formation.

Further progress has also been made in capturing local dissipation rates. This includes both numerical and physical dissipation, with extensions beyond the standard shear viscosity to include bulk viscosity effects (Sect. 3.3). New methods evolve the kinetic energy equation directly (Sect. 3.4.2) alongside the standard MHD equations (Sect. 2.1), providing novel ways of estimating sub-resolution turbulent velocity dispersions and energies. These quantities are crucial for subgrid star-formation models and can be applied in galaxy-scale simulations. A promising direction for future work is to extend these approaches to quantify the local magnetic energy dissipation rate, providing a more complete view of turbulent energy transfer and its impact on star formation and ISM dynamics.

## 4 Gravity

Modeling gravity is a fundamental requirement in star-formation simulations. Once the the gravitational acceleration  $\mathbf{g}(\mathbf{x},t)$  is computed, it is incorporated into the MHD system (Eqs. 1–5) by adding the terms  $+\rho\mathbf{g}$  and  $+\rho\mathbf{v}\cdot\mathbf{g}$  to the RHS of Eqs. (2) and (3), respectively, as source terms, where  $\mathbf{g} = -\nabla\Phi$  can be written as the negative gradient of the gravitational potential  $\Phi$ .

#### 4.1 Discrete mass distributions

To obtain  $\mathbf{g}$ , ideally, the gravitational acceleration  $\mathbf{g}_i$  of a fluid element and/or mass particle i at position  $\mathbf{x}_i$  can be determined directly via a sum over the contributions from all N mass elements  $m_i$  at positions  $\mathbf{x}_j$ , as

$$\mathbf{g}_i = -G\sum_{j=1}^N m_j \frac{\mathbf{r}_j}{r_j^3} \mathcal{K}(r_j/r_{\text{soft}}), \tag{18}$$

where G is the gravitational constant,  $\mathbf{r}_j = \mathbf{x}_i - \mathbf{x}_j$  and  $r_j = |\mathbf{r}_j|$ . The function  $\mathcal{K}(r_j/r_{\text{soft}})$  is a cubic-spline softening kernel (Monaghan and Lattanzio 1985; Price and Monaghan 2007),

$$\mathcal{K}(\tilde{r}) = \begin{cases}
4\tilde{r}^2 \left(\frac{8}{3}\tilde{r} - \frac{48}{5}\tilde{r}^3 + 8\tilde{r}^4\right) & \text{for } 0 \leq \tilde{r} < \frac{1}{2}, \\
4\tilde{r}^2 \left(\frac{16}{3}\tilde{r} - 12\tilde{r}^2 + \frac{48}{5}\tilde{r}^3 - \frac{8}{3}\tilde{r}^4 - \frac{1}{60}\tilde{r}^{-2}\right) & \text{for } \frac{1}{2} \leq \tilde{r} < 1, \\
1 & \text{for } \tilde{r} \geq 1,
\end{cases} \tag{19}$$

with the dimensionless radius  $\tilde{r} = r/r_{\rm soft}$ , where  $r_{\rm soft}$  is a user-defined gravitational softening radius. Gravitational softening is required, because otherwise  $\mathbf{g} \to \infty$  when particles approach one another. Using this kernel, we see that  $\mathcal{K} \to 0$  smoothly when  $r \to 0$ , and  $\mathcal{K} = 1$  for  $r \geq r_{\rm soft}$ , such that we recover Newton's exact acceleration with Eqs. (18) and (19) outside the softening radius, which is preferred over simpler softening approaches, such as Plummer softening, where  $\mathcal{K}(\tilde{r}) = \tilde{r}^3(\tilde{r}^2 + 1)^{-3/2}$ , which only approaches the exact solution for  $r \gg r_{\rm soft}$ .

Equation (18) is essentially how a basic N-body method approaches the problem for discrete point masses and is the most accurate way to compute the gravitational acceleration. However, direct summation is by definition very slow, so most particle-based gas dynamics codes solve for the gravitational forces by hierarchically grouping close neighbors and constructing a tree (e.g., see Sect. 4.4.3).

#### 4.2 Continuous mass distributions

For continuous mass distributions, modeling gravity essentially requires the solution of the Poisson equation for the gravitational potential,  $\Phi$ ,

$$\nabla^2 \Phi = 4\pi G \rho. \tag{20}$$

There are three main methods to obtain a numerical solution of the Poisson equation, which are discussed in more detail below (FFT, multi-grid, tree-based), where all three can be adopted in grid-based codes, while only the third one is usually adopted in particle-based codes.

## 4.3 Combining the gravitational effects of gas and stars

Finally, the most common situation for star-formation calculations is that we have both gas and stars coexisting, in which case we simply add up their contributions to the total gravitational potential and acceleration,

$$\Phi = \nabla \Phi_{\rm gas} + \nabla \Phi_{\rm sinks}, \tag{21}$$

$$\mathbf{g} = \mathbf{g}_{\text{gas}} + \mathbf{g}_{\text{sinks}}.\tag{22}$$

A common approach would be to solve Poisson's equation (Eq. 20) for the gas, and direct summation for the stars. Indeed, Eq. (18) can be used for the star-particle method described in detail below (Sect. 5.2), and is efficient as long as the number of star particles N in a simulation is not exceedingly large, which is problem-dependent. For typical star-formation simulations, which nowadays have > millions of resolution elements (grid cells or SPH particles), a direct summation method is efficient for star-particle counts of the order of a thousand, as the cost of direct summation scales as  $N^2$  in order to compute  $\mathbf{g}$  for all particles. For continuous mass distributions (i.e., the gas) we now look into three different basic methods.

## 4.4 Methods for solving the Poisson equation

#### 4.4.1 FFT methods

If the system has periodic boundary conditions and can be represented on a uniform grid, the solution to Poisson's equation can be obtained via Fourier transformation, i.e., in wavenumber (**k**) space<sup>12</sup>. In this case,  $\nabla^2 \to -|\mathbf{k}|^2$ , and after FFT of  $\rho \to \rho_k$ , Eq. (20) becomes

$$-|\mathbf{k}|^2 \Phi_k = 4\pi G \rho_k,\tag{23}$$

which is algebraically solved for  $\Phi_k = -4\pi G \rho_k/|\mathbf{k}|^2$ . Ignoring the k=0 mode (mean density), because only density fluctuations matter for the potential in a periodic system, inverse FFT of  $\Phi_k$  yields  $\Phi$ . While this method is fast (as FFT scales with  $N \log N$ ), it has the obvious limitation that it only works on a uniform grid, and only for periodic boundary conditions (although FFT-based methods that also work with free boundaries have been developed; see Genovese et al. 2006), neither of which are usually the case for star-formation simulations.

## 4.4.2 Multi-grid methods

While FFT-based solvers are extremely efficient for periodic systems on a uniform grid, their applicability is restricted when dealing with non-periodic boundary conditions, and situations where high dynamic range in resolution is required. In astrophysical simulations, gravitational potentials often need to be resolved over many orders of magnitude in density and spatial scale. Multi-grid methods (Briggs et al. 2000; Trottenberg et al. 2001) are particularly suited for this as they employ a hierarchy of grids at different resolutions. The core idea is to smooth high-frequency error components on fine grids and correct low-frequency errors on coarser grids, accelerating convergence compared with simple relaxation methods.

A key element of multi-grid is that the initial conditions for the iterative solution of Poisson's equation on the fine grids is obtained from interpolated solutions on the respective coarser grids. This hierarchical cycling between grid levels makes multigrid solvers among the fastest iterative methods available for elliptic equations such as Poisson's equation. However, it should be noted that multi-grid methods therefore require a relatively low-resolution (coarse) grid on the lowest level of the grid hierarchy, because the lowest level is where initial guesses are required to initialize the iteration. This can cause problems if one wants to employ a large (high-resolution) base grid on the lowest-resolution level, because the initial iteration may take a very long time to converge. For star-formation applications that use a large molecular cloud as a basis, where turbulence needs to be resolved on a base grid of at least  $256^3$  cells or more, this step in the multi-grid solve can become prohibitively expensive. The only solution is to add 'ghost' lower-level grids to artificially extend the multi-grid hierarchy to coarserresolution grids. Alternatively, if the system represents a  $\sim 1-10$  pc-sized molecular cloud, which is always embedded in the larger-scale ISM of the galaxy, then periodic boundary conditions can be a reasonable approximation (Klessen et al. 2000; Jappsen et al. 2005; Federrath and Klessen 2012; Krumholz et al. 2016; Mathew et al. 2023,

 $<sup>^{12}{\</sup>rm In}$  practice one would use a Fast Fourier Transform (FFT) method.

2025), in which case the coarse-level multi-grid solve can be done via the FFT method above, followed by the standard multi-grid cycles to finer grids of the AMR hierarchy.

In practice, multi-grid approaches allow localized refinement while still solving the global problem consistently, making them well suited for self-gravitating astrophysical flows, adaptive mesh refinement (AMR) frameworks, and different types of boundary conditions. A few examples of multi-grid in astrophysical AMR codes are FLASH (Ricker 2008), ENZO (Bryan et al. 2014), and RAMSES (Teyssier 2002) (see Table 1. These methods provide the flexibility and scalability necessary for modern simulations of cosmic structure formation and star-forming systems.

#### 4.4.3 Tree-based methods

Another widely used alternative to FFT or multi-grid solvers are tree methods, which are particularly well suited for N-body simulations of self-gravitating systems. Instead of mapping the mass density onto a mesh, tree algorithms operate directly on particle distributions. The essential idea is to hierarchically subdivide the computational domain into nodes (or cells), forming an octree in 3D or a quadtree in 2D. At each level of the tree, the mass distribution of a node can be approximated by a multipole expansion when viewed from sufficiently large distances. This reduces the computational cost of force evaluation from the brute-force  $\mathcal{O}(N^2)$  scaling to approximately  $\mathcal{O}(N\log N)$ , while retaining controllable accuracy. The Barnes–Hut (BH) method (Barnes and Hut 1986) is the classic example, introducing a simple opening-angle criterion to decide whether a distant group of particles can be treated as a single node or whether the tree must be further refined.

In the BH-tree algorithm, the decision to approximate a group of particles by a single pseudo-particle is governed by the opening-angle criterion,

$$\frac{l}{d} < \theta, \tag{24}$$

where l is the size of the node (typically the side length of the cubic cell enclosing the particles), d is the distance from the particle under consideration to the node's center of mass (COM), and  $\theta$  is a user-chosen tolerance parameter (commonly  $\theta \sim 0.5-0.7$ , with lower  $\theta$  resulting in higher accuracy). If this inequality is satisfied, the node subtends a sufficiently small angle and its contents are treated as a single body of mass  $m_{\text{node}}$  located at the COM of that node  $\mathbf{x}_{\text{COM}}$ . The gravitational acceleration contribution then reduces to the standard point-mass expression, i.e., using Eq. (18) with  $m_j = m_{\text{node}}$  and  $\mathbf{r}_j = \mathbf{x}_i - \mathbf{x}_{\text{COM}}$  for each node. If the criterion is not met, the node is 'opened' and the test applied recursively to its children. This adaptive procedure ensures that distant groups of particles are efficiently approximated, while nearby or extended structures are resolved in detail, balancing speed and accuracy.

Tree-based methods have proven especially powerful in astrophysical contexts where mass distributions are highly clustered and the dynamic range is large. Unlike mesh-based solvers, they naturally adapt to particle positions without requiring a predefined grid, making them efficient for collisionless dynamics, galaxy formation, cosmological structure growth, and star-formation simulations. Hybrid approaches

are also common, for instance the TreePM method (Xu 1995; Bode et al. 2000; Bagla 2002), which combines a particle—mesh solver for long-range forces with a tree algorithm for short-range interactions, achieving both speed and flexibility. For comprehensive introductions, the original Barnes and Hut (1986) paper remains the canonical reference, complemented by later reviews such as Springel (2005) for the GADGET code family.

While tree-based methods have traditionally been applied in particle-based simulations, they can also be adapted for grid-based approaches by treating individual cells as effective point masses. An example is the BH-tree solver implemented in FLASH (Wünsch et al. 2018). Moreover, the utility of tree algorithms extends well beyond solving the Poisson equation. Since the method hierarchically subdivides the domain into nodes characterized by angular size and distance relative to each evaluation point, it can be repurposed for ray-tracing applications. Prominent examples are TreeCol (Clark et al. 2012) and TreeRay (Wünsch et al. 2021; Klepitko et al. 2023; Gaches et al. 2023), which use the tree structure to estimate local column densities and shielding from external radiation fields. In these applications, the angular domain is typically discretized using the Hierarchical Equal Area isoLatitude Pixelization of the sphere (HEALPix; see Górski et al. 2005), which provides an efficient equal-area tessellation of the sphere and ensures uniform angular coverage.

## 4.5 Summary of challenges and future directions

Gravitational interactions in simulations can broadly be divided into two categories: (i) interactions between point masses (e.g., stars) and (ii) interactions of continuous mass distributions (e.g., gas). For point-mass systems, direct N-body summation with gravitational softening (Sect. 4.1) or tree-based methods (Sect. 4.4.3) are commonly employed. Continuous mass distributions, by contrast, require solving Poisson's equation. In particle-based approaches such as SPH or mesh-free methods, tree solvers are often used to approximate the continuous density field. In grid-based methods, the choice of solver depends on geometry and boundary conditions: FFT solvers (Sect. 4.4.1) are the most efficient for periodic domains and uniform grids, while multi-grid methods (Sect. 4.4.2) are best suited for hierarchically refined meshes with complex boundaries. Tree-based solvers can also be applied in grid codes, where they demonstrate both accuracy and efficiency. A further advantage of tree methods is their versatility, as they can be extended to compute column densities via ray-based techniques that exploit the tree structure.

Overall, gravitational solvers in modern star formation simulations have become highly robust, yielding accurate solutions when convergence criteria are satisfied (e.g., the opening-angle parameter in tree codes or tolerance thresholds in iterative multigrid solvers). However, a notable challenge arises in how interactions between gas and stars are treated. Many codes compute these interactions via the Poisson solver, which introduces significant effective smoothing of the stellar potential. This can degrade the accuracy of stellar orbits embedded in dense gas distributions—an crucial regime in star formation. To avoid such artifacts, direct N-body summation should be considered for gas—star interactions, even though it comes at higher computational cost.

This remains an important area for future development, balancing numerical accuracy with computational efficiency.

## 5 Star formation

As gravitational collapse proceeds, regions of runaway density enhancement form. Following collapse to the natural endpoint of star formation calculations—stellar densities of  $\sim 1\,\mathrm{g\,cm^{-3}}$ —requires a dynamic range of some 20 orders of magnitude in density. Meanwhile, numerical stability requires significantly reduced time-steps to treat the evolution of the accompanying small spatial scales as sufficient resolution (see Sect. 5.1). While calculations of the collapse of isolated dense cores have succeeded in modeling protostar formation self-consistently (e.g., Tomida et al. 2013), these are limited to relatively short evolutionary times of  $\mathcal{O}(1)$  yr, though recent advances are pushing to later stages of disk formation and evolution (Xu and Kunz 2021a,b; Mauxion et al. 2024, e.g.,). The cost remains prohibitive for calculations of star cluster formation, which commence from parsec scales and aim to follow dynamical times of millions of years.

Consequently, most star formation calculations adopt significantly lower spatial resolution and instead follow processes in smaller, denser regions using a 'sub-resolution model' attached to a particle that represents an individual star or stellar group termed a 'sink particle' (Bate et al. 1995). Sink particles accrete material from the gaseous domain (i.e., from the grid or from SPH particles), i.e., they are mass sinks, but have no internal structure, and thus require no further spatial or temporal resolution. Sophisticated treatments may attach detailed evolutionary models to the particles that follow time-dependent protostellar evolution and stellar feedback. Below we describe different numerical treatments for sink particles (Sect. 5.2), sub-resolution modeling of stellar evolution (Sect. 6.1), and various forms of stellar feedback (Sect. 6.2–6.6).

## 5.1 Jeans resolution criterion

Since stars form in dense, self-gravitating gas, the standard resolution criterion in simulations of star formation is based on resolving the Jeans length,

$$\lambda_{\rm J} = \left(\frac{\pi c_{\rm s}^2}{G\rho}\right)^{1/2},\tag{25}$$

where  $c_s$  is the sound speed and G is the gravitational constant. Truelove et al. (1997) demonstrated that  $\lambda_J$  must be resolved by at least 4 grid cells to avoid artificial fragmentation. Subsequent studies have shown that much higher Jeans resolution ( $\sim 30$  cells) is needed to capture additional physical processes on the Jeans scale, including convergence of the turbulent solenoidal energy, capturing minimal dynamo amplification of magnetic fields, and resolving small-scale density substructure (Turk et al. 2009; Sur et al. 2010; Federrath et al. 2011b; Turk et al. 2012; Federrath et al. 2014b). An equivalent resolution criterion can be formulated for particle-based methods such as

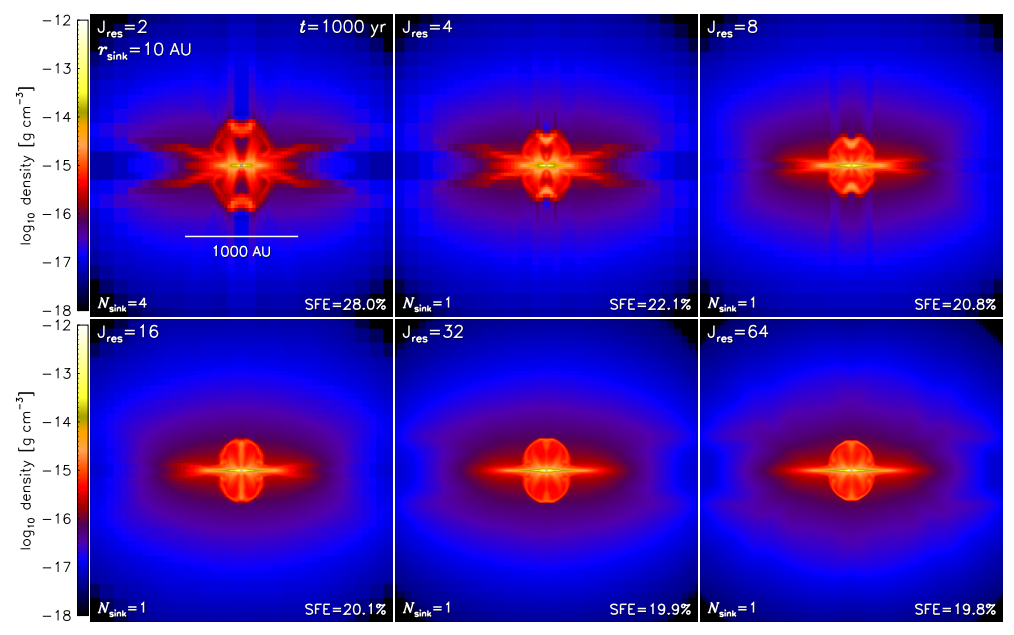


Fig. 5 Jeans resolution study of accretion disk and outflow formation, 1000 yr after the formation of the protostar, with edge-on slices through the disk. Panels show identical simulations but with Jeans resolutions of  $J_{\rm res}=2,\,4,\,8,\,16,\,32,\,{\rm and}\,64$  cells per  $\lambda_{\rm J}$ . For  $J_{\rm res}=2,\,{\rm artificial}$  fragmentation produces four sink particles (annotated as  $N_{\rm sink}$ ), while only a single star forms for  $J_{\rm res}\geq 4$ , confirming the Truelove et al. (1997) criterion. However, disk and outflow structure, as well as the accretion rate (measured by the fraction of gas accreted, i.e., the star formation efficiency after 1000 yr), only converge for  $J_{\rm res}\gtrsim 30$ . Figure adapted from Federrath et al. (2014b).

SPH, moving-mesh, and meshless approaches (see Table 1), by requiring adequate resolution of the Jeans mass,  $M_{\rm J}=(4\pi/3)(\lambda_{\rm J}/2)^3\rho$ , as introduced by Bate and Burkert (1997).

Most grid-based star formation studies now adopt a Jeans resolution of at least  $\sim 8$  cells per Jeans length. However, substantially higher resolution may be required to properly capture turbulence, dynamo action, and core/disk structure on the Jeans scale. Several studies suggest that at least  $\sim 30$  cells are needed (Sur et al. 2010; Federrath et al. 2011b; Turk et al. 2012), which poses a major computational challenge. Compared to a resolution of 8 cells per  $\lambda_{\rm J}$ , increasing to 30 cells requires  $\sim (30/8)^3 \gtrsim 50$  times more computational resources in 3D. While this is an enormous cost, the investment may be essential for accurately resolving turbulence and magnetic-field amplification. Moreover, systematic tests of core and disk formation, such as those shown in Fig. 5, reveal substantial structural differences with increasing Jeans resolution—for example, significant disk flaring persists when  $\lambda_{\rm J}$  is resolved with  $\lesssim 20$  cells and only disappears at  $\sim 30$  cells per  $\lambda_{\rm J}$ .

## 5.2 Star particles

Since the Jeans resolution criterion (Eq. 25) cannot be upheld indefinitely with rising density during collapse, star particles have become a crucial tool for modeling collapse,

accretion, and star formation. This method is often referred to as 'star particle' or 'sink particle' method (Bate et al. 1995; Krumholz et al. 2004; Federrath et al. 2010a; Hubber et al. 2013; Bleuler and Teyssier 2014). Any code aiming to capture star-forming gas over a significant period of time during accretion and fragmentation will need a sink particle implementation<sup>13</sup>.

## 5.2.1 Sink particle formation

Sink particles are designed to represent star-forming gas undergoing gravitational collapse and accretion. Thus, only bound and collapsing gas should be eligible to form sink particles and be accreted. To enforce this, a control volume must defined around each grid cell that exceeds a density threshold,

$$\rho_{\rm sink} = \frac{\pi c_{\rm s}^2}{4Gr_{\rm sink}^2},\tag{26}$$

which is obtained from Eq. (25) by setting the Jeans length  $\lambda_{\rm J}=2\,r_{\rm sink}$  and solving for the density. Here,  $2r_{\rm sink}$  is the chosen sink particle diameter, which is typically set to 5 grid-cell lengths (corresponding to  $r_{\rm sink}=2.5\,\Delta x$ ) at the maximum refinement level, in order to avoid artificial fragmentation (cf. Sect. 5.1).

Grid cells that exceed the threshold in Eq. (26) must not immediately form sinks. Instead, a sequence of additional checks for collapse and gravitational instability is performed. First, a spherical control volume of radius  $r_{\rm sink}$  is defined, centered on the candidate cell with  $\rho > \rho_{\rm sink}$ . The total gravitational, thermal, kinetic, and magnetic energies ( $E_{\rm grav}$ ,  $E_{\rm th}$ ,  $E_{\rm kin}$ ,  $E_{\rm mag}$ ) are then determined by summation over all cells i within the control volume, evaluated in the reference frame of the central cell, and using the gravitational potential provided by the Poisson solver (Sect. 4.4). A sink particle is only created if the gas within the control volume,

- 1. lies on the highest refinement level (for grid-based codes),
- 2. is not within  $r_{\rm sink}$  of an existing sink particle,
- 3. is converging from all directions, i.e., radial velocity  $v_{r,i} < 0$ ,
- 4. has a minimum of the gravitational potential at its center,
- 5. is gravitationally bound ( $|E_{\rm grav}| > E_{\rm th} + E_{\rm kin} + E_{\rm mag}$ ), and
- 6. is Jeans-unstable.

Grudić et al. (2021) replace condition (iv) with a tidal stability criterion, while Hubber et al. (2013) instead employ a Hill-sphere criterion. Both serve the same purpose of ensuring that the candidate cell lies at the true center of a collapsing region. These checks ensure that only genuinely collapsing, star-forming gas is converted into sink particles.

The density threshold in Eq. (26) alone is insufficient, because local density enhancements can arise in shocks without leading to collapse. Therefore, the cell-bycell Jeans criterion alone is inadequate, since it does not guarantee that sufficient mass

 $<sup>^{13} \</sup>rm For~example,~the~sink~particle~method~implemented~in~FLASH~is~publicly~available~on~GitHub:~https://github.com/chfeder/cfflash$ 

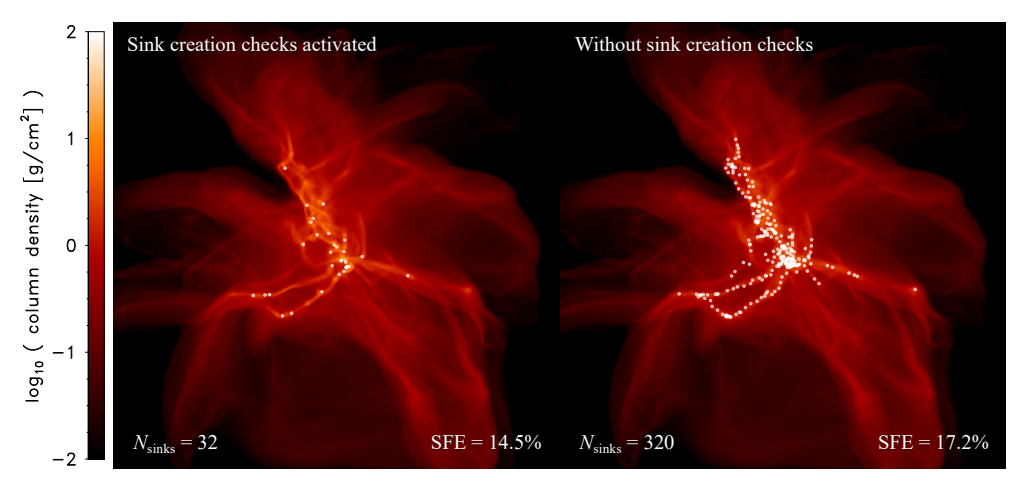


Fig. 6 The importance of sink particle creation checks for identifying truly collapsing regions. Shown are two identical turbulent cloud collapse simulations forming sink particles (shown as white circles): the left-hand panel uses the full set of sink creation checks (Sect. 5.2.1), while the right-hand panel uses only the density threshold criterion in Eq. (26). Without the additional checks,  $10 \times$  more sink particles are created (32 sinks vs. 320). The total stellar mass is also overestimated, with an SFE of 14.5% compared to 17.2%. Figure adapted from Federrath et al. (2010a). An animation of these simulations is available at https://www.mso.anu.edu.au/~chfeder/pubs/sinks/sinks.html.

is contained within the entire Jeans volume to become gravitationally bound. Ensuring collapse requires non-local consistency, as the Jeans length must be resolved by multiple grid cells (see Sect. 5.1).

The implementations by Bate et al. (1995), Federrath et al. (2010a), Hubber et al. (2013), and Bleuler and Teyssier (2014) all adopt the set of creation checks outlined above (with slight variations in the details). By contrast, the sink method of Krumholz et al. (2004) relies solely on the local density criterion  $\rho > \rho_{\rm sink}$  (Eq. 26) for sink formation. As discussed in Federrath et al. (2010a), this single-cell condition is insufficient to ensure that sink-forming gas is both bound and collapsing, and can therefore lead to spurious sink creation.

Figure 6 illustrates this point with two otherwise identical simulations: one with the full set of sink creation checks enabled (left-hand panel), and one using only the density threshold criterion (right-hand panel). In the latter case, the number of sink particles is overproduced by an order of magnitude (10× more sinks), and the total accreted mass is also inflated, yielding a star formation efficiency (SFE) of 17.2% instead of 14.5%. Thus, when adopting the Krumholz et al. (2004) approach, it is critical to choose a sufficiently high density threshold for sink formation, so that collapse and boundedness can be assumed implicitly rather than explicitly tested.

## 5.2.2 Sink particle accretion

In grid/AMR simulations, once a sink particle is created, it can accrete gas from the grid but only if the gas exceeds the density threshold, is inside the sink particle accretion radius, is bound to the particle and more bound to it than to any other, and is collapsing toward it. If all these criteria are fulfilled, the excess mass above the density threshold defined by Equation (26) is removed from the MHD system and added to the sink particle, such that mass, momentum, and angular momentum are conserved. The mass fraction  $\Delta m_i$  to be accreted from cell i with mass  $m_i$  and volume  $V_i$  is  $\Delta m_i = m_i - \rho_{\rm sink} V_i$ . Within the control volume  $(4\pi/3)r_{\rm sink}^3$  of a sink particle, we gather the mass, center of mass (COM), momentum, and angular momentum of the material to be accreted,

$$\begin{aligned} \text{Mass:} \quad & M_{\text{acc}} = \sum_{i} \Delta m_{i} \\ \text{Center of mass:} \quad & \mathbf{R}_{\text{acc}} = \sum_{i} \Delta m_{i} \mathbf{r}_{i} / M_{\text{acc}} \\ \text{Linear momentum:} \quad & \mathbf{P}_{\text{acc}} = \sum_{i} \Delta m_{i} \mathbf{v}_{i} \\ \text{Angular momentum:} \quad & \mathbf{L}_{\text{acc}} = \sum_{i} \Delta m_{i} \mathbf{r}_{i} \times \mathbf{v}_{i}, \end{aligned}$$

where  $\mathbf{r}_i$  and  $\mathbf{v}_i$  are the lab-frame position and velocity of the gas in cell i. We then remove the mass  $\Delta m_i$  from each affected cell and update the sink particle properties — mass  $M_{\rm sink}$ , position  $\mathbf{R}_{\rm sink}$ , linear momentum  $\mathbf{P}_{\rm sink}$ , and angular momentum  $\mathbf{L}_{\rm sink}$  — such that the total mass, center of mass (COM), linear momentum, and angular momentum are conserved. The latter includes both the lab-frame angular momentum of the sink particle,  $\mathbf{L}_{\rm sink}$ , and its intrinsic spin,  $\mathbf{S}_{\rm sink}$ . Denoting post-accretion quantities with a prime, the updated sink properties are

$$\begin{aligned} \operatorname{Mass:} M'_{\operatorname{sink}} &= M_{\operatorname{sink}} + M_{\operatorname{acc}} \\ \operatorname{COM:} \mathbf{R}'_{\operatorname{sink}} &= (M_{\operatorname{sink}} \mathbf{R}_{\operatorname{sink}} + M_{\operatorname{acc}} \mathbf{R}_{\operatorname{acc}}) / M'_{\operatorname{sink}} \end{aligned}$$

$$\operatorname{Linear\ momentum:} \mathbf{P}'_{\operatorname{sink}} &= \mathbf{P}_{\operatorname{sink}} + \mathbf{P}_{\operatorname{acc}}$$

$$\operatorname{Angular\ momentum:} \mathbf{L}'_{\operatorname{sink}} &= \mathbf{R}'_{\operatorname{sink}} \times \mathbf{P}'_{\operatorname{sink}}$$

$$\operatorname{Spin:} \mathbf{S}'_{\operatorname{sink}} &= \mathbf{S}_{\operatorname{sink}} + \mathbf{L}_{\operatorname{acc}} + \mathbf{L}_{\operatorname{sink}} - \mathbf{L}'_{\operatorname{sink}}.$$

$$(28)$$

Here, the spin  $\mathbf{S}_{\mathrm{sink}}$  is required to absorb the excess angular momentum carried by the accreted material. Importantly, this excess is not simply equal to  $\mathbf{L}_{\mathrm{acc}}$ , because the sink position  $\mathbf{R}'_{\mathrm{sink}}$  and momentum  $\mathbf{P}'_{\mathrm{sink}}$ —and thus its orbital angular momentum  $\mathbf{L}'_{\mathrm{sink}}$ —change during the accretion step. The corrective term  $\mathbf{L}_{\mathrm{sink}} - \mathbf{L}'_{\mathrm{sink}}$  accounts for this shift, ensuring exact global angular momentum conservation (see Appendix B in Federrath et al. 2010a).

In SPH codes the accretion criteria are the same (within  $r_{\rm sink}$  and bound to the sink), and additionally satisfies an angular momentum criterion to ensure that it does not have an orbit that takes it outside  $r_{\rm sink}$  (Bate et al. 1995). The mesh-less code GIZMO also requires that the volume element associated with accretion must be smaller than the spherical volume corresponding to  $r_{\rm sink}$  to ensure that it has sufficient spatial resolution to be accreted. The GIZMO sink accretion prescription further introduces a sub-grid reservoir, where the mass to be accreted is first stored and subsequently accreted onto the sink according to the local freefall time (Grudić et al. 2021); this reduces the artifical variability of accreting entire SPH particles of a fixed mass, while avoiding artificially over-smoothing. This problem does not exist in the grid-based method described above, where fraction of accreted material always exactly matches that required to fulfill the Jeans criterion of the collapsing gas. We note that the

grid-based accretion method by Krumholz et al. (2004) is different in that it combines Bondi-Hoyle accretion with accretion of all gas cells exceeding  $\rho_{\rm sink}$ . In practice, Krumholz et al. (2004) find that the Bondi-Hoyle pathway of accretion is usually subdominant compared to the direct accretion method of temporarily-created particles exceeding  $\rho_{\rm sink}$ , and subsequently merged into the main sink doing the accretion. Since all gas above  $\rho_{\rm sink}$  is therefore accreted, without a check for boundedness and collapse, the accretion rate is somewhat overestimated in the Krumholz et al. (2004) method (cf. Fig. 6).

Finally, we note that it has been argued that magnetic flux should also be accreted. Implementing this would require directly modifying the magnetic field whenever a sink particle is created or gains mass. However, none of the existing sink particle methods adopt this approach, in order to avoid complications associated with altering the local magnetic field and the risk of introducing  $\nabla \cdot \mathbf{B}$  errors. Instead, our method leaves  $\mathbf{B}$  unchanged and only accretes mass. The magnetic flux, and thus the associated magnetic pressure and tension, remain on the grid. This is in fact a desirable property: if the magnetic field were accreted, one would need to model its influence on the surrounding gas through sub-resolution prescriptions, which becomes unnecessary when the field is left intact.

## 5.2.3 Sink particle dynamics

With sink particles present there are three types of gravitational interactions that need to be considered:

- (i) the force of the gas on the sink particles (gas→sink),
- (ii) the force of the sink particles on the gas (sink→gas),
- (iii) the force of the sink particles on other sinks (sink↔sink).

Each of these could be treated with distinct methods for calculating the gravitational acceleration. However, we note that (i) and (ii) should be done with the same method, which ensures strict symmetry between the two interactions, otherwise violating linear and angular momentum conservation (Federrath et al. 2011a).

Ideally, all three gravitational interactions are computed by direct N-body summation (see Sect. 4.1) over all sink particles and grid cells or SPH particles, providing the most accurate gravitational acceleration. This is the case for example in the FLASH code<sup>14</sup>. Many other codes only use direct summation for the sink $\leftrightarrow$ sink interaction (iii), while they use the Poisson solver (usually in the form of multi-grid or tree-based; Sect. 4.4) to compute the gas $\rightarrow$ sink and sink $\rightarrow$ gas interactions. Using the Poisson solver first requires that the sink mass is interpolated onto the grid (or treating the sink mass as part of the tree-solve in SPH codes or other mesh-less codes like GIZMO; see Grudić et al. 2021), and then solving the Poisson equation for the combined gas+sink

<sup>&</sup>lt;sup>14</sup>A detail worth noting is that while the sink $\leftrightarrow$ sink interaction is softened with Eq. (19) to capture tight sink-sink orbits as accurately as possible, interactions (i) and (ii) are softened with  $\mathcal{K} = (r/r_{\rm soft})^3$  for  $r \leq r_{\rm soft}$  and  $\mathcal{K} = 1$  for  $r > r_{\rm soft}$ , resulting in a linearly rising gravitational acceleration (Eq. 18) 'inside' the sink particle, as for the purposes of gas $\rightarrow$ sink and sink $\rightarrow$ gas interactions, it is reasonable to approximate the sink as a gaseous object of radius  $r_{\rm sink}$ .

potential (Krumholz et al. 2004; Bleuler and Teyssier 2014). While this has the advantage of speed, i.e.,  $\mathcal{O}(N \log N)$  vs.  $\mathcal{O}(N^2)$ , and simplicity in that one can use the existing Poisson solver, it comes at the price of a substantially smoothed acceleration field in the gas  $\rightarrow$ sink and sink  $\rightarrow$ gas interactions, which can cause inaccuracies in the gas and sink dynamics, especially in regions close to a sink particle, e.g., in the orbits of a sink particle around a dense gas accumulation (Federrath et al. 2010a, 2011a).

For time integration of sink particle positions and velocities, a second-order Leapfrog integrator is commonly employed. This is combined with both velocity- and acceleration-based timestep constraints, which allow close and highly eccentric orbits of sink particles to be resolved without introducing errors such as artificial perihelion shifts. These timestep constraints can, however, become very stringent — particularly for closely approaching sink particles interacting via mechanism (iii) — and may force extremely small timesteps. To alleviate this, a sub-cycling method can be used: the sink $\leftrightarrow$ sink interactions are updated in each sub-cycle, while gas $\rightarrow$ sink and sink $\rightarrow$ gas forces are held fixed until the sub-cycles catch up with the global timestep. The global timestep itself is limited by the CFL condition together with additional timestep constraints, including a gravity-based constraint that accounts only for interactions (i) and (ii) (see implementation details and orbit tests in Federrath et al. 2010a, 2011a).

#### 5.2.4 Sink particle merging

Sink particle merging is available in some implementations of sink particles. For example, in the Krumholz et al. (2004) implementation in ORION, sink particle merging is a key step in modeling sink particle creation and accretion, as their implementation creates many temporary sink particle fragments that then need to undergo merging. In the Federrath et al. (2010a) implementation in FLASH, sink particle merging is optional, as accretion is handled directly with the gas on the grid (see above). If merging is activated, sink particles are only allowed to merge, if they are inside the accretion radii of one another, and if they are gravitationally bound and converging. The merged particle is moved to the center of mass of the merging particles, and their linear and angular momenta are assigned to the merged particle. In GIZMO, sink merging only occurs if the pair has a binary semi-major axis less than  $r_{\rm sink}$  and the secondary is at least 10 times smaller than the primary (Grudić et al. 2021).

Merging can be used to model star formation in extremely dense environments, where stellar merger have been considered a possibility to form massive stars (Zinnecker and Yorke 2007). Under more normal conditions, however, merging is rather unlikely, considering that sink particles are often used to represent individual stars, for which the probability of merging is near zero due to the actual stellar size they represent and the velocity dispersion between forming stars.

## 5.3 Summary of challenges and future directions

Achieving sufficient Jeans resolution is computationally demanding, but essential. At least  $\sim 30$  cells per Jeans length are required to accurately capture key physical processes such as the solenoidal turbulent energy content, the minimum amplification of magnetic fields, and the structure of disks on the Jeans scale (cf. Sect. 5.1).

Rigorous sink particle creation checks are critical to ensure that only bound, collapsing gas forms sinks. Without these checks, spurious sinks can form and the accretion rate may be systematically overestimated (cf. Sect. 5.2.1).

During gas accretion onto sink particles, strict conservation of mass, center of mass, linear momentum, and angular momentum must be maintained. Careful numerical implementation is required to guarantee this conservation (cf. Sect. 5.2.2).

Many implementations combine direct N-body summation for  $\mathrm{sink}\leftrightarrow\mathrm{sink}$  interactions with a grid-based Poisson solver (or a tree solver in particle-based methods) for  $\mathrm{sink}$ -gas coupling. However, in dense gas systems, resolving accurate orbital dynamics requires direct summation of all three interaction channels:  $\mathrm{sink}\leftrightarrow\mathrm{sink}$ ,  $\mathrm{gas}\to\mathrm{sink}$ , and  $\mathrm{sink}\to\mathrm{gas}$  (cf. Sect. 5.2.3).

Together, these criteria define the minimum requirements for robust and physically reliable collapse calculations and sink particle implementations.

Beyond individual star formation, sink (or star) particle methods are also widely used to represent entire star clusters in large-scale simulations of galaxy formation and evolution. In this context, sub-resolution prescriptions are employed to model the properties of the embedded stellar population—including the IMF, chemical composition, and resulting feedback efficiencies—at varying levels of detail. However, significant uncertainties remain in these approaches, owing to the many free parameters involved. We therefore anticipate substantial developments in the coming years, with increasingly sophisticated, multi-faceted models aimed at bridging the gap between small-scale star formation physics and galaxy-scale evolution.

## 6 Stellar feedback

Stars do not only accrete gas, but also eject material, loaded with momentum and energy, and sometimes with species that can enrich and change the chemical composition of the ISM. This stellar feedback is a key process for many reasons. Jet feedback (Sect. 6.2) for instance transports angular momentum away from the accretion disk, allowing stars to accrete more efficiently through the protostellar disk. Radiation feedback in the form of heating (Sect. 6.3) changes the thermodynamic conditions of the parental cloud, suppressing fragmentation of the gas. Stellar winds (Sect. 6.4), ionization (Sect. 6.5), and supernova feedback (Sect. 6.6) can drive powerful outflows and shocks and change the chemical composition of the gas in their surroundings.

Stellar feedback is generally modeled by adding source terms to the RHS of the mass, momentum, and energy equations (Eqs. 1–5). Generally, adding the entire feedback contribution to a single grid cell or particle produces numerical instability, especially when the equations are very stiff. Various prescriptions have been developed to distribute the stellar feedback to gas in the vicinity of the emitting star in a robust and efficient way. Grid-based codes typically add the mass, momentum, and energy to some number of neighboring cells according to a weighting function centered on the stellar location (Offner et al. 2009; Cunningham et al. 2011; Federrath et al. 2014b; Hopkins and Grudić 2019; Mathew and Federrath 2020). Similarly, SPH methods distribute the radiated energy among the nearby particles that are exposed

to the stellar radiation, i.e., have a direct sight-line to the source (Jones and Bate 2018) or insert new cells/particles (Grudić et al. 2021).

## 6.1 Stellar and protostellar evolution

A key requirement for many of these feedback prescriptions is to track the evolution of the unresolved protostar, in order to estimate the stellar radius and stellar luminosity, which is required for modeling radiation feedback. Given the accretion rate (Sect. 5.2.2), the protostar will grow in mass and start deuterium burning, producing accretion luminosity (Nakano et al. 2000). The protostellar evolution phases can be summarized and implemented as (Offiner et al. 2009):

- Phase 0: Pre-collapse The gas continues to collapse but the object has not
  yet reached stellar densities.
- Phase I: No-burning Contraction The object is adiabatically contracting but the central density has not yet reached a temperature of  $1.5 \times 10^6$  K, at which deuterium fusion begins.
- Phase II: Core Deuterium Burning with Fixed  $T_c$  Deuterium fusion begins in the core and the protostar enters a convective phase during which the central core temperature,  $T_c$ , remains constant.
- Phase III: Core Deuterium Burning with Variable  $T_c$  The deuterium in the core is depleted and the protostar contracts further, during which  $T_c$  rises.
- Phase IV: Shell Deuterium Burning Deuterium burning begins in a shell outside the core, as the center continues to contract.
- **Zero Age Main Sequence (ZAMS)** The central temperature reaches 10<sup>7</sup> K, at which point hydrogen fusion begins and the protostar becomes a ZAMS star.

Thus, the protostellar evolution model primarily provides the stellar radius and luminosity during its accretion phase and its main sequence evolution, used for various feedback processes that we describe next.

## 6.2 Protostellar jet and outflow feedback

Observations show that jets and outflows are launched from virtually all young protostar—disk systems, with ALMA now providing unprecedented detail and resolution. Jets and outflows play a central role in star formation: they help explain the low star formation rate and efficiency in turbulent molecular clouds, remove angular momentum from the rotating star-forming core/disk, and reduce the characteristic stellar mass in the IMF by a factor of ~ 3 (Federrath et al. 2014b; Mathew and Federrath 2021; Guszejnov et al. 2021). In addition, outflows can significantly contribute to driving and sustaining turbulence in star-forming regions (e.g., Li and Nakamura 2006; Nakamura and Li 2007; Nakamura et al. 2011; Offner and Chaban 2017; Lebreuilly et al. 2024), suggesting that star formation may in part regulate itself through outflow feedback. However, accurately incorporating jets and outflows into numerical simulations of star cluster formation remains a major challenge. To date, only a few codes include subgrid models for jet feedback (FLASH, GIZMO, ORION), each with varying

levels of detail. Below we summarize how jet feedback can be implemented as a sub-resolution module, following the methods of Federrath et al. (2014b), and implemented in FLASH.

In this implementation, outflows are launched along the sink particle angular momentum vector once accretion has been calculated, consistent with the modular design of the code. The accretion and outflow modules are thus separated, with the outflow module directly depending on the accretion step but not vice versa. This ensures that in each timestep the system state after accretion is fully determined before outflow feedback is applied, allowing a prescribed fraction of the accreted material to be re-inserted and launched in bipolar outflows. Two loops over all sink particles and their surrounding grid cells (within the outflow radius; see details below) are required: the first gathers information about the cells that will host outflow injection, and the second updates the state variables to launch the outflows. In this way, the conservation of mass, momentum, and angular momentum is strictly maintained.

## 6.2.1 Geometry of the outflow launching region

Figure 7 illustrates the sub-resolution outflow model of Federrath et al. (2014b), implemented in FLASH (see Sect. 6.2.5). The outflow is launched through two spherical sectors of radius  $r_{\rm out}$  and opening angle  $\theta_{\rm out}$ , aligned with the spin axis of the sink particle,  $\mathbf{S}_{\rm sink}$ . We refer to these regions as the top and bottom 'outflow sectors'.

Observations and theoretical models indicate that outflows align with the rotation axis of the accretion disk (Appenzeller and Mundt 1989). In our model, the sink spin — acquired through the accretion of angular momentum (see Sect. 5.2.2) — serves as a proxy for the unresolved disk spin axis. Although the opening angle is, in principle, a user-defined parameter, adopting  $\theta_{\text{out}} = 30^{\circ}$  is consistent with magneto-centrifugal acceleration of the jet component (Blandford and Payne 1982), and this value is therefore used as the default in our sub-resolution model.

#### 6.2.2 Outflow mass transfer

The outflow model reinserts a fixed fraction of the accreted mass and launches it away from the sink particle to represent the outflow+jet component. The outflow mass  $M_{\rm out}$  inserted in each timestep  $\Delta t$  is determined by the sink accretion rate  $\dot{M}_{\rm acc}$ ,

$$M_{\rm out} = f_{\rm m} \, \dot{M}_{\rm acc} \, \Delta t, \tag{29}$$

where  $f_{\rm m}$  is a user-defined parameter. Theory, observations, and numerical simulations all suggest  $f_{\rm m} \sim 0.1-0.4$  (Matzner and McKee 2000; Cunningham et al. 2011; Federrath et al. 2014b, and references therein). In the FLASH implementation discussed here, we adopt  $f_{\rm m}=0.3$  as a reasonable standard value. The results, however, are largely insensitive to the precise choice of  $f_{\rm m}$ , owing to the self-regulating nature of accretion—outflow coupling: if  $f_{\rm m}$  is increased,  $\dot{M}_{\rm acc}$  is temporarily reduced, which in turn weakens the outflow until accretion resumes, thus establishing a self-regulated balance.

In practice, after each accretion step the outflow mass  $M_{\rm out}$  is computed, subtracted from the sink particle, and deposited into the gas within the outflow sectors,

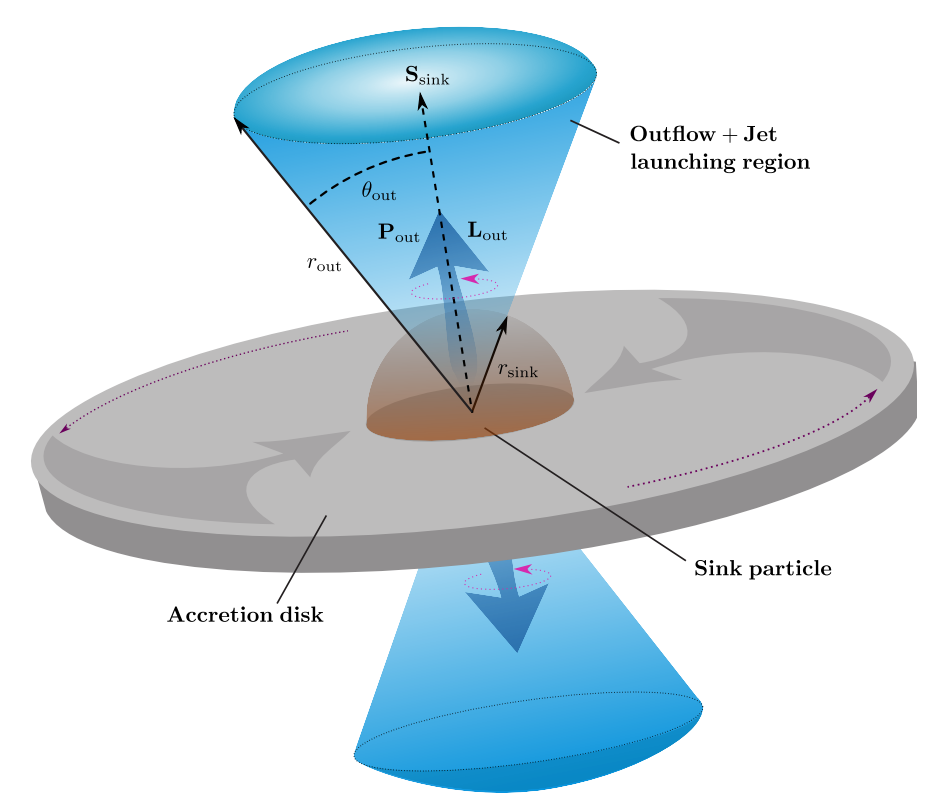


Fig. 7 Schematic (not to scale) of the sub-resolution outflow+jet model by Federrath et al. (2014b), showing the basic geometry with the sink particle radius  $r_{\rm sink}$ , sink spin  ${\bf S}_{\rm sink}$ , outflow radius  $r_{\rm out}$ , outflow opening angle  $\theta_{\rm out}$ , outflow linear momentum  ${\bf P}_{\rm out}$ , and outflow angular momentum  ${\bf L}_{\rm out}$ . The upper and lower components of the outflow region are shown as the two spherical sectors in blue, for the which the symmetry axis is defined by  $\mathbf{S}_{\mathrm{sink}}.$ 

ensuring mass conservation. To achieve a smooth transition at the boundary of the launching region (defined by  $r_{\text{out}}$  and  $\theta_{\text{out}}$ ), we apply radial and angular smoothing functions,

$$\mathcal{R}(r, r_{\text{out}}) = \begin{cases} \sin[\pi(r/r_{\text{out}})] & \text{for } r \leq r_{\text{out}} \\ 0 & \text{for } r > r_{\text{out}} \end{cases}, \tag{30}$$

$$\mathcal{R}(r, r_{\text{out}}) = \begin{cases}
\sin[\pi(r/r_{\text{out}})] & \text{for } r \leq r_{\text{out}} \\
0 & \text{for } r > r_{\text{out}}
\end{cases},$$

$$\Theta(\theta, \theta_{\text{out}}) = \begin{cases}
\cos^{p}[(\pi/2)(\theta/\theta_{\text{out}})] & \text{for } |\theta| \leq \theta_{\text{out}} \\
0 & \text{for } |\theta| > \theta_{\text{out}}
\end{cases},$$
(30)

with p=1 as the default smoothing power. These functions quickly approach zero at the edges of the outflow sectors, preventing sharp discontinuities. The resulting outflow morphology is insensitive to the exact choice of p as long as  $p \leq 4$ . While the model would in principle function without smoothing, the application of these functions avoids numerical instabilities near the sector boundaries.

#### 6.2.3 Outflow momentum transfer

The momentum transferred to each of the two outflow sectors in the rest frame of the sink particle is  $\mathbf{P}_{\text{out}} = \pm M_{\text{out}} \mathbf{v}_{\text{out}}/2$ , where  $M_{\text{out}}$  is the outflow mass (Eq. 29). For the radial outflow velocity  $\mathbf{v}_{\text{out}}$ , we adopt the Keplerian speed at the foot-point of a centrifugally-driven jet, close to the protostellar radius, as suggested by analytic models (Blandford and Payne 1982; Shibata and Uchida 1985, 1986; Pudritz and Norman 1986; Wardle and Königl 1993; Königl and Pudritz 2000). The resulting outflow velocity is

$$|\mathbf{v}_{\text{out}}| = \left(\frac{GM_{\text{sink}}}{10\,\text{R}_{\odot}}\right)^{1/2} \mathcal{V}(\theta/\theta_{\text{out}}) = 100\,\text{km}\,\text{s}^{-1} \left(\frac{M_{\text{sink}}}{0.5\,\text{M}_{\odot}}\right)^{1/2} \mathcal{V}(\theta/\theta_{\text{out}}), \quad (32)$$

which depends on the sink mass  $M_{\rm sink}$  and on the two-component jet+outflow profile  $\mathcal{V}(\theta/\theta_{\rm out})$  defined below.

Observations and jet-launching simulations (e.g., Camenzind 1990; Machida et al. 2008; Machida and Basu 2019) consistently show that outflows exhibit two components: a fast, collimated jet and a slower, wide-angle outflow. To capture both, we adopt a normalized velocity profile based on the angular smoothing function  $\Theta(\theta/\theta_{\text{out}})$  from Eq. (31),

$$\mathcal{V}(\theta, \, \theta_{\text{out}}) = \frac{3}{4} \, \Theta(\theta, \, \theta_{\text{out}}/6) + \frac{1}{4} \, \Theta(\theta, \, \theta_{\text{out}}), \tag{33}$$

where the first term represents the fast collimated jet and the second term the slower wide-angle outflow. Momentum transfer is implemented symmetrically between the two sectors to ensure exact global momentum conservation.

#### 6.2.4 Outflow angular momentum transfer

Outflows and jets are observed to rotate (Bacciotti et al. 2002), making them a key mechanism for transporting angular momentum away from the protostar and its disk, thereby enabling the star to grow in mass (Uchida and Shibata 1985; Shu et al. 1987; Königl and Pudritz 2000; Pudritz et al. 2007; Frank et al. 2014). Similar to the mass transfer described in Sect. 6.2.2, we introduce a fraction  $f_a$  of the accreted angular momentum,  $\mathbf{S}'_{\text{sink}} - \mathbf{S}_{\text{sink}}$  (from Eq. 28), which is released along the sink particle's rotation axis  $\mathbf{S}'_{\text{sink}}$  after each accretion event. This fraction of angular momentum is transferred to the two outflow sectors as

$$\mathbf{L}_{\text{out}} = f_{\text{a}} \left( \mathbf{S}'_{\text{sink}} - \mathbf{S}_{\text{sink}} \right) \frac{\mathbf{S}'_{\text{sink}}}{|\mathbf{S}'_{\text{sink}}|}.$$
 (34)

Observationally, Bacciotti et al. (2002) used Hubble Space Telescope data of the DG Tau flow to infer angular momentum fractions of  $f_a = 0.6 - 1.0$ . This range is consistent with predictions from disk-wind models (Pelletier and Pudritz 1992), which yield  $f_a \sim 0.7 - 1.0$  for sub- to super-Alfvénic accretion flows. Numerical simulations further support these values: Banerjee and Pudritz (2006) and Hennebelle and Fromang (2008) measured  $f_a \sim 0.5 - 2$ , with a time-averaged value of  $f_a \sim 0.9$ . This agrees well with the observations of Bacciotti et al. (2002). Based on these findings, we adopt

 $f_{\rm a}=0.9$  as the standard value in the jet+outflow model in FLASH, resulting in 90% of the accreted angular momentum re-injected in the outflow sectors and removed from the disk-protostar system — a physically reasonable choice for magnetically-driven jets and outflows (Pudritz et al. 2007). This prescription ensures angular momentum is consistently removed from the accreting system, in agreement with both observations and theoretical expectations.

#### 6.2.5 Implementation, code validation, and access

The practical implementation of the outflow module in FLASH, as described above, requires two loops over all grid cells, with each loop iterating over all sink particles. The first grid loop is used to gather information from the cells within the two outflow sectors and to 'test-insert' the outflow mass, momentum, and angular momentum. In this stage, the state variables of the gas cells and the sink particles are not yet modified; instead, the collected information is used to ensure that all conservation laws can be satisfied exactly. The second grid loop then updates the gas cell properties to inject the outflowing mass, momentum, and angular momentum.

It is worth noting that no additional smoothing of the momentum and angular momentum injection is required, because both are proportional to the injected mass, which is already smoothed via Eqs. (30) and (31). Finally, the sink particle properties are updated to guarantee global conservation. As in the case of accretion, strict conservation requires slight repositioning of the sink particles driving outflows in order to satisfy two major constraints: (i) global conservation of the center of mass (COM), and (ii) ensuring that the linear momentum components injected into the two outflow sectors are parallel.

The sink particle outflow module implemented in FLASH is publicly available on GitHub<sup>15</sup>. The module has been calibrated, tested, and validated against dedicated resolved jet/outflow simulations in Federrath et al. (2014b). Key features of the method include:

- convergence of fundamental outflow properties (mass, linear and angular momentum, and jet speed) for a sufficiently resolved outflow radius,  $r_{\rm out} \gtrsim 16\Delta x$ , i.e.,  $\sim 32$  cells in diameter,
- a systematic quantification of the impact of the default parameter choices for  $f_{\rm m}$  and  $f_{\rm a}$ , demonstrating the self-regulation of the outflow-accretion system, and
- built-in adaptivity of the sub-resolution model to changes in the absolute resolution scale of a simulation.

Adopting the open-source outflow module from FLASH in other codes is straightforward, owing to its design, which cleanly separates the accretion and outflow steps. As a result, the module only requires the sink particle properties after accretion, which then serve as input for the outflow injection.

<sup>&</sup>lt;sup>15</sup>Sink particle jet/outflow module in the FLASH code: https://github.com/chfeder/cfflash

## 6.2.6 Comparison of jet/outflow implementations

The first outflow model applied to star cluster formation was developed by Li and Nakamura (2006) and Nakamura and Li (2007). In their approach, a Lagrangian particle was created once the gas density exceeded 100 times the mean density. Twenty percent of the mass in a cubic region surrounding the particle was then transferred to it, without modeling subsequent accretion. Their feedback consisted of isotropic, radial point explosions, later extended by Nakamura and Li (2007) to include a collimated component with an opening angle of 30°. In this model, the outflow axis was aligned with the local magnetic field vector—a choice that may inadvertently couple to the wound-up toroidal component of the disk field. Angular momentum transfer was not included.

Wang et al. (2010) and Nakamura and Li (2011) improved on these early models by adding accretion onto sink particles. However, the outflow axis remained tied to the local magnetic field, and angular momentum transfer was still omitted. Dale and Bonnell (2008) studied isotropic and collimated winds in massive star formation using SPH, but their prescription was not adaptive. In contrast, the model of Cunningham et al. (2011) launched outflows along the rotation axis of the sink particles, scaling the outflow mass and momentum with the sink accretion rate. Nevertheless, their model also neglected angular momentum transfer, likely underestimating the overall outflow impact.

The outflow model by Federrath et al. (2014b) explicitly includes angular momentum transfer (see Sect. 6.2.4), a process that is highly efficient and likely the dominant mechanism for removing angular momentum from protostellar disks. It was tested against fully-resolved simulations of magnetized protostellar collapse and disk formation, with convergence studies demonstrating robustness. The model reproduces realistic mass, momentum, and energy injection rates, as well as jet velocities, even at resolutions  $\sim 1,000$  times lower than would otherwise be required in the absence of a sub-resolution prescription.

A more recent implementation by Grudić et al. (2021) in the GIZMO code adopts methods broadly similar to Federrath et al. (2014b), but omits angular momentum injection. Their rationale is that angular momentum must already be shed by the disk before material accretes onto the star, and thus does not need to be explicitly injected back into the outflow. However, because the disk is generally unresolved in large-scale simulations, this argument overlooks part of the physics intended to be captured by a sub-resolution model. In particular, the Federrath et al. (2014b) scheme returns angular momentum to larger scales through the jets, while the Grudić et al. (2021) implementation does not, potentially underestimating feedback effects on cluster-scale dynamics.

#### 6.3 Protostellar heating feedback

Accreting protostars radiate both through their intrinsic stellar luminosity, powered by nuclear burning, and through their accretion luminosity, which arises from the energy released by in-falling material. Most of the accretion luminosity is generated in shocks at the stellar surface and can be expressed as a function of the instantaneous

stellar mass  $M_{\star}$  and radius  $R_{\star}$ ,

$$L_{\rm acc} = f_{\rm acc} \frac{GM_{\star}\dot{M}_{\star}}{R_{\star}},\tag{35}$$

where  $\dot{M}_{\star}$  is the accretion rate and  $f_{\rm acc}$  is a coefficient of order unity that specifies the fraction of kinetic energy radiated away rather than expended to drive jets or retained by the star.

Offner et al. (2009) introduced a detailed one-zone protostellar evolution model that follows the nuclear state of the star and tracks its radius as a function of mass and accretion history (cf. Sect. 6.1). When full radiation transfer (RT) is included in a simulation (Sect. 7), the resulting bolometric luminosity can be incorporated directly as a source term on the RHS of the RT equation (e.g., Offner et al. 2009; Klassen et al. 2012; Bate 2012; Grudić et al. 2021; Menon et al. 2022).

A simpler way to model stellar heating, without solving the full RT problem, is to modify the gas temperature directly. Assuming the protostar radiates as a blackbody, the heating temperature profile can be written as

$$T_{\text{heat}}^4(r) = \frac{L_{\text{acc}}}{4\pi\sigma_{\text{SB}}r^2},\tag{36}$$

with  $\sigma_{\rm SB}$  the Stefan–Boltzmann constant (Stamatellos et al. 2012). Mathew and Federrath (2020) extended this approach by relaxing the assumption of spherical symmetry and implementing a sub-resolution model that includes the accretion disk. This captures the effect of the asymmetric dust distribution on the circumstellar temperature. The orientation of the sub-resolution disk is aligned with the sink particle spin axis  $\mathbf{S}_{\rm sink}$ , as in the outflow module (cf. Fig. 7). The resulting accretion- and protostar-induced luminosity yields an effective heating temperature  $T_{\rm heat}(r,\theta)$  that depends on both distance from the star r and polar angle  $\theta$  (Mathew and Federrath 2020)<sup>16</sup>.

Finally, this heating temperature is incorporated into the EOS (Sect. 2.1.2) of the MHD system by modifying the thermal pressure (Guszejnov et al. 2016; Federrath et al. 2017; Mathew and Federrath 2020),

$$p_{\rm th} \rightarrow \left[ p_{\rm th}^4 + \left( \frac{\rho k_{\rm B} T_{\rm heat}}{\mu m_{\rm H}} \right)^4 \right]^{1/4}$$
 (37)

Figure 8 demonstrates how stellar heating alters the IMF<sup>17</sup>. In the simulations of Bate (2012), a simple polytropic EOS produces an excess of low-mass objects, while including RT in the flux-limited-diffusion (FLD) approximation suppresses their

 $<sup>^{16}</sup>$  The protostellar heating method implemented in the FLASH code is publicly available on GitHub: https://github.com/chfeder/cfflash  $^{17}$  Note that the modified Kroupa (2001) and Chabrier (2005) IMFs shown in Fig. 8 are primarily intended

<sup>&</sup>lt;sup>17</sup>Note that the modified Kroupa (2001) and Chabrier (2005) IMFs shown in Fig. 8 are primarily intended as illustrative guides, not for direct comparison with the simulation data. The low-mass end of the IMF remains uncertain due to systematics related to binaries, incompleteness, and luminosity-to-mass conversions (Chabrier 2003; Kroupa et al. 2013; Hopkins 2018). Ongoing debate continues regarding the most appropriate form of the IMF in different environments, with recent reviews and discussions provided by Kroupa et al. (2026), Gjergo et al. (2025), and Jerabkova et al. (2025).

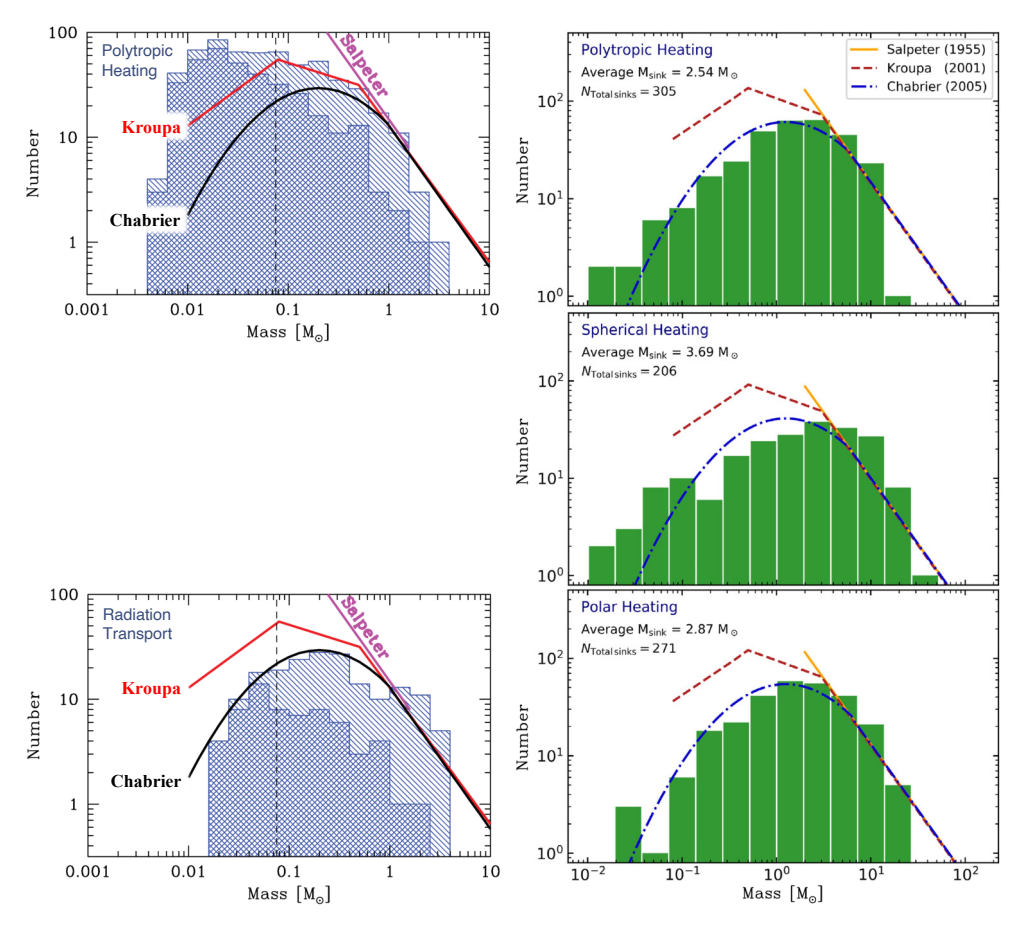


Fig. 8 Impact of protostellar heating on the initial mass function (IMF). Left: sink particle mass distributions from Bate (2012), comparing a polytropic EOS (top) with RT in the FLD approximation (bottom). Right: simulations from Mathew and Federrath (2020), using the same polytropic EOS (top), spherical heating feedback (middle), and polar heating feedback (bottom). Without RT, or with only simple spherical heating, the number of low-mass stars is strongly overestimated. By contrast, RT and polar heating both suppress spurious low-mass stars. Polar heating provides a computationally efficient approximation to RT for low-mass star formation, but the IMF peak mass (here  $\sim 1\text{--}2\,\mathrm{M}_\odot$ ) remains too high due to the neglect of additional feedback processes, especially jets and outflows. For clarity, the IMFs of Salpeter (1955), Kroupa (2001), and Chabrier (2005) are shifted to highlight shape differences.

formation. A similar trend is seen in the simulations of Mathew and Federrath (2020): spherical heating feedback reduces the overall fragmentation but still overproduces low-mass stars, whereas polar heating, which accounts for disk shielding, yields an IMF much closer to the RT case. Nonetheless, the IMF peak mass ( $\sim 1-2\,\mathrm{M}_\odot$ ) is clearly overestimated, underscoring the importance of additional processes such as jet and outflow feedback (cf. Mathew and Federrath 2021; Guszejnov et al. 2021, 2022; Mathew et al. 2023, 2025).

In summary, the primary impact of stellar heating is the suppression of small-scale fragmentation, particularly within protostellar accretion disks (Krumholz et al. 2007a; Offner et al. 2010; Jones and Bate 2018). A similar effect can be partially reproduced by radiative trapping at high densities, even without explicitly modeling stellar feedback (Bate 2009b, 2012). Episodic accretion, during which intervals of efficient cooling occur, may mitigate radiative heating and allow disk fragmentation to proceed (Stamatellos et al. 2012). Nevertheless, the microphysics of disk accretion remains poorly understood, and direct simulations of turbulent disk dynamics are currently beyond the resolution limits achievable in star-cluster calculations.

### 6.4 Stellar wind feedback

Many simulation codes include sub-resolution models for radiatively driven mass loss from main-sequence (MS) and post-MS stars. Stellar winds from massive stars are a major source of nuclear-processed heavy elements and, after supernovae, represent the second most important channel of energy and momentum injection into the ISM (Smith 2014). In contrast to protostellar outflows, stellar winds are relatively straightforward to implement: they are intrinsically spherical, contribute little angular momentum, and can be benchmarked against analytic models of wind-bubble evolution (Weaver et al. 1977; Koo and McKee 1992; Lancaster et al. 2021a). While some uncertainty remains regarding the details of the mass-loss process—particularly for late B- and A-type stars—the general launching mechanisms and the dependence of wind properties on stellar mass and metallicity are well established (Cure and Araya 2023).

Despite the central role of radiation pressure in driving stellar winds, most numerical prescriptions do not explicitly model radiation transport or radiation pressure. Instead, mass, momentum, and energy are injected directly into the computational domain, analogous to the treatment of SNe (see Sect. 6.6). Mass-loss rates, wind velocities, and temperatures are typically adopted from stellar evolution models or empirical fits to observational data. In SPH and hybrid methods, winds are implemented by spawning new particles or cells at the source location (Dale and Bonnell 2008; Price et al. 2018; Grudić et al. 2021).

In mesh-based methods, the injected mass, momentum, and energy are deposited into a spherical region using a predefined stencil (Offner and Arce 2015; Geen et al. 2015b; Gatto et al. 2017; Lancaster et al. 2021b). The injection region must be sufficiently large to resolve spherical expansion. To model winds more realistically, Lancaster et al. (2021b) introduced a hybrid thermal/kinetic energy scheme that interpolates between thermal energy—dominant near the source—and kinetic energy, which dominates at the shell edge. In addition, modifications to the CFL timestep criterion may be required to enhance stability and avoid numerical overshoot in the amount of injected feedback (Grudić et al. 2021).

Simulations that include stellar winds show that they generate a complex, fractal ISM structure, which in turn shapes the environment for subsequent SN explosions (Rogers and Pittard 2013; Walch and Naab 2015; Geen et al. 2015b). Feedback from winds of intermediate-mass stars contributes to driving and sustaining turbulence within molecular clouds (Offner and Liu 2018). For massive stars, stellar winds play

a key role in halting ongoing star formation and dispersing the natal gas reservoirs of their parent clouds (Guszejnov et al. 2022).

#### 6.5 Ionization feedback

Ionization regulates accretion and strongly shapes the natal environments of massive stars (Kuiper and Hosokawa 2018). As with stellar winds, ionization feedback is primarily important for high-mass stars. Several methods implement ionization feedback from star particles by computing the instantaneous ionizing flux they emit (Rosen et al. 2020). Because the Strömgren radius depends on the local gas number density, the effects of ionization can be approximated without solving the full RT problem. For example, Dale et al. (2007) compute the ionization front radius around a source, identify which nearby SPH particles lie within it, and reset their temperatures to  $10^4$  K, the approximate equilibrium temperature of ionized hydrogen.

More detailed approaches couple ionization feedback to stellar evolution models (Sect. 6.1), estimating the ionizing photon flux from the stellar spectrum and computing the gas response via ray-tracing or other RT schemes (Peters et al. 2010; Geen et al. 2015b; Grudić et al. 2021, see Sect. 7). In clustered environments, photoionization may even trigger secondary star formation, although this remains difficult to confirm observationally (Dale et al. 2013). On larger scales, photoionization plays a central role in dispersing molecular clouds and in reducing star formation efficiencies to  $\lesssim 10\%$  (Geen et al. 2016, 2017; Kim et al. 2018, 2021; Grudić et al. 2022; Guszejnov et al. 2022; Menon et al. 2023). The combined influence of ionizing radiation and jets has also recently been studied in Verliat et al. (2022), showing that both are crucial ingredients for massive cluster formation and evolution.

## 6.6 Supernova feedback

Supernova (SN) explosions are a critical component of star formation and galaxy evolution. They shape the multi-phase ISM, regulate the rate and efficiency of star formation (McKee and Ostriker 1977), and are among the dominant drivers of large-scale ISM turbulence (e.g., Mac Low and Klessen 2004; Tamburro et al. 2009; Padoan et al. 2016; Pan et al. 2016; Beattie et al. 2025c). Consequently, most star formation codes include some prescription for SN energy, momentum, and mass injection (see Table 1). In contrast to many other feedback processes, SN sub-resolution models can be benchmarked directly, since SNe evolve through a sequence of well-characterized phases, including the energy-conserving Sedov-Taylor phase (Taylor 1950; Sedov 1959; Book 1994).

While the underlying physics of the blast wave is well understood, numerical implementations face several challenges and adopt varying approaches. Most models assume a fiducial explosion energy of  $E_{\rm SN}=10^{51}\,{\rm erg}$ , with all stars above  $M_{\star}>8\,M_{\odot}$  ending their lives as SNe. The relative fractions of thermal and kinetic energy that make up  $E_{\rm SN}$  depend on the evolutionary phase being modeled and, critically, on how well the injected blast wave is resolved numerically. Energy, momentum, and ejecta mass are typically deposited within the local region surrounding the explosion, either by spawning new SPH particles or by distributing mass and energy across a group of grid

cells with some weighting kernel (Walch and Naab 2015; Haid et al. 2016; Kim and Ostriker 2017; Hopkins et al. 2018; Grudić et al. 2021).

Special care is required to ensure that the injected feedback converges toward the analytic Sedov–Taylor solution. If mass and energy are deposited into too large a region, the explosion is artificially underpowered; if deposited into too small a region, the injected thermal energy may radiate away before driving expansion (Hu et al. 2016; Hopkins et al. 2018). To maintain numerical stability and load-balancing, some methods distribute the injection over several timesteps (Grudić et al. 2021). It is also essential to enforce isotropy, ensuring that the feedback does not introduce spurious momentum anisotropies or directional biases in the expanding blast wave (Bruls et al. 1999; Hopkins et al. 2018). Accurate SN feedback is therefore central to galaxy-scale simulations, where it sets the ISM structure and controls star formation efficiencies.

## 6.7 Summary of challenges and future directions

Star formation feedback relies heavily on sub-resolution modeling. Key ingredients include protostellar evolution models that track stellar radii and luminosities during accretion and onto the ZAMS (Sect. 6.1). Outflows and jets must be included in simulations aiming to converge on the star formation rate (SFR) and the initial mass function (IMF): without them, both the SFR and the characteristic stellar mass are overestimated by factors of  $\sim 2-3$ . Remarkably, although angular momentum transport via protostellar jets is essential for enabling accretion and likely represents the primary solution to the angular momentum problem, only one of the three codes that currently support sub-resolution jet models coupled to dynamic star particles includes angular momentum injection (Sect. 6.2).

Additional advances have been made in simplified treatments of stellar heating feedback (Sect. 6.3), which avoid the full radiation transport problem. Such approaches provide efficient approximations while still suppressing spurious fragmentation. Whereas jets and heating are relevant for stars of all masses, winds (Sect. 6.4), ionization (Sect. 6.5), and supernova (SN) feedback (Sect. 6.6) primarily affect massive stars. Wind models are comparatively straightforward due to their spherical symmetry and relatively well-constrained physical background. Ionization and SN blast-wave physics are also well understood, but ionization feedback ideally requires radiation transport (see Sect. 7), while SN feedback remains sensitive to the resolution scale and to how energy and momentum are partitioned between thermal and kinetic components.

Future developments aim to improve the robustness and physical fidelity of these feedback models. For SN feedback in particular, new approaches seek to initialize profiles based on the analytic Sedov–Taylor solution, while incorporating the correct timing, expansion phase, and the structure of the surrounding medium. Similarly, more comprehensive implementations of jet feedback, including angular momentum transport, and improved sub-resolution treatments of stellar heating will be critical. These advances are essential not only for realistic star cluster simulations, but also for bridging the gap to galaxy-scale studies where feedback regulates star formation and drives the multiphase ISM.

## 7 Radiation hydrodynamics

A defining characteristic of stars is that they shine. Forming stars heat their natal gas, and young massive stars ( $\gtrsim 8\,\mathrm{M}_\odot$ ) further shape their environment through ionization and radiation pressure (Rosen et al. 2020). In many regimes, the energy and momentum carried by radiation are comparable to those of the gas, making radiation-matter interactions critical for modeling star formation.

Radiation hydrodynamics (RHD), however, remains one of the most difficult areas of computational astrophysics, both numerically and computationally. All current simulations rely on approximations of the full equations. Many studies omit radiation transfer (RT) altogether, replacing it with simplified heating and cooling prescriptions such as modified equations of state or pre-computed tables. These can be adequate in some regimes but fail in others—notably in massive star formation, where RT is essential.

It is useful to distinguish RT from radiation feedback. Radiation transport describes how photons propagate and interact with matter, while radiation feedback refers to emission from stars or clusters, which may or may not be coupled to detailed RHD. In simulations that include RHD, feedback typically enters as a source term for radiation energy and flux.

In this section, we review RHD methods<sup>18</sup> used in star-formation modeling. We outline the relevant physical regimes, opacity treatments, and the role of laboratory, co-moving, and mixed frames. We then present the basic RT equations, discuss ray-tracing, and derive the moment equations with three closures: flux-limited diffusion (FLD), moment-1 (M1), and variable Eddington tensor (VET). Section 7.5 summarizes advances in Monte Carlo radiation transport (MCRT), and we conclude with a direct comparison of MCRT, FLD, M1, and VET in Sect. 7.6.

## 7.1 Optically-thin vs. optically-thick regimes

Consider a system of size  $\ell$  with velocity v and photon mean free path  $\lambda_{\rm mf}$ . The hydrodynamic flow time is  $\ell/v$ , while the mean time between photon-matter interactions is  $\lambda_{\rm mf}/c$ . The optical depth is  $\tau = \ell/\lambda_{\rm mf}$ . In the optically-thin limit,  $\tau \ll 1$  (streaming limit), radiation propagates freely at  $\sim c$ , decouples from the gas, and escapes, allowing efficient cooling. Here isothermality is often a good approximation, since local heat (e.g., by shocks or dissipation) is quickly radiated away.

In contrast, for  $\tau \gg 1$  (diffusion limit), gas and radiation are tightly coupled, photons undergo many scatterings, and radiation propagates diffusively, much slower than c. Radiation becomes effectively 'trapped' in the material, leading to local heating.

The diffusion limit can be subdivided depending on the importance of gas motion (Mihalas and Mihalas 1984). In the static diffusion limit ( $\beta \tau \ll 1$ , with  $\beta = v/c$ ), radiation and gas are strongly coupled and flows are non-relativistic. In the dynamic diffusion limit ( $\beta \tau \gg 1$ ), radiation is advected with the gas, and terms describing advection and radiation work dominate over emission and absorption. Even non-relativistic systems with extreme  $\tau$ , such as stellar interiors ( $\tau \sim 10^{11}$ ), can enter

<sup>&</sup>lt;sup>18</sup>A recent review on RT methods for star formation is provided by Wünsch (2024).

this regime. For most star-formation problems—dense cores and accretion disks—conditions lie in the static diffusion limit (Krumholz et al. 2007b). Jets and outflows, however, carve low-density polar cavities (cf. Sect. 6.2), making the pure diffusion approximation inaccurate in those directions.

In present-day star-forming regions (unlike in the primordial Universe), dust dominates the opacity, which depends on frequency and temperature (Semenov et al. 2003). As a result, mean opacities vary by orders of magnitude: dense cores are typically optically thick, while diffuse cloud regions remain optically thin. Accurate RT methods must therefore treat both regimes and, crucially, the transition between them.

#### 7.1.1 Opacities

A central ingredient in radiation transfer is the opacity,  $\kappa_{\nu}$ , which determines how radiation interacts with matter. Opacities are intrinsically frequency-dependent, reflecting the microphysical absorption and scattering processes relevant at different photon energies. For practical applications, these frequency-dependent opacities are often averaged to produce a single effective value. Two of the most common averages are the *Planck mean opacity*,

$$\kappa_{\rm P}(T) = \frac{\int_0^\infty \kappa_\nu B_\nu(T) \, d\nu}{\int_0^\infty B_\nu(T) \, d\nu},\tag{38}$$

and the Rosseland mean opacity,

$$\kappa_{\rm R}(T) = \frac{\int_0^\infty \frac{\partial B_{\nu}(T)}{\partial T} d\nu}{\int_0^\infty \kappa_{\nu}^{-1} \frac{\partial B_{\nu}(T)}{\partial T} d\nu}.$$
 (39)

Here  $B_{\nu}(T)$  is the Planck function. The Planck mean  $\kappa_{\rm P}$  weights the opacity by the local emissivity spectrum and is most relevant when describing absorption of stellar or thermal emission. The Rosseland mean  $\kappa_{\rm R}$ , by contrast, weights low-opacity windows more strongly and is appropriate in the diffusion limit, where radiative flux is carried preferentially through the most transparent frequency channels. Both averages are widely used in RHD simulations, depending on the physical regime.

In present-day star-forming regions, dust provides the dominant source of opacity. The effective dust opacity depends on grain size, composition, and shape, and varies strongly with frequency (Semenov et al. 2003). In practice, many studies employ precomputed, tabulated dust opacities as functions of temperature and density (e.g., Semenov et al. 2003), which implicitly capture frequency-averaged effects, i.e., they provide  $\kappa_{\rm P}(T)$  and  $\kappa_{\rm R}(T)$ .

Different physical regimes require different opacity prescriptions. For example, in primordial (Population III) star formation, where metals and dust are absent, the relevant opacities arise from bound-free and free-free transitions and electron scattering. The main contributors in this case are atomic H, He, and molecular  $H_2$  (via rovibrational lines), with Thomson scattering becoming important at high temperatures (Mayer and Duschl 2005).

At photon energies above the Lyman limit ( $h\nu > 13.6\,\mathrm{eV}$ ), ionizing radiation dominates. Here, the key opacity sources are the photoionization cross sections of neutral hydrogen and helium (Verner et al. 1996; Osterbrock and Ferland 2006). These frequency-dependent cross sections set the structure of ionization fronts and determine the coupling between radiation and gas in H II regions around massive stars. Simulations of reionization and stellar feedback therefore typically adopt tabulated H and He opacities, augmented by Thomson scattering for the highest photon energies (Sharda and Menon 2025).

Thus, while dust dominates most present-day star-forming environments, opacity physics is highly problem-dependent. Accurate modeling requires not only capturing the correct frequency dependence, but also adopting the relevant opacity sources for the environment under consideration. Moreover, the frequency dependence of the opacity introduces challenges related to the choice of reference frame in which to formulate the relevant equations.

### 7.1.2 Laboratory, co-moving, and mixed reference frames

The difficulty of solving the RT can be reduced both by approximations and by choosing a suitable frame. In the laboratory frame the observer is at rest, while in the co-moving frame we move with the fluid. Ideally, RT would be formulated in the lab frame to remain consistent with the MHD equations (Eqs. 1–5), where conservation laws are easiest to implement, especially in Eulerian schemes. However, RT involves frequency-dependent opacities, which in the lab frame require Doppler corrections due to gas-photon relative motion. In the co-moving frame, opacities can be evaluated directly.

To balance these advantages, most RHD methods use a mixed-frame formulation: radiation quantities (energy density, flux, pressure tensor) are defined in the lab frame, while opacities are computed in the co-moving frame. This simplifies microphysics but introduces additional source terms that expand in orders of v/c (Mihalas and Mihalas 1984; Mihalas and Auer 2001). In practice, it is sufficient to retain the leading terms in v/c, with the required order depending on whether the system is in the streaming, static, or dynamic diffusion limit. The most general formulation, valid across all regimes, includes terms up to  $\mathcal{O}(v^2/c^2)$  (see tab. 1 in Krumholz et al. 2007b), which is adequate for the non-relativistic flows relevant to the ISM and star formation, where  $v/c \lesssim 10^{-3}$ .

## 7.2 Basic equations of radiation transfer

## 7.2.1 Time-dependent radiation transfer

The basic RT equation describes how the radiation intensity changes along a ray. Consider an element of material with length ds, then the infinitesimal difference between the radiation energy that enters at  $(\mathbf{x}, t)$  and emerges at a different point in space and time,  $(\mathbf{x} + \Delta \mathbf{x}, t + \Delta t)$ ,

$$[I_{\nu}(\mathbf{x} + \Delta \mathbf{x}, t + \Delta t, \mathbf{n}) - I_{\nu}(\mathbf{x}, t, \mathbf{n})] dA d\Omega d\nu dt, \tag{40}$$

is produced by emission and absorption along the ray. Here  $I_{\nu}$  (erg cm<sup>-2</sup> sr<sup>-1</sup> Hz<sup>-1</sup> s<sup>-1</sup>) is the radiation intensity at frequency  $\nu$ , dA is the surface area perpendicular to the direction of propagation  $\mathbf{n}$ ,  $d\Omega$  is the solid angle, and dt is the time. Without scattering<sup>19</sup> this can be written as the difference between emission and absorption along ds,

$$[j_{\nu}(\mathbf{x}, t, \mathbf{n}) - \rho \kappa_{\nu}(\mathbf{x}, t, \mathbf{n}) I_{\nu}(\mathbf{x}, t, \mathbf{n})] ds dA d\Omega d\nu dt, \tag{41}$$

where  $j_{\nu}$  (erg cm<sup>-3</sup> sr<sup>-1</sup> Hz<sup>-1</sup> s<sup>-1</sup>) and  $\rho \kappa_{\nu}$  (cm<sup>-1</sup>) are the emissivity and extinction coefficient, respectively, with the opacity  $\kappa_{\nu}$  (cm<sup>2</sup> g<sup>-1</sup>). Substituting dt = ds/c with the speed of light c, and omitting the explicit dependencies ( $\mathbf{x}, t, \mathbf{n}$ ) for compactness, this expression becomes a PDE in the intensity,

$$\left(\frac{1}{c}\frac{\partial}{\partial t} + \mathbf{n} \cdot \nabla\right) I_{\nu} = j_{\nu} - \rho \kappa_{\nu} I_{\nu}. \tag{42}$$

This equation depends on seven variables: time, three spatial dimensions, two angular directions (via n), and photon frequency. Time-dependent RHD calculations must solve the RT equation at every time step and then couple the result to the MHD equations (Eqs. 1–5). Altogether this defines a complex, coupled set of PDEs that is extremely challenging to solve.

#### 7.2.2 Time-independent radiation transfer

A common simplification is the *time-independent* RT equation, obtained by neglecting the  $\partial/\partial t$  term in Eq. (42), valid when the radiation field is in steady state compared to the hydrodynamic evolution. In this case, the equation reduces to

$$\mathbf{n} \cdot \nabla I_{\nu} = j_{\nu} - \rho \kappa_{\nu} I_{\nu}. \tag{43}$$

Along a ray parametrized by path length s, this becomes an ordinary differential equation,

$$\frac{dI_{\nu}}{ds} = j_{\nu} - \rho \kappa_{\nu} I_{\nu} = \rho \kappa_{\nu} (S_{\nu} - I_{\nu}), \tag{44}$$

with the source function  $S_{\nu} = j_{\nu}/(\rho \kappa_{\nu})$ . This has the well-known exponential solution

$$I_{\nu}(s) = I_{\nu}(0) e^{-\tau_{\nu}(s)} + \int_{0}^{s} j_{\nu}(s') e^{-[\tau_{\nu}(s) - \tau_{\nu}(s')]} ds'$$

$$= I_{\nu}(0) e^{-\tau_{\nu}(s)} + \int_{0}^{s} \rho(s') \kappa_{\nu}(s') S_{\nu}(s') e^{-[\tau_{\nu}(s) - \tau_{\nu}(s')]} ds'$$

$$= I_{\nu}(0) e^{-\tau_{\nu}(s)} + \int_{0}^{\tau_{\nu}(s)} S_{\nu}(\tau'_{\nu}) e^{-[\tau_{\nu}(s) - \tau'_{\nu}]} d\tau'_{\nu},$$
(45)

<sup>&</sup>lt;sup>19</sup>Neglecting direct scattering is often a reasonable approximation in star-formation studies, where true absorption usually dominates, or scattering can be folded into an 'effective opacity'.

where  $\tau_{\nu}(s) = \int_0^s \rho(s')\kappa_{\nu}(s') ds'$  is the optical depth along the path. The first term describes attenuation of the incident radiation, while the second term accounts for local emission along the ray.

## 7.3 Ray-based methods

Ray-based methods solve the RT equation (Eq. 42) along characteristics (rays). Their accuracy and efficiency depend on ray length and angular sampling. Most star-formation applications use either long characteristics or hybrid long—short characteristics. Long characteristics trace rays with multiple crossings of resolution elements (grid cells or SPH particles), while short characteristics solve the RT equation by interpolating between neighboring cells (Abel and Wandelt 2002; Davis et al. 2012). The former is more accurate but harder to parallelize, since rays cross multiple processor domains, requiring intensive communication. Short characteristics are easier to parallelize but are also more diffusive. Hybrid schemes combine both: long characteristics near sources and short characteristics for long-range propagation, as in the FLASH implementation (Rijkhorst et al. 2006; Buntemeyer et al. 2016).

Relative to moment methods (Sect. 7.4), ray-based approaches excel at modeling radiation from point sources but perform poorly in the diffusion limit unless many rays are used. Hybrid ray-moment methods address this by splitting the flux into a direct stellar component and a diffuse (reprocessed) component,

$$\mathbf{F}_{\rm r} = \mathbf{F}_{\star} + \mathbf{F}_{\rm reprocessed},\tag{46}$$

with  $\mathbf{F}_{\star}$  computed by ray tracing and  $\mathbf{F}_{\text{reprocessed}}$  solved via a moment method (e.g., Murray et al. 1994).

For  $\mathbf{F}_{\star}(r)$ , as a function of distance r from the star, neglecting time dependence, scattering, and in-situ emission, the time-independent RT equation (Eq. 45) with  $j_{\nu}=0$  yields

$$I(r) = I_0 e^{-\tau(r)}, (47)$$

where the optical depth is

$$\tau(r) = \int_{R_{\star}}^{r} \kappa_{\rm P}(T_{\star}) \, \rho(r') \, dr', \tag{48}$$

with  $R_{\star}$  the stellar radius and  $\kappa_{\rm P}(T_{\star})$  the Planck-mean opacity (Eq. 38) at  $T_{\star}$ . The stellar flux then follows

$$\mathbf{F}_{\star}(r) = F_{\star}(R_{\star}) \left(\frac{R_{\star}}{r}\right)^{2} e^{-\tau(r)} \frac{\mathbf{r}}{r}, \tag{49}$$

where  $F_{\star}(R_{\star}) = L_{\star}/(4\pi R_{\star}^2) = \sigma_{\rm SB} T_{\star}^4$  is the stellar surface flux for a star of luminosity  $L_{\star}$ , and  $\sigma_{\rm SB}$  is the Stefan–Boltzmann constant.

The accuracy of ray tracing depends on angular sampling. Long characteristics oversample near the source but undersample at large radii. HEALPix (Górski et al. 2005) addresses this by dividing the sphere into equal-area elements and enabling

adaptive ray splitting, maintaining uniform angular resolution and efficient parallelization in AMR and SPH codes (Abel and Wandelt 2002; Wise and Abel 2011; Buntemeyer et al. 2016; Rosen et al. 2017; Kim et al. 2017).

Hybrid methods following the approach in Eq. (46) are implemented in FLASH (Rijkhorst et al. 2006; Buntemeyer et al. 2016; Peters et al. 2010; Menon et al. 2022), ORION2 (Rosen et al. 2017), and PLUTO (Kuiper et al. 2010; Klassen et al. 2014). These methods are well suited for massive star formation, where they capture both direct stellar radiation pressure and dust-reprocessed flux. They regulate accretion, drive instabilities and outflows, and influence fragmentation (Rosen et al. 2016, 2019; Menon et al. 2023), potentially setting the final stellar mass (Kuiper and Hosokawa 2018). Adaptive UV ray-tracing methods have also been applied to photoionization (Kim et al. 2017, 2019, 2021; Menon et al. 2023).

#### 7.4 Moment methods

One of the most widely adopted classes of RHD approaches are moment methods, which reduce the dimensionality of the RT problem by integrating over angles. This procedure is analogous to deriving the MHD equations from the Boltzmann equation via the Chapman–Enskog method. The accuracy of the resulting equations depends critically on the adopted closure relation. In the following, we derive the moments of the RT equation and then discuss the three most common closures: the Eddington approximation (also called *flux-limited diffusion*, FLD), the Moment-1 (M1) closure, and the variable Eddington tensor (VET) closure.

By averaging over all angles, low-order closures such as FLD perform well in the optically-thick, diffusive limit. Higher-order closures like M1 and VET also capture the transition between optically-thick and optically-thin gas. While all moment methods average over angles to obtain a mean intensity, M1 and VET additionally retain information about the radiation flux, thus preserving directional information. As a class, moment methods are computationally efficient, with cost scaling as  $N \log N$ , where N is the number of resolution elements. Implementation can be challenging, however, particularly for VET, which requires a preliminary ray-tracing step (cf. Sect. 7.3) to compute the Eddington tensor before solving the RHD moment equations. The latter is typically done with solver libraries such as the Portable, Extensible Toolkit for Scientific Computation (PETSc; Balay et al. 1997), the High Performance Preconditioners package (Hypre; Falgout and Yang 2002), or the Adaptive Mesh Refinement Exascale library (AMReX; Zhang et al. 2019).

#### 7.4.1 Moments of the radiation transport equation

Equation (42) describes the directional propagation of radiation at frequency  $\nu$ , subject to emission and absorption. Solving it in full is prohibitively complex, since every point in space and time emits and absorbs at multiple frequencies and angles. To simplify, we adopt the 'gray' approximation, integrating over all frequencies (an assumption that can later be relaxed with multi-frequency bins). We then take angular

averages of the radiation intensity, defining the moments of the radiation field:

Radiation energy density: 
$$E_{\rm r} = \int E_{\rm r,\nu} d\nu = \int \left(\frac{1}{c} \int I_{\nu} d\Omega\right) d\nu,$$
 (50)

Radiation flux: 
$$\mathbf{F}_{r} = \int \mathbf{F}_{r,\nu} d\nu = \int \left( \int I_{\nu} \mathbf{n} d\Omega \right) d\nu,$$
 (51)

Radiation pressure: 
$$\mathbb{P}_{\mathbf{r}} = \int \mathbb{P}_{\mathbf{r},\nu} d\nu = \int \left(\frac{1}{c} \int I_{\nu} \mathbf{n} \mathbf{n} d\Omega\right) d\nu.$$
 (52)

Using these definitions, we can derive more tractable equations for the radiation field by taking successive angular moments of Eq. (42), i.e.,  $\iint (\cdots) \mathbf{n}^m d\Omega d\nu$  for  $m = 0, 1, \ldots$  The m = 0 and m = 1 moments describe the evolution of radiation energy and flux, respectively. As an example, integrating Eq. (42) gives

$$\iint \left(\frac{1}{c}\frac{\partial}{\partial t} + \mathbf{n} \cdot \nabla\right) I_{\nu} d\Omega d\nu = \iint \left(j_{\nu} - \rho \kappa_{\nu} I_{\nu}\right) d\Omega d\nu$$

$$\implies \frac{\partial E_{\mathbf{r}}}{\partial t} + \nabla \cdot \mathbf{F}_{\mathbf{r}} = \iint \left(j_{\nu} - \rho \kappa_{\nu} I_{\nu}\right) d\Omega d\nu. \tag{53}$$

This relation is analogous to the hydrodynamic continuity equation: the local change in  $E_{\rm r}$  is set by the net flux divergence, plus emission and absorption terms on the RHS. If the gas were at rest, the RHS could be written as

$$\iint (j_{\nu} - \rho \kappa_{\nu} I_{\nu}) d\Omega d\nu = J - \rho \kappa_{\rm E} c E_{\rm r}, \tag{54}$$

where  $J = \rho \kappa_{\rm P} 4\sigma_{\rm SB} T^4$  is the emission rate in LTE (via Kirchhoff's law), with  $\kappa_{\rm P}$  the Planck mean opacity (Eq. 38). The absorption term involves the energy mean opacity,

$$\kappa_{\rm E} = \frac{\int_0^\infty \kappa_\nu E_{\rm r,\nu} \, d\nu}{\int_0^\infty E_{\rm r,\nu} \, d\nu}.\tag{55}$$

Similarly, the m=1 moment introduces the flux mean opacity,

$$\kappa_{\rm F} = \frac{\int_0^\infty \kappa_{\nu} |\mathbf{F}_{\rm r,\nu}| \, d\nu}{\int_0^\infty |\mathbf{F}_{\rm r,\nu}| \, d\nu}.$$
 (56)

In reality, the gas moves. The LHS operators of Eq. (53) are exact in the lab frame, but evaluating the RHS is complicated because photons undergo Doppler shifts, aberration, and advection relative to the comoving frame where opacities are most naturally defined. Thus, absorption and emission couple differently in lab vs. comoving frames. To treat this consistently, most RHD approaches adopt a mixed-frame formalism, valid to leading order in v/c (cf. Sect. 7.1.2), which introduces additional terms involving  $E_{\rm r}$ ,  $\mathbf{F}_{\rm r}$ , and  $\mathbb{P}_{\rm r}$  (Mihalas and Auer 2001; Krumholz et al. 2007b; Menon et al. 2022).

A fundamental issue is that the hierarchy of moment equations never closes: the mth moment depends on the (m+1)th. For example, Eq. (53) for  $E_r$  depends on  $\mathbf{F}_r$ , while  $\mathbf{F}_{r}$  depends on  $\mathbb{P}_{r}$ , and so forth. Closure is obtained by assuming a relation of the form

$$\mathbb{P}_{\mathbf{r}} = \mathbb{T} E_{\mathbf{r}},\tag{57}$$

where the Eddington tensor  $\mathbb{T}$  encodes the angular structure of the radiation field. The choice of  $\mathbb T$  determines the accuracy of the method. Common closures include:

- 1. Diffusion limit (flux-limited diffusion; FLD):  $\mathbb{T} = \mathbb{I}/3$ .
- 2. Free-streaming limit:  $\mathbb{T} = \mathbf{n}\mathbf{n}$ , aligning  $\mathbb{P}_{r}$  with  $\mathbf{F}_{r}$ .
- 3. Moment-1 (M1) closure:  $\mathbb{T}$  as a function of the reduced flux  $|\mathbf{F}_r|/(cE_r)$ .
- 4. Variable Eddington tensor (VET): T computed directly from Eqs. (50) and (52) using  $I_{\nu}$  from the time-independent RT solution (Eq. 45), typically via ray tracing.

We will discuss and compare the FLD, M1, and VET closures in detail below.

#### 7.4.2 Complete set of RHD moment equations

Combining the above, the mixed-frame formulation of the RHD moment equations is (Mihalas and Auer 2001; Menon et al. 2022)

$$\frac{\partial(\rho \mathbf{v})}{\partial t} = -\nabla \cdot (\rho \mathbf{v} \mathbf{v}) - \nabla p_{\text{th}} + \mathbf{G},$$

$$\frac{\partial(\rho e)}{\partial t} = -\nabla \cdot [(\rho e + p_{\text{th}}) \mathbf{v}] + cG^{0},$$
(58)

$$\frac{\partial(\rho e)}{\partial t} = -\nabla \cdot [(\rho e + p_{\rm th})\mathbf{v}] + cG^0, \tag{59}$$

$$\frac{\partial E_{\rm r}}{\partial t} = -\nabla \cdot \mathbf{F}_{\rm r} - cG^0,\tag{60}$$

$$\frac{\partial \mathbf{F}_{\mathbf{r}}}{\partial t} = -\nabla \cdot (c^2 E_{\mathbf{r}} \mathbb{T}) - c^2 \mathbf{G},\tag{61}$$

with  $p_{\rm th}$  and e as defined in Sect. 2.1. The source terms  $G^0$  and  ${\bf G}$  represent absorption and emission of radiation energy and momentum. They appear with opposite sign in the MHD momentum and energy equations, ensuring self-consistent gas-radiation

To leading order in v/c, and assuming a direction-independent flux spectrum (Krumholz et al. 2007b), these terms are (Mihalas and Auer 2001; Menon et al. 2022)

$$G^{0} = \rho \kappa_{E} E_{r} - \frac{1}{c} \rho \kappa_{F} 4 \sigma_{SB} T^{4} + \rho \left( \kappa_{F} - 2 \kappa_{E} \right) \frac{\mathbf{F}_{r}}{c} \cdot \frac{\mathbf{v}}{c} + \rho \left( \kappa_{E} - \kappa_{F} \right) E_{r} \left( \frac{|\mathbf{v}|^{2}}{c^{2}} + \frac{\mathbf{v} \mathbf{v}}{c^{2}} : \mathbb{T} \right),$$

$$\mathbf{G} = \rho \kappa_{F} \left[ \frac{\mathbf{F}_{r}}{c} - E_{r} (\mathbb{I} + \mathbb{T}) \frac{\mathbf{v}}{c} \right].$$
(62)

The mean opacities  $\kappa_{\rm P}$ ,  $\kappa_{\rm R}$ ,  $\kappa_{\rm E}$ , and  $\kappa_{\rm F}$  are defined in Eqs. (38), (39), (55), and (56), and are evaluated in the co-moving frame. This choice makes them straightforward to compute, while the remaining quantities are handled in the lab frame—facilitating mixed-frame implementation.

In general, solving Eqs. (60) and (61) requires implicit evaluation of  $\kappa_{\rm E}$  and  $\kappa_{\rm F}$  through frequency integration over  $E_{\rm r}$  and  ${\bf F}_{\rm r}$ . In practice, useful approximations exist:  $\kappa_{\rm E} \approx \kappa_{\rm P}$  holds near LTE, while for optically-thick gas (diffusion limit)  $\kappa_{\rm F} \approx \kappa_{\rm R}$ . These substitutions are widely used, though they may remain reasonable even before reaching the strict diffusion limit. This system of equations is closed once a choice for  ${\mathbb T}$  is specified, with the FLD, M1, and VET closures discussed in the following subsections.

## 7.4.3 Flux-limited diffusion (FLD)

FLD is the simplest moment closure, obtained by assuming an isotropic radiation field in the laboratory frame, so that the Eddington tensor is

$$\mathbb{T} = \frac{1}{3} \, \mathbb{I}. \tag{63}$$

In this limit, one eliminates the radiation momentum equation by prescribing a relation for the flux in terms of the radiation energy density (a diffusion law), and evolves only the m=0 moment (Eq. 60) coupled to the gas via the source terms in Sect. 7.4.2. This approximation is often accurate in optically-thick regions where gas and radiation are strongly coupled (e.g., dense star-forming gas; Offner et al. 2012), but it degrades in optically-thin environments (e.g., cloud outskirts, jet-cleared polar cavities), where diffusion is a poor description.

To prevent superluminal propagation of radiation fronts in optically-thin regions, FLD introduces a *flux limiter* that transitions smoothly between diffusion and free-streaming. The standard (Levermore and Pomraning 1981) form is

$$\mathbf{F}_{\mathbf{r}} = -\frac{\zeta c}{\rho \kappa_{\mathbf{R}}} \nabla E_{\mathbf{r}}, \qquad \zeta = \frac{1}{\xi} \left( \coth \xi - \frac{1}{\xi} \right), \qquad \xi = \frac{|\nabla E_{\mathbf{r}}|}{\rho \kappa_{\mathbf{R}} E_{\mathbf{r}}}, \tag{64}$$

where  $\kappa_{\rm R}$  is the Rosseland mean opacity (Eq. 39). In the diffusion limit ( $\xi \to 0$ ),  $\zeta \to 1/3$  and

$$\mathbf{F}_{\mathrm{r}} \to -\frac{c}{3\rho\kappa_{\mathrm{R}}} \nabla E_{\mathrm{r}},$$
 (65)

while in the streaming limit  $(\xi \to \infty)$ ,  $\zeta \to 1/\xi$  and  $|\mathbf{F}_{\rm r}| \to c E_{\rm r}$  with  $\mathbf{F}_{\rm r}$  aligned antiparallel to  $\nabla E_{\rm r}$ .

Thus, the FLD system is obtained by inserting Eq. (64) into the general RHD moment equations from Sect. 7.4.2. This includes radiation pressure through  $\mathbb{P}_{\rm r} = (E_{\rm r}/3) \mathbb{I}$  (e.g., relevant for massive star formation), through the mixed-frame source terms  $G^0$  and G with the FLD flux substituted (explicit forms are summarized in Krumholz et al. 2007b). The incorporation of radiation pressure allows the treatment of massive star formation, where radiation regulate gas accretion (Rosen et al. 2020). Simulations of massive star formation with non-axisymmetric geometries, however,

find that radiation pressure is not sufficient to halt accretion onto the star (Krumholz et al. 2009; Commerçon et al. 2011).

Gray and multi-group FLD schemes are widely used in star-formation simulations (cf. Table 1). Multi-group extensions, i.e., solving the FLD system for several frequency bins, improve temperature accuracy across a wide range of optical depths (Shestakov and Offner 2008; Kuiper and Klessen 2013; González et al. 2015). Nonetheless, FLD has well-known limitations: by construction  $\mathbf{F}_{\rm r} \parallel -\nabla E_{\rm r}$ , so it cannot cast shadows or represent crossing beams, and it can misdirect radiation forces in multi-source configurations (Hayes and Norman 2003; Jiang et al. 2012; Menon et al. 2022). These deficiencies motivate higher-order closures, such as M1 and VET (Sect. 7.4.4 and 7.4.5), which retain angular information.

## 7.4.4 Moment-1 (M1) closure

Some limitations of FLD can be alleviated by retaining partial directional information of the radiation field. The M1 closure assumes rotational symmetry around the radiative flux direction. The Eddington tensor is then a linear combination of  $\mathbb{I}$  (as in FLD) and the flux direction tensor  $\hat{\mathbf{F}}_r\hat{\mathbf{F}}_r$ , where  $\hat{\mathbf{F}}_r = \mathbf{F}_r/|\mathbf{F}_r|$  (Levermore 1984; Skinner and Ostriker 2013),

$$\mathbb{T} = \frac{1 - \chi}{2} \mathbb{I} + \frac{3\chi - 1}{2} \hat{\mathbf{F}}_{\mathbf{r}} \hat{\mathbf{F}}_{\mathbf{r}}, \tag{66}$$

with the Eddington factor  $\chi$  chosen to ensure flux limiting (Levermore 1984),

$$\chi(f_r) = \frac{3 + 4f_r^2}{5 + 2\sqrt{4 - 3f_r^2}},\tag{67}$$

where  $f_r = |\mathbf{F}_r|/(cE_r)$  is the reduced flux. This closure smoothly interpolates between the diffusion  $(f_r \to 0 \Longrightarrow \chi \to 1/3)$  and streaming  $(f_r \to 1 \Longrightarrow \chi \to 1)$  limits, avoiding the need for an ad-hoc flux limiter.

The M1 system is thus the general RHD moment equations (Sect. 7.4.2) with  $\mathbb{T}$  given by Eqs. (66) and (67). While M1 outperforms FLD in optically-thin regions and can reproduce shadows from a single source, it fails in multi-source configurations where fluxes can spuriously cancel (Frank et al. 2012; Skinner and Ostriker 2013; Menon et al. 2022). This limitation arises because the M1 Eddington tensor is defined purely locally, depending only on  $\mathbf{F}_r$  and  $E_r$ .

An advantage is that the M1 system is hyperbolic, allowing radiation to be evolved like a fluid with wave speed  $\lesssim c$ . However, explicit timesteps are prohibitively small ( $\Delta t \propto c^{-1}$ ) compared to the CFL timestep of the MHD system. A common remedy is the reduced speed of light approximation ( $c \to \tilde{c} \ll c$  in time-derivative terms only) (Gnedin and Abel 2001; Skinner and Ostriker 2013; Hopkins and Grudić 2019; Mignon-Risse et al. 2020). This is accurate if  $\tilde{c} \gg v_{\rm max}$ , the maximum MHD signal speed (Rosdahl et al. 2013), with tests showing proper ionization front propagation for  $\tilde{c} \gtrsim 30\,{\rm km\,s^{-1}}$  (Geen et al. 2015a; Grudić et al. 2021). Too small a  $\tilde{c}$ , however,

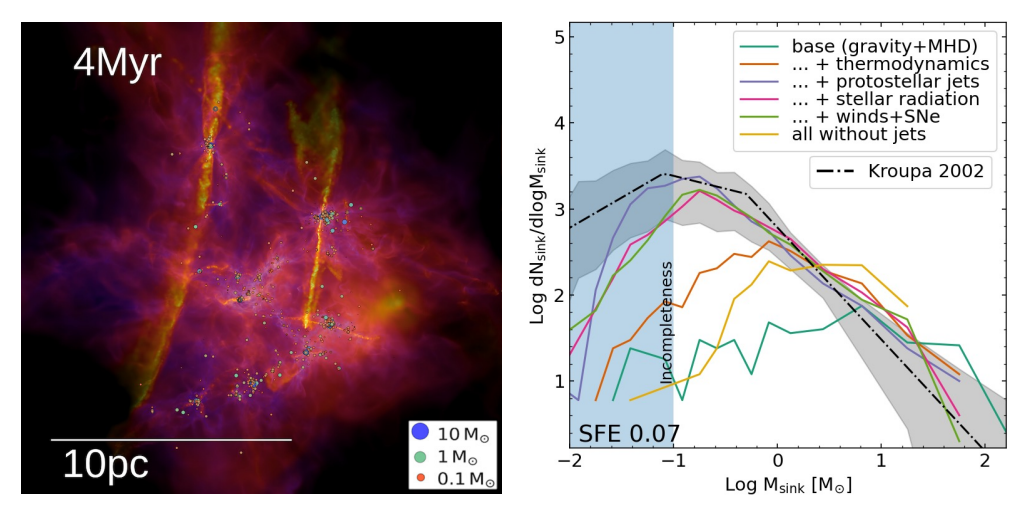


Fig. 9 STARFORGE simulation of a molecular cloud including an M1 multi-bin RHD method with ionization, radiation pressure, and other stellar feedback processes (Guszejnov et al. 2022). Left panel: Color map of the 1D line-of-sight velocity dispersion, increasing from purple (0.1 km s<sup>-1</sup>) to orange (10 km s<sup>-1</sup>). Surface density is indicated by brightness (lighter is denser). Kinematic maps highlight feedback features such as protostellar outflows. Circles mark the locations of sink particles, with size and color denoting stellar mass. Right panel: Stellar initial mass function (IMF) for simulations with different physics included, as indicated in the legend. Protostellar jets have the overall biggest effect (cf. Sect. 6.2), with radiation primarily reducing the formation of very low-mass stars (cf. Fig. 8).

underestimates radiation pressure in optically-thick gas, relevant to massive star formation. Additional cost reductions can be achieved via radiation sub-cycling (Skinner and Ostriker 2013).

M1 has been implemented in ATHENA (Skinner and Ostriker 2013), AREPO (Kannan et al. 2019), Flash (Menon et al. 2022), Gizmo (Hopkins and Grudić 2019), QUOKKA (Wibking and Krumholz 2022; He et al. 2024b.a), and RAMSES (Aubert and Teyssier 2008; Rosdahl et al. 2013; Rosdahl and Teyssier 2015; Mignon-Risse et al. 2020). Its strictly local closure, similar to FLD, ensures that the M1 method is independent of the number of sources, and that it scales linearly with the number of resolution elements, as it is usually evolved with explicit time integration, making it well-suited for large-scale simulations. Applications to star-cluster formation find ionization and radiation pressure from massive stars significantly regulate efficiencies (Skinner and Ostriker 2015; Raskutti et al. 2016, 2017; Grudić et al. 2021). Multi-group M1 extensions following distinct radiation bands capture frequency-dependent radiation effects such as ionizing feedback more realistically (Aubert and Teyssier 2008; Rosdahl et al. 2013; Rosdahl and Teyssier 2015; Geen et al. 2015b,a, 2016, 2017; Guszejnov et al. 2022; He et al. 2024b,a), with results showing cloud dispersal and reduced star formation efficiencies, and suppression of low-mass star formation through radiation heating (see Fig. 9).

## 7.4.5 Variable Eddington tensor (VET) method

The variable Eddington tensor (VET) method is the most advanced moment-based approach to RHD (see e.g., Hayes and Norman 2003; Davis et al. 2012; Jiang et al. 2012; Menon et al. 2022). Unlike the M1 closure, the Eddington tensor in VET is not determined locally but computed directly from angular quadratures of the frequency-averaged specific intensity  $I_{\rm r}$  via Eqs. (50) and (52). The intensity  $I_{\rm r}$  along path length s follows the time-independent RT equation (cf. Eqs. 44–45) under the gray approximation with the Planck mean opacity  $\kappa_{\rm P}$  (Eq. 38):

$$I_{\rm r}(s) = \int_0^\infty I_{\nu}(s) \, d\nu$$

$$\approx I_{\rm r}(0) e^{-\tau(s)} + \int_0^s \rho(s') \, \kappa_{\rm P}(s') \, S_{\rm r}(s') \, e^{-[\tau(s) - \tau(s')]} \, ds', \tag{68}$$

with

$$\tau(s) = \int_0^s \rho(s') \kappa_{\mathcal{P}}(s') \, ds', \tag{69}$$

and  $S_{\rm r}$  the source function, typically the integrated Planck function for dust emission,  $S_{\rm r}(s) = \sigma_{\rm SB} T^4(s)/\pi$ . This expression neglects scattering and  $\mathcal{O}(v/c)$  terms from the mixed-frame formulation, which are expected to make only minor contributions to  $\mathbb{T}$ .

In practice, Eq. (68) is evaluated by ray tracing (Sect. 7.3) along discrete directions  $\mathbf{n}$ , producing  $I_{\mathbf{r}}(\mathbf{n})$  and thus  $\mathbb{T}$  via Eqs. (50) and (52). In FLASH, this is achieved using the parallel hybrid-characteristics ray tracer of Buntemeyer et al. (2016), with AMR support, and directions discretized via HEALPix (Górski et al. 2005) into 12, 48, 192, 768, etc. equal-area rays. The resulting  $\mathbb{T}$  is then inserted into the coupled RHD system (Eqs. 58–62). Solving this implicit system is done efficiently in parallel using PETSc (Balay et al. 1997), with additional care at coarse-fine AMR boundaries (Menon et al. 2022).

The strength of VET is its accuracy across both optically-thin and optically-thick limits, as well as in the transition regime. It reproduces realistic shadows, radiation fields, and gas temperature distributions. Accuracy depends on the angular resolution (Davis et al. 2012): with HEALPix sampling, biases from grid alignment are minimized by rotating the base orientation between runs. Menon et al. (2022) showed that using 48 rays already yields very good results, with only marginal improvement at 192 rays; see their fig. B1.

#### Extension to multi-frequency VET

In Eq. (62) we approximated  $\kappa_{\rm E} = \kappa_{\rm P}$  and  $\kappa_{\rm F} = \kappa_{\rm R}$ , which ensures consistency with the steady-state equation for  $E_{\rm r}$  (Menon et al. 2022). However, this choice is not simultaneously consistent with the steady-state equation for  ${\bf F}_{\rm r}$ . In fact, no single gray opacity can make both moment equations exact — only frequency-dependent opacities can achieve full consistency.

To improve upon this limitation, Menon et al. (2023) developed a multi-frequency RHD scheme combining the IR dust-radiation approach described above with an ionizing (UV) radiation treatment. The UV component computes the hydrogen ionization

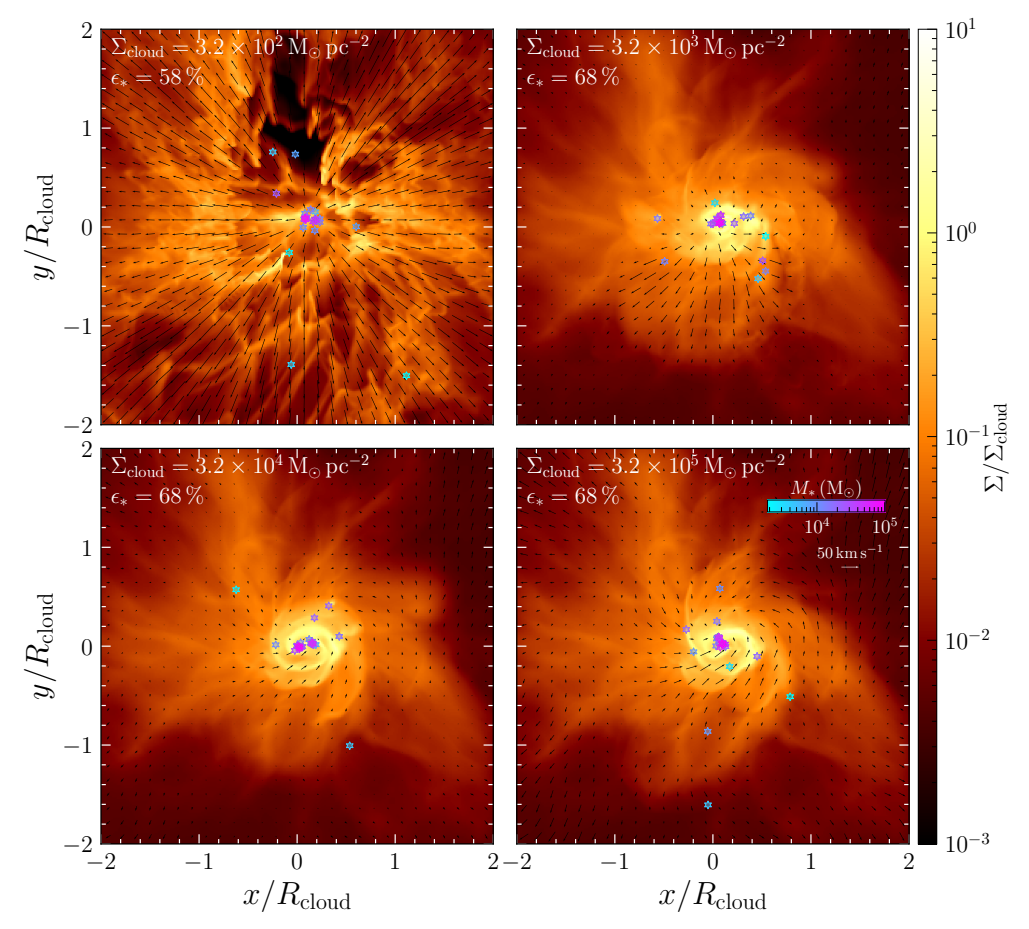


Fig. 10 Massive star cluster formation and feedback using the combined VET IR and UV scheme from Menon et al. (2023). Shown are simulations of clouds with increasing surface density. In Milky Way–like conditions (top left), the UV radiation component drives powerful outflows that disperse the cloud and limit the star formation efficiency  $\epsilon_*$ . In contrast, in extreme, dense environments (bottom right), neither UV nor IR feedback can disperse the cloud, and  $\epsilon_*$  remains high. An animation is available at https://shm-1996.github.io/movies/.

fraction by evaluating the optical depth of ionizing photons along rays. The ionization fraction then updates the opacity and iterates to convergence. A natural next step would be to include Doppler shifts of the ionizing lines, whereas the method of Menon et al. (2023) currently assumes hydrogen ionization in the rest frame.

Figure 10 demonstrates this IR+UV VET approach in simulations of massive star-cluster formation. Four clouds of increasing surface density are compared. In typical Galactic environments, UV feedback disperses clouds via outflows, soon after cluster formation, significantly reducing the star formation efficiency,  $\epsilon_*$ . In very dense, extreme conditions, however, radiative feedback is largely ineffective, and the star formation efficiency remains high.

## 7.5 Monte Carlo radiation transfer

Monte Carlo radiation transfer (MCRT) is analogous to kinetic theory in gas dynamics: instead of explicitly solving the RT equation, MCRT uses a large number of test particles, or 'photon packets', to model the radiation field. These packets sample the photon phase-space distribution, with each packet's behavior—including direction of propagation and the probability of scattering or absorption—determined probabilistically. As in kinetic theory, it is the ensemble behavior rather than individual packets that matters. With a sufficiently large number of packets, the ensemble accurately represents the RT process. For a detailed review of MCRT techniques, see Noebauer and Sim (2019). Here, we summarize the main characteristics of MCRT.

The accuracy of MCRT improves with the number of packets N, but the computational cost also scales proportionally with N. MCRT parallelizes efficiently, since each processor can follow an independent subset of packets with minimal communication (Robitaille 2011). However, the method becomes inefficient in optically-thick regions, where packets undergo many scatterings, requiring numerous advancement steps to sample the radiation field across the domain.

MCRT methods naturally incorporate scattering and accurately follow the angular dependence of the radiation field, but they require a large number of packets to reach accuracies comparable to moment methods (Davis et al. 2012, see Fig. 11 below). Like all Monte Carlo approaches, MCRT suffers from noise that scales as  $N^{-1/2}$ . For this reason, coupling MCRT directly to MHD simulations has long been considered prohibitively expensive, and the method has most often been used as a post-processing tool (e.g., Dullemond and Turolla 2000; Ercolano et al. 2008; Robitaille 2011; Reissl et al. 2016; Haworth et al. 2018; Harries et al. 2019). Recent advances, however, have led to the development of in-situ MCRT-MHD methods that are competitive in speed and accuracy with moment methods. Implementations now exist in a number of hydrodynamics codes used for star-formation modeling, including AREPO (Smith et al. 2020), CMACIONIZE (Vandenbroucke and Wood 2018), FLASH (Tsang and Milosavljević 2015), PHANTOM (Petkova et al. 2021), and TORUS (Harries 2015).

MCRT-MHD provides a powerful tool for problems with complex, high-intensity radiation fields or multiple scattering events. To make such calculations tractable, however, several numerical approximations and acceleration techniques are employed, including continuous absorption, energy deposition, and implicit thermal balance (Lucy 1999; Bjorkman and Wood 2001), photon weighting and luminosity boosting, and local packet merging and splitting (Smith et al. 2020).

#### 7.6 Comparison of RT methods

Several studies have carried out detailed comparisons between the FLD, M1, MC, and VET methods (Davis et al. 2012; Jiang et al. 2012; Menon et al. 2022). Figure 11 provides a direct comparison of all four methods. The top panels, taken from Davis et al. (2012), show a shearing-box simulation of an accretion disk patch with physical properties described in Hirose et al. (2006) (density is highest at the bottom and decreases toward the disk atmosphere at the top). From left to right, the panels compare FLD, MC, VET with 24 rays, and VET with 168 rays. All panels display the

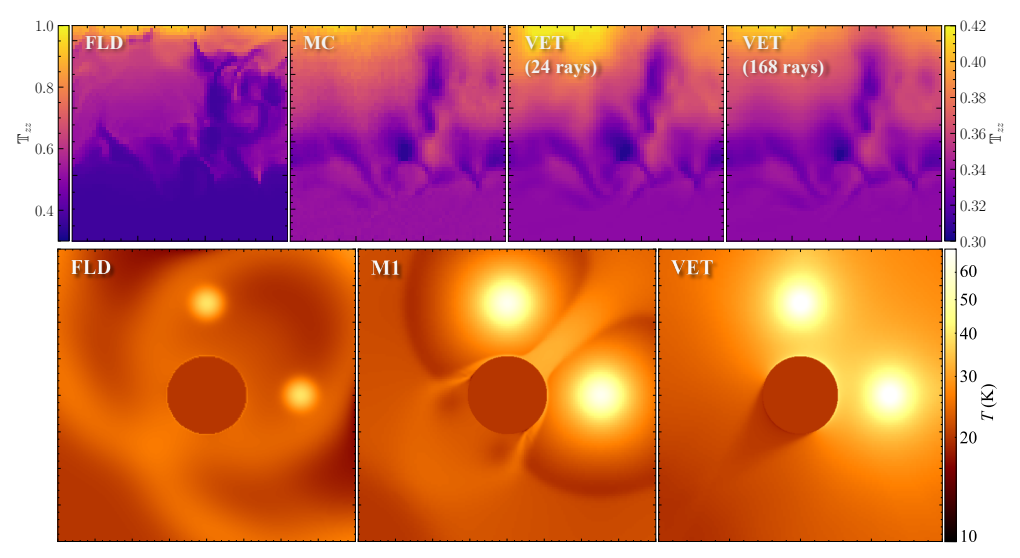


Fig. 11 Comparison of numerical methods for radiation transport (RT). Top panels: Flux-limited diffusion (FLD, left), Monte Carlo (MC, 2nd panel), variable Eddington tensor (VET) with 24 rays (3rd panel), and VET with 168 rays (right) for a shearing-box patch of an accretion disc from Hirose et al. (2006) and Davis et al. (2012). The disk gas density increases from top to bottom in each panel, with shearing flow along the horizontal direction. The panels show the zz-component of the Eddington tensor, where the left color map applies for FLD (for which  $\mathbb{T}_{zz} \to 1$  in optically-thin gas, by construction), and the right color map applies for the MC and VET panels. FLD produces noticeably different structures and magnitudes of  $\mathbb{T}_{zz}$  compared to MC and VET, which are largely consistent. MC shows some small-scale noise but otherwise agrees well with VET using 168 rays. Even with only 24 rays, VET produces similar results, though a larger number of rays is preferable. Bottom panels: FLD (left), Moment-1 (M1, middle), and VET with 192 rays (right) in a shadow test by Menon et al. (2022), where a dense dust cloud is placed at the center of the domain and two radiation sources are located at 12 and 3 o'clock. Panels show the gas temperature after one light-crossing time of the domain. VET is the only method that reproduces the correct temperature distribution, including the correct structure of the shadow behind the cloud. An animation of the bottom panels is available at https://www.mso.anu.edu.au/~chfeder/pubs/vettam/vettam.html.

zz-component of the Eddington tensor  $\mathbb{T}_{zz}$ . FLD yields a markedly different radiation field distribution than MC or VET (note also the different color map range, as  $\mathbb{T}_{zz}$  in FLD approaches unity in the optically-thin limit, by construction). The MC result shows some small-scale noise despite using  $\sim 10^{10}$  photon packets and requiring  $\sim 100\times$  the compute time of VET. The close agreement between MC and VET strongly suggests both methods are accurate. Minor differences are visible between the 24 ray and 168 ray VET runs, with the latter more closely matching MC (aside from the MC noise).

The bottom panels of Fig. 11 compare FLD, M1, and VET in a shadow test, where a dense, high-opacity gas cloud is placed at the center and two radiation sources are positioned at 12 and 3 o'clock in the computational domain (Menon et al. 2022). The surrounding medium is optically thin. In FLD, radiation diffuses around the cloud, producing no shadows. M1 creates directionally dependent solutions with a shadow behind the cloud, opposite the sources. However, the shadow is weaker along the midplane between the two sources and the radiation field shows spurious maxima and

minima around the sources. By contrast, VET yields the correct radiation and gas temperature distribution, including well-defined shadows behind the cloud.

## 7.7 Summary of challenges and future directions

Although RT is fully understood in theory, solving it numerically is extremely challenging due to its high dimensionality (time, 3D space, 2 angles, and frequency; Sect. 7.1 and 7.2). Approximations are therefore essential, including gray (frequency-integrated) treatments or reduced angular sampling in ray tracing (Sect. 7.3). Monte Carlo RT (MCRT; Sect. 7.5) is conceptually simple and highly parallelizable, but requires very large numbers of photon packets to reduce noise. Numerical tricks—such as packet weighting, splitting/merging, continuous absorption, and luminosity boosting—have made MCRT increasingly competitive for live RHD rather than just post-processing.

The most widely used methods remain RHD moment approaches (Sect. 7.4), which are more efficient and easier to parallelize than full ray tracing. A mixed-frame treatment is required to handle frequency-integrated transport and mean opacities (Sect. 7.4.1), leading to the complete set of RHD moment equations (Sect. 7.4.2). Their accuracy hinges on the closure choice for the Eddington tensor: FLD (Sect. 7.4.3) and M1 (Sect. 7.4.4) rely on local quantities, while VET (Sect. 7.4.5) requires a formal RT solution (typically via ray tracing).

Comparisons of FLD, M1, VET, and MCRT (Sect. 7.6) highlight their respective strengths and weaknesses: FLD performs well only in optically-thick regions and cannot capture shadows. M1 reproduces single-source shadows but fails with multiple sources due to spurious flux cancellation. VET and MCRT both produce accurate radiation fields and shadowing; however, MCRT typically requires an order of magnitude more computation to match VET accuracy, though it stands to benefit from advances in GPU acceleration.

Another area of progress is multi-group RT, which distinguishes broad bands such as IR and UV. This enables more realistic treatments of feedback, especially from massive stars. However, incorporating full atomic and molecular line transfer with Doppler shifts (critical for, e.g., Population III star formation) remains too computationally demanding for large-scale applications.

Finally, gas dissipation acts as a local radiation source (Sect. 3.3). Since numerical dissipation is resolution-dependent (Sect. 3.4.1), coupling this heating consistently into the RHD system is non-trivial. Methods that explicitly track the local dissipation rate (Sect. 3.4.2) may provide a promising way forward by linking dissipation-driven heating directly to the radiation source terms.

# 8 Cosmic-ray hydrodynamics (CRHD)

The importance of cosmic rays (CRs), i.e., charged particles traveling at relativistic velocities, to the structure of the ISM and galaxy evolution has long been recognized (Beck 2016). CRs are thought to be primarily produced by diffusive shock acceleration (first-order Fermi acceleration) in supernova remnants (Bell 2004). Within the ISM, the CR pressure is comparable to both thermal and magnetic pressures, making CRs

a key regulator of the star formation rate (Birnboim et al. 2015; Ruszkowski et al. 2017). Bursts of star formation and AGN activity can further accelerate CRs, driving large-scale galactic winds (Booth et al. 2013; Hanasz et al. 2013; Girichidis et al. 2016; Ruszkowski et al. 2017).

Most CRHD studies to date have focused on the impact of CRs at galactic scales. However, their role at smaller scales is equally important. CRs are an important source of ionization in dense molecular gas, thereby altering chemical abundances and reaction rates (e.g., Jørgensen et al. 2020) and controlling magnetic resistivity in molecular clouds, cores, and disks. Despite this, very few numerical studies have explicitly modeled CR propagation within molecular clouds; most star formation simulations either neglect CRs entirely or assume a constant ionization rate.

Recent theoretical and observational studies highlight that CR processes within star-forming regions cannot be ignored. Protostellar jets, accretion shocks, and expanding HII regions can accelerate low-energy ( $\lesssim 100\,\mathrm{GeV}$ ) CRs in situ (Padovani et al. 2020), enhancing the local CR ionization rate with strong consequences for thermodynamics and chemistry (Gaches and Offner 2018; Gaches et al. 2019). Elevated CR ionization increases coupling between gas and magnetic fields, which can either promote compact disk formation or suppress disks altogether (Zhao et al. 2020).

Motivated by this growing recognition, cosmic-ray transport (CRT) modules have now been implemented in several hydrodynamic codes (cf. Table 1). The associated numerical challenges closely parallel those of radiation hydrodynamics (RHD): high characteristic velocities ( $v \sim c$ ), large effective particle numbers, and a broad dynamic range in energies. As a result, many RHD techniques—gray approximations, moment methods (e.g., diffusion), reduced-speed-of-light schemes, and flux limiters—are directly applicable to CRHD. In the following, we review the principal CRHD methods employed in modern star-formation codes. See also the recent comprehensive reviews of CRHD by Ruszkowski and Pfrommer (2023) and Hopkins (2025).

## 8.1 Uncertainties in CR propagation

In contrast to RHD, where the physics of radiation transfer and radiation—matter interactions is relatively well understood, CRHD suffers from significant uncertainties, foremost among them how CRs actually propagate in different physical regimes. These uncertainties can be divided into two main categories: those concerning the physics of CR transport and those concerning CR production mechanisms.

CRs primarily stream along magnetic field lines and change direction through scattering, produced by inhomogeneities in the field (e.g., magnetic mirroring; see Cesarsky and Volk 1978), ambient MHD turbulence (Yan and Lazarian 2004), or Alfvén waves resonantly excited by the CRs themselves (i.e., via the streaming instability; see Skilling 1975). The large uncertainties and complexities in the turbulent structure and dynamics of the magnetized ISM (cf. Fig. 2), combined with the anisotropic nature of CR transport, imply that the degree of scattering and the extent to which CRs diffuse across field lines are uncertain by orders of magnitude. Transport is therefore often parameterized using diffusion coefficients parallel and perpendicular

to the bulk magnetic field, typically treated as free parameters constrained empirically by observations (e.g., Owen et al. 2021).

As they propagate, CRs continuously lose energy through both collisional and non-collisional interactions with the thermal ISM gas. These energy losses are parameterized by a loss function that depends on the ionization state, density, magnetic field strength, and gas/dust composition. However, due to uncertain interaction cross sections and microphysics, even the dominant energy-loss mechanism in some regimes remains debated (e.g., Lazarian and Xu 2022; Gaches et al. 2024; Hopkins 2025).

While there is well-developed theory for the acceleration of CRs at supernova shocks and their energetics, which is supported by observations (Caprioli 2015), the details depend on the local conditions (Hu et al. 2022; Xu and Lazarian 2022). Meanwhile, the acceleration efficiency and resulting CR spectra from other sources have even larger uncertainties. Shock properties (e.g., magnetization, Mach number, and temperature) are poorly constrained in protostellar accretion, HII-region, and jet shocks, and these mechanisms appear to produce CR fluxes far lower than those from SNe (Krumholz et al. 2023). Consequently, the limited observational constraints available for CR fluxes within molecular clouds—such as non-thermal synchrotron emission, gamma-ray emission, and chemical abundances—remain indirect (e.g., Rodríguez-Kamenetzky et al. 2017; Cabedo et al. 2023; Pineda et al. 2024; Pandey et al. 2025). Additional sources of CRs, such as re-acceleration by ISM turbulence (second-order Fermi acceleration) or turbulent reconnection within molecular clouds, may also be important, but are highly uncertain (Drury and Strong 2017; Gaches et al. 2021).

Thus, while the numerical methods for CRHD described below are technically stable and robust, it is important to bear in mind that the fundamental uncertainties in CR transport physics may outweigh the approximations inherent in any given methodology.

#### 8.2 Moment methods for CRHD

Ideally, the transport of CRs would be modeled directly by solving for the CR phase space distribution, e.g., the Fokker-Planck equation derived by applying linear approximations (Skilling 1975; Schlickeiser 1989):

$$\frac{\partial f}{\partial t} = -\mathbf{v} \cdot \nabla f + \nabla \cdot (\mathbb{D}_{xx} \nabla f) + \frac{1}{3} (\nabla \cdot \mathbf{v}) p \frac{\partial f}{\partial p} + \frac{1}{p^2} \frac{\partial}{\partial p} \left[ p^2 \left( b_{\text{loss}} f + D_{pp} \frac{\partial f}{\partial p} \right) \right] + j, \quad (70)$$

where  $f = f(\mathbf{x}, \mathbf{p}, t)$  is the isotropic part of the phase-space CR distribution function, assuming efficient pitch-angle scattering, and  $\mathbb{D}_{xx}$  and  $D_{pp}$  are the spatial diffusion tensor and the momentum diffusion coefficient, respectively. CR momentum losses are described by  $b_{\text{loss}}(\mathbf{x}, \mathbf{p}, t) = dp/dt < 0$ , and  $j = j(\mathbf{x}, \mathbf{p}, t)$  is a CR source term. The first term on the RHS in Eq. (70) represents CR advection with the gas flow ( $\mathbf{v}$ ), while the second term describes CR spatial diffusion. The third term models adiabatic behavior associated with gas expansion and compression. The fourth term describes both energy losses and second-order Fermi acceleration, i.e., re-acceleration due to small-scale magnetic turbulence. The last term, j, represents CRs accelerated due to

first-order Fermi acceleration, i.e., acceleration produced by SNe and/or other shock processes. Cosmic-ray streaming adds an additional transport channel, in which CRs drift along magnetic field lines at approximately the Alfvén speed, which is effectively added to the fluid speed in the Fokker–Planck equation.

Solving the Fokker–Planck equation directly is the approach taken by dedicated CRT solvers such as GALPROP (Strong and Moskalenko 1998), PICARD (Kissmann 2014), DRAGON2 (Evoli et al. 2017), CREST (Winner et al. 2019), and CRIPTIC (Krumholz et al. 2022). However, achieving sufficient accuracy requires resolving a large number of CR momentum bins, which becomes computationally prohibitive in full CRHD contexts (e.g., Winner et al. 2019). Consequently, CRHD implementations in general-purpose hydrodynamic codes adopt a range of approximations, often analogous to those used in RHD (e.g., gray approximations, diffusion models and flux limiters).

CRHD frameworks have been implemented in several AMR and mesh-free codes, including AREPO (Thomas et al. 2021), ATHENA (Zhao et al. 2025), ENZO (Salem and Bryan 2014), FLASH (Girichidis et al. 2014, 2020), GIZMO (Hopkins et al. 2021a), PLUTO (Mignone et al. 2018), and RAMSES (Dubois and Commerçon 2016). Owing to its similarity with RHD, approximate CRT is relatively straightforward to incorporate into codes that already support RHD solvers. Despite its reduced complexity, this treatment can effectively model CR-driven galactic winds, CR pressure support in the ISM, and the role of CRs in SN blast-wave energetics (Salem and Bryan 2014; Dubois and Commerçon 2016; Girichidis et al. 2016). It also enables parameter studies of the highly uncertain diffusion coefficients. For example, Commerçon et al. (2019) identified a critical value of D, below which CRs become effectively 'trapped', producing CR pressure gradients that suppress thermal instability (see Fig. 12a).

#### 8.2.1 One-moment methods

The simplest treatment of CRT assumes that CRs are a single fluid, distinct from the gas, that behaves diffusively, i.e., the CRs scatter and diffuse due to unresolved small-scale turbulence. The most basic implementation assumes frequent CR scattering isotropizes the pitch-angle distribution, leading to an effectively constant diffusion coefficient (Zweibel 2013). In a slightly more nuanced approach transport is parameterized by a (usually constant) diffusion coefficient with components parallel and perpendicular to the magnetic-field direction to allow for anisotropic scattering. This is effectively a single-moment approach, similar to that adopted to treat gray FLD RT (cf. Sect. 7.4.3). In this limit, the CR energy equation is

$$\frac{\partial E_{\text{CR}}}{\partial t} = -\nabla \cdot (E_{\text{CR}} \mathbf{v}) - p_{\text{CR}} (\nabla \cdot \mathbf{v}) + \nabla \cdot (\mathbb{D} \nabla E_{\text{CR}}) + S_{\text{CR}}, \tag{71}$$

where  $E_{\rm CR}$  is the CR energy density,  $p_{\rm CR} = (\gamma_{\rm CR} - 1)E_{\rm CR}$  is the CR pressure with  $\gamma_{\rm CR} = 4/3$  for a relativistic gas,  $\mathbb D$  is the CR diffusion tensor, and  $S_{\rm CR}$  represents CR sources (for a derivation, see Schlickeiser and Lerche 1985). The first two terms on the RHS represent advection and adiabatic compression/expansion. The third and fourth terms describe diffusion and sources of CRs, respectively. CRs are coupled to

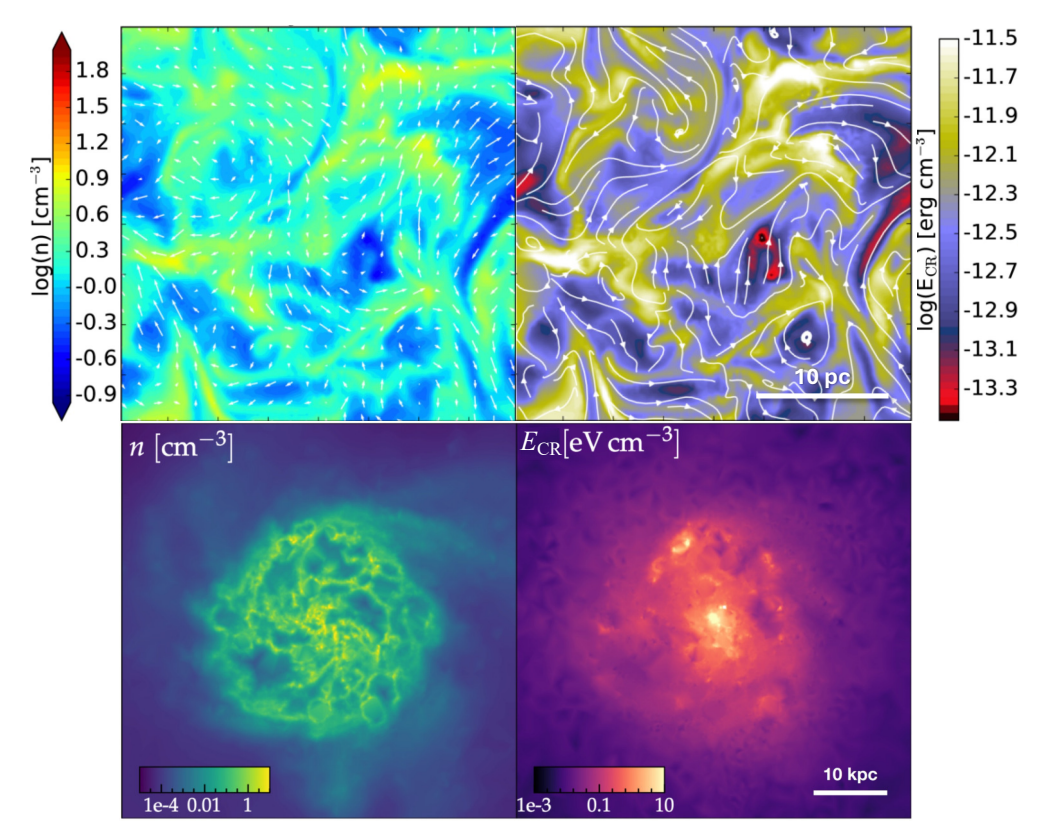


Fig. 12 Top panels: Gas number density (left) and CR energy density (right) in a simulation of magnetized, turbulent ISM gas using a single-moment CRHD scheme (Commerçon et al. 2019). White arrows denote the velocity field, while streamlines show magnetic field lines. With a parallel diffusion coefficient  $D=10^{22}, {\rm cm}^2, {\rm s}^{-1}$ , well within the CR-trapping regime, strong CR energy inhomogeneities develop. Bottom panels: Gas number density (left) and CR energy density (right) in a galactic simulation using a two-moment CRHD scheme (Hopkins et al. 2021b). Here, the diffusion coefficient scales with the damping rate and the streaming velocity is tied to the Alfvén–ion speed. This model reproduces key observables, including the scattering-rate-weighted effective diffusivity, gamma-ray luminosity, and mean CR energy density of a Milky Way–like galaxy.

the MHD system of equations (Sect. 2.1) by adding the diffusion term  $\nabla \cdot (\mathbb{D}\nabla E_{\text{CR}})$  to gas energy equation (Eq. 3) to account for thermal energy injected by CR diffusion. Likewise, the total gas energy density and pressure are updated to include the CR contributions, i.e.,  $\rho e \to \rho e + E_{\text{CR}}$ , and  $p \to p + p_{\text{CR}}$ .

## 8.2.2 Two-moment methods

The diffusion approximation for CRT neglects several key processes: the generation of Alfvén waves by CR streaming, damping of waves through ion–neutral collisions, and nonlinear Landau damping driven by anisotropic particle distributions (see also Rincon et al. 2016; St-Onge and Kunz 2018; Achikanath Chirakkara et al. 2024; Chirakkara et al. 2024). These processes are essential for accurately modeling CR

transport in the multi-phase ISM (Seta and Federrath 2022) and within molecular clouds. Moreover, the diffusion approach is effectively 'gray', since  $E_{\rm CR}$  represents the spectrum-integrated CR energy density, providing no information on the spectral evolution or energy-dependent CR behavior.

A more sophisticated treatment is the two-moment (or flux-evolving) approach, which explicitly evolves the CR flux equation (Zweibel 2017; Jiang and Oh 2018; Thomas and Pfrommer 2019; Chan et al. 2019; Ruszkowski and Pfrommer 2023). This method enables a more accurate treatment of CR streaming. Figure 12b illustrates a two-moment CRHD simulation of a Milky Way-like galaxy, showing that this framework can reproduce several expected CR observables.

Despite methodological parallels to RHD, important differences arise. On galactic scales, one- and two-moment CRT approaches produce very similar bulk outcomes, such as star formation rates and gamma-ray luminosities (Chan et al. 2019). Thomas and Pfrommer (2022) demonstrate that, unlike RHD, the CR behavior is relatively insensitive to the choice of closure. This insensitivity stems from the fact that CR propagation is dominated by pitch-angle scattering, which tends to isotropize the distribution and ensures diffusion dominates over directional effects such as shadowing (cf. Fig.11).

For star-cluster formation, simulations that include all major physics and feedback processes along with CRT for a typical Galactic CR background recover a standard IMF (Fitz Axen et al. 2024). In these models, ambient CRs do not have a significant effect inside dense clouds due to energy losses induced by the streaming instability (Bustard and Zweibel 2021; Fitz Axen et al. 2024), creating CR pressure gradients between the cloud interior and exterior. This gradient enhances the final star formation efficiency. Furthermore, CRT simulations provide tentative evidence that environments with high CR energy densities—whether from an elevated background or local CR acceleration—can yield more top-heavy IMFs (Fitz Axen et al. 2024, 2025).

## 8.3 Multi-bin spectral formalisms

Several recent approaches explicitly follow the evolution of the CR spectrum, including energy-dependent losses. These methods solve discretized forms of the Fokker–Planck equation for the CR number and energy densities, in close analogy to multi-frequency treatments of the RT equation. The first two moments of the Fokker–Planck equation are defined as

$$n_{\mathrm{CR},i} = \int_{p_{i-1/2}}^{p_{i+1/2}} 4\pi p^2 f(p) \, dp, \tag{72}$$

$$E_{\text{CR},i} = \int_{p_{i-1/2}}^{p_{i+1/2}} 4\pi p^2 f(p) T(p) dp,$$
 (73)

where p is the CR momentum,  $n_{\text{CR},i}$  and  $E_{\text{CR},i}$  are the CR number and energy densities in momentum bin i, and

$$T(p) = \sqrt{p^2 c^2 + m_{\rm p}^2 c^4} - m_{\rm p} c^2 \tag{74}$$

is the CR kinetic energy, with the proton mass  $m_{\rm p}$ .

In practice, these methods often assume a piecewise power-law representation of f(p) within each bin,

$$f(p) = f_{i-1/2} \left(\frac{p}{p_{i-1/2}}\right)^{-q_i}, \tag{75}$$

with two degrees of freedom per bin: the normalization  $f_{i-1/2}$  and the spectral slope  $q_i$ . Continuity of f(p) enforces closure. Using these definitions, the two-moment equations for the CR number density and energy density in each momentum bin i can be defined (for details we refer to Girichidis et al. 2020; Hopkins et al. 2022). Cost savings in multi-bin methods are often achieved by using logarithmically-spaced momentum bins and adopting a reduced-speed-of-light approximation (e.g., Chan et al. 2019; Hopkins et al. 2021b).

Spectral CRT methods allow direct comparison with the observed CR spectrum in the Milky Way and other galaxies (Girichidis et al. 2020; Hopkins et al. 2022). They show that CR spectra and ionization rates can vary substantially across galactic environments. These calculations also indicate that turbulent re-acceleration plays only a minor role, while CRs produced in reverse supernova shocks dominate over other sources of acceleration (Hopkins et al. 2022).

#### 8.4 Monte Carlo CR transport

In lieu of a continuous fluid approach, CRT may also be modeled discretely by random sampling from the CR distribution. This is analogous to the MC approach to RT, where the evolution of the radiation spectrum is modeled by following the interactions between individual photon 'packets' and the gas (see Sect. 7.5). To date, no in situ MC CRT methods have been implemented in star-formation hydrodynamic codes, although this is a promising future avenue due to advantages in scalability and spectral resolution, as well as potential for GPU acceleration.

A few examples of MC CRT have been applied to star-formation problems in post processing, however. For example, Fitz Axen et al. (2021b) developed a threedimensional time-independent MC CRT method that follows the propagation of CR protons and electrons through a grid of magnetic-field strengths and densities. The code solves the Boltzmann transport equation, rather than the quasi-linear Fokker-Planck equation, for each particle step, where the distance traveled is sampled from an exponential probability distribution (Harding et al. 2016). Scattering is modeled by sampling a random vector at every particle step, which emulates a turbulent magnetic field (e.g., Harding et al. 2016). In this way, the code models the sub-resolution turbulent magnetic field as an isotropic field, with a proton-scattering opacity. Fraschetti et al. (2018) adopts a similar approach to follow the trajectories of CR particles accelerated in the stellar wind through the circumstellar disk. Likewise, they decompose the magnetic field into mean and turbulent components, where the mean component is given by MHD simulations and pitch-angle scattering produced by the turbulent component derived from an assumed Kolmogorov (1941) turbulent power spectrum (see also Fraschetti and Giacalone 2012).

Applications using such approaches suggest that the asymmetric magnetic field from core to stellar scales produces significant anisotropy in the CR flux that reaches the circumstellar disk (Fraschetti et al. 2018; Fitz Axen et al. 2021a). As in the radiation case, CRs can experience a flashlight effect, in which they preferentially leak out the outflow cavity due to a combination of lower-energy losses and magnetic focusing (Fitz Axen et al. 2021a). However, as in other CR approaches, the effective diffusion coefficient and level of anisotropy is sensitive to assumptions about the sub-resolution magnetized turbulence (Lazarian and Xu 2021; Zhang and Xu 2023).

## 8.5 Summary of challenges and future directions

Despite substantial progress in recent years, cosmic-ray hydrodynamics (CRHD) still faces major open challenges. Unlike radiation hydrodynamics (RHD), the basic transport physics of CRs remains highly uncertain (Sect. 8.1). The degree to which CRs scatter along or across magnetic fields, the importance of streaming instabilities, and the impact of damping processes such as ion-neutral and Landau damping are all poorly constrained, particularly in the multi-phase ISM and in molecular clouds. Similarly, while supernovae are well-established CR accelerators, the efficiency and spectral properties of CRs from protostellar jets, accretion shocks, or expanding H II regions remain uncertain.

On the numerical side, most CRHD methods still rely on simplified one-moment diffusion or streaming treatments, often with gray approximations that integrate over the CR spectrum (Sect. 8.2.1). Multi-bin formalisms (Sect. 8.3) now allow explicit spectral evolution, but at high computational cost. Two-moment methods (Sect. 8.2.2) improve the modeling of streaming and anisotropy, yet global galaxy simulations often find little difference in bulk outcomes such as the star formation rate compared to one-moment methods. Monte Carlo approaches (Sect. 8.4) promise higher accuracy and natural spectral resolution, but have so far only been applied in post-processing due to expense. The need for scalable implementations, possibly with GPU acceleration, is pressing.

Finally, observational constraints on CR transport are largely indirect, relying on gamma-ray emission, synchrotron radiation, or molecular abundances, which provide only limited leverage on diffusion coefficients and loss processes. Star-forming regions in particular show tentative evidence for enhanced CR ionization rates, but the magnitude and spatial structure of this enhancement remain debated.

Future progress will likely require multi-scale, multi-physics models that couple CR transport to MHD turbulence, chemistry, and radiative feedback, combined with hybrid fluid-particle methods that can capture both spectral evolution and anisotropy. Ultimately, predictive CRHD will depend on tighter synergy between theory, numerical models, and new observational diagnostics from facilities such as ALMA, JWST, and CTAO.

## 9 Conclusions

The physics of star formation spans a remarkable range of scales and processes, from supersonic turbulence to self-gravity, stellar feedback, radiation transfer, and cosmic-ray dynamics. Each of these ingredients is now modeled with increasing realism in modern simulation codes (cf. Table 1), yet major challenges remain.

For turbulence, the fundamental difficulty lies in the enormous Reynolds numbers of the ISM, Re  $\sim 10^9$ , which remain far beyond current computational capabilities. Advances such as positivity-preserving solvers, GPU acceleration, hybrid-precision techniques, and methods to track local dissipation rates (Sect. 3) are enabling progress, but bridging the gap to fully realistic turbulence is still a long-term goal. In gravity, solvers are generally robust (Sect. 4), but the treatment of interactions between gas and stars remains problematic: accurate stellar orbits embedded in dense gas likely require more widespread use of direct N-body summation despite its cost.

At the scale of star formation, robust sink particle treatments (Sect. 5) demand strict checks for gravitational collapse and careful conservation of mass, momentum, and angular momentum. These criteria are essential to avoid spurious fragmentation and inaccurate accretion. Stellar feedback (Sect. 6) adds further complexity: jets and outflows are critical for angular momentum transport and IMF regulation, while heating, winds, ionization, and supernovae each operate in different mass regimes. Progress here requires more comprehensive implementations of jet feedback, improved thermal treatments, and resolution-independent SN feedback models.

Radiation hydrodynamics (Sect. 7) presents perhaps the greatest numerical challenge due to its high dimensionality. Approximations remain unavoidable, whether gray moment methods with different closures (FLD, M1, VET) or Monte Carlo (MC) schemes. Each has strengths and weaknesses, with VET and MC providing the most accurate solutions but are either hard to implement (VET) or high in cost (MC). Multi-frequency extensions are now beginning to bridge the gap between idealized gray schemes and the complexity of real stellar and gas/dust, though full line transfer remains out of reach.

Cosmic-ray hydrodynamics (Sect. 8) shares some methodological parallels with RHD but faces even larger physical uncertainties. The propagation of CRs depends sensitively on poorly constrained scattering, streaming, and damping processes, while their sources outside supernovae remain uncertain. Numerically, one-moment diffusion models dominate current applications, though multi-bin spectral and two-moment approaches are emerging. Monte Carlo methods again offer conceptual simplicity and high accuracy but are not yet feasible in situ. Observational constraints are similarly limited, underscoring the need for closer ties between simulations and diagnostics such as gamma rays, synchrotron emission, and molecular abundances.

Looking forward, the most promising advances will come from methods that integrate across physics modules. Multi-scale, multi-physics approaches that couple turbulence, gravity, radiation, feedback, and CR transport will be required to create the most realistic models of star formation. Continued development of hybrid particle-fluid methods, combined with the increasing availability of GPU acceleration and exascale computing, will enable more accurate treatments of both microphysics and global ISM dynamics. Ultimately, progress in theory and computation must go hand in hand with improved observational diagnostics, ensuring that simulations remain grounded in measurable reality while continuing to push toward ever higher fidelity.

**Funding.** C.F. acknowledges funding provided by the Australian Research Council (Discovery Projects DP230102280 and DP250101526), and the Australia-Germany Joint Research Cooperation Scheme (UA-DAAD). S.O. acknowledges support from

NSF AST-2107340, NSF AST-2107942, NASA 80NSSC23K047, NSF AAG-2407522, a Peter O'Donnell Distinguished Researcher Fellowship, and a Donald Harrington Fellowship. We further acknowledge high-performance computing resources provided by the Leibniz Rechenzentrum and the Gauss Centre for Supercomputing (grants pr32lo, pr48pi and GCS Large-scale project 10391), the Australian National Computational Infrastructure (grant ek9) and the Pawsey Supercomputing Centre (project pawsey0810) in the framework of the National Computational Merit Allocation Scheme and the ANU Merit Allocation Scheme.

## References

- Abel T, Wandelt BD (2002) Adaptive ray tracing for radiative transfer around point sources. Mon Not R Astron Soc 330(3):L53–L56. https://doi.org/10.1046/j. 1365-8711.2002.05206.x, arXiv:astro-ph/0111033 [astro-ph]
- Achikanath Chirakkara R, Federrath C, Trivedi P, et al (2021) Efficient Highly Subsonic Turbulent Dynamo and Growth of Primordial Magnetic Fields. Phys Rev Lett 126(9):091103. https://doi.org/10.1103/PhysRevLett.126.091103, arXiv:2101.08256 [astro-ph.HE]
- Achikanath Chirakkara R, Seta A, Federrath C, et al (2024) Critical magnetic Reynolds number of the turbulent dynamo in collisionless plasmas. Mon Not R Astron Soc 528(1):937–953. https://doi.org/10.1093/mnras/stad3967, arXiv:2401.08499 [astro-ph.CO]
- Appenzeller I, Mundt R (1989) T Tauri stars. Astron Astrophys Rev 1:291–334. https://doi.org/10.1007/BF00873081
- Arzoumanian D, André P, Peretto N, et al (2013) Formation and evolution of interstellar filaments. Hints from velocity dispersion measurements. Astron Astrophys 553:A119. https://doi.org/10.1051/0004-6361/201220822, arXiv:1303.3024 [astro-ph.SR]
- Arzoumanian D, Shimajiri Y, Inutsuka Si, et al (2018) Molecular filament formation and filament-cloud interaction: Hints from Nobeyama 45 m telescope observations. Publ Astron Soc Japan 70:96. https://doi.org/10.1093/pasj/psy095, arXiv:1807.08968
- Aubert D, Teyssier R (2008) A radiative transfer scheme for cosmological reionization based on a local Eddington tensor. Mon Not R Astron Soc 387(1):295–307. https://doi.org/10.1111/j.1365-2966.2008.13223.x, arXiv:0709.1544 [astro-ph]
- Bacciotti F, Ray TP, Mundt R, et al (2002) Hubble Space Telescope/STIS Spectroscopy of the Optical Outflow from DG Tauri: Indications for Rotation in the Initial Jet Channel. Astrophys J 576:222–231. https://doi.org/10.1086/341725, astro-ph/0206175

- Bagla JS (2002) TreePM: A Code for Cosmological N-Body Simulations. J Astrophys Astron 23(3-4):185–196. https://doi.org/10.1007/BF02702282, arXiv:astro-ph/9911025 [astro-ph]
- Balay S, Gropp WD, McInnes LC, et al (1997) Efficient management of parallelism in object-oriented numerical software libraries. In: Arge E, Bruaset AM, Langtangen HP (eds) Modern Software Tools for Scientific Computing. Birkhäuser Boston, Boston, MA, pp 163–202, https://doi.org/10.1007/978-1-4612-1986-6\_8
- Banerjee R, Pudritz RE (2006) Outflows and Jets from Collapsing Magnetized Cloud Cores. Astrophys J 641:949–960. https://doi.org/10.1086/500496, arXiv:astro-ph/0508374
- Barnes J, Hut P (1986) A hierarchical O(N log N) force-calculation algorithm. Nature 324:446–449. https://doi.org/10.1038/324446a0
- Bate MR (2009a) The dependence of star formation on initial conditions and molecular cloud structure. Mon Not R Astron Soc 397(1):232–248. https://doi.org/10.1111/j.1365-2966.2009.14970.x, arXiv:0905.3562 [astro-ph.SR]
- Bate MR (2009b) The importance of radiative feedback for the stellar initial mass function. Mon Not R Astron Soc 392:1363–1380. https://doi.org/10.1111/j. 1365-2966.2008.14165.x, arXiv:0811.1035
- Bate MR (2012) Stellar, brown dwarf and multiple star properties from a radiation hydrodynamical simulation of star cluster formation. Mon Not R Astron Soc 419:3115–3146. https://doi.org/10.1111/j.1365-2966.2011.19955.x, arXiv:1110.1092 [astro-ph.SR]
- Bate MR (2018) On the diversity and statistical properties of protostellar discs. Mon Not R Astron Soc 475(4):5618–5658. https://doi.org/10.1093/mnras/sty169, arXiv:1801.07721 [astro-ph.SR]
- Bate MR, Burkert A (1997) Resolution requirements for smoothed particle hydrodynamics calculations with self-gravity. Mon Not R Astron Soc 288:1060–1072
- Bate MR, Bonnell IA, Price NM (1995) Modelling accretion in protobinary systems. Mon Not R Astron Soc 277(2):362–376. https://doi.org/10.1093/mnras/277.2.362, arXiv:astro-ph/9510149 [astro-ph]
- Bate MR, Bonnell IA, Bromm V (2003) The formation of a star cluster: predicting the properties of stars and brown dwarfs. Mon Not R Astron Soc 339:577–599. https://doi.org/10.1046/j.1365-8711.2003.06210.x, arXiv:astro-ph/0212380
- Beattie JR, Federrath C, Kriel N, et al (2023) Growth or Decay I: universality of the turbulent dynamo saturation. Mon Not R Astron Soc 524(3):3201–3214. https://doi.org/10.1093/mnras/stad1863, arXiv:2209.10749 [astro-ph.GA]

- Beattie JR, Federrath C, Klessen RS, et al (2025a) The spectrum of magnetized turbulence in the interstellar medium. Nature Astronomy https://doi.org/10.1038/s41550-025-02551-5, arXiv:2504.07136 [astro-ph.GA]
- Beattie JR, Federrath C, Kriel N, et al (2025b) Taking control of compressible modes: bulk viscosity and the turbulent dynamo. Mon Not R Astron Soc https://doi.org/10.1093/mnras/staf1318, arXiv:2312.03984 [astro-ph.GA]
- Beattie JR, Noer Kolborg A, Ramirez-Ruiz E, et al (2025c) So long Kolmogorov: the forward and backward turbulence cascades in a supernovae-driven, multiphase interstellar medium. arXiv e-prints arXiv:2501.09855. https://doi.org/10.48550/arXiv.2501.09855, arXiv:2501.09855 [astro-ph.GA]
- Beck R (2016) Magnetic fields in spiral galaxies. Astron Astrophys Rev 24:4. https://doi.org/10.1007/s00159-015-0084-4, arXiv:1509.04522
- Bell AR (2004) Turbulent amplification of magnetic field and diffusive shock acceleration of cosmic rays. Mon Not R Astron Soc 353(2):550–558. https://doi.org/10.1111/j.1365-2966.2004.08097.x
- Benz W (1988) Applications of smooth particle hydrodynamics (SPH) to astrophysical problems. Comput Phys Commun 48:97–105. https://doi.org/10.1016/0010-4655(88)90027-6
- Benzi R, Biferale L, Fisher RT, et al (2008) Intermittency and Universality in Fully Developed Inviscid and Weakly Compressible Turbulent Flows. Phys Rev Lett 100(23):234503. https://doi.org/10.1103/PhysRevLett.100.234503
- Beresnyak A, Lazarian A (2019) Turbulence in Magnetohydrodynamics. De Gruyter, Berlin, Boston, https://doi.org/doi:10.1515/9783110263282, URL https://doi.org/10.1515/9783110263282
- Berger MJ, Colella P (1989) Local adaptive mesh refinement for shock hydrodynamics. J Comput Phys 82:64–84. https://doi.org/10.1016/0021-9991(89)90035-1
- Birke C, Chalons C, Klingenberg C (2021) A low Mach two-speed relaxation scheme for the compressible Euler equations with gravity. arXiv e-prints arXiv:2112.02986. https://doi.org/10.48550/arXiv.2112.02986, arXiv:2112.02986 [math.NA]
- Birnboim Y, Balberg S, Teyssier R (2015) Galaxy evolution: modelling the role of non-thermal pressure in the interstellar medium. Mon Not R Astron Soc 447(4):3678–3692. https://doi.org/10.1093/mnras/stu2717, arXiv:1311.1206 [astro-ph.CO]
- Bjorkman JE, Wood K (2001) Radiative Equilibrium and Temperature Correction in Monte Carlo Radiation Transfer. Astrophys J 554(1):615–623. https://doi.org/10.1086/321336, arXiv:astro-ph/0103249 [astro-ph]

- Blandford RD, Payne DG (1982) Hydromagnetic flows from accretion discs and the production of radio jets. Mon Not R Astron Soc 199:883–903
- Bleuler A, Teyssier R (2014) Towards a more realistic sink particle algorithm for the RAMSES CODE. Mon Not R Astron Soc 445(4):4015–4036. https://doi.org/10.1093/mnras/stu2005, arXiv:1409.6528 [astro-ph.SR]
- Bode P, Ostriker JP, Xu G (2000) The Tree Particle-Mesh N-Body Gravity Solver. Astrophys J Suppl 128(2):561–569. https://doi.org/10.1086/313398, arXiv:astro-ph/9912541 [astro-ph]
- Book DL (1994) The Sedov self-similar point blast solutions in nonuniform media. Shock Waves 4(1):1–10. https://doi.org/10.1007/BF01414626
- Booth CM, Agertz O, Kravtsov AV, et al (2013) Simulations of Disk Galaxies with Cosmic Ray Driven Galactic Winds. Astrophys J Lett 777(1):L16. https://doi.org/10.1088/2041-8205/777/1/L16, arXiv:1308.4974 [astro-ph.GA]
- Bouchut F, Klingenberg C, Waagan K (2007) A multiwave approximate Riemann solver for ideal MHD based on relaxation. I: theoretical framework. Numerische Mathematik 108:7–42
- Brandenburg A, Rempel M (2019) Reversed Dynamo at Small Scales and Large Magnetic Prandtl Number. Astrophys J 879(1):57. https://doi.org/10.3847/1538-4357/ab24bd, arXiv:1903.11869 [astro-ph.SR]
- Brandenburg A, Sharma R, Vachaspati T (2023) Inverse cascading for initial magnetohydrodynamic turbulence spectra between Saffman and Batchelor. J Plasma Phys 89(6):905890606. https://doi.org/10.1017/S0022377823001253, arXiv:2307.04602 [physics.plasm-ph]
- Briggs W, Henson V, McCormick S (2000) A Multigrid Tutorial, 2nd edn. Society for Industrial and Applied Mathematics
- Bruls JHMJ, Vollmöller P, Schüssler M (1999) Computing radiative heating on unstructured spatial grids. Astron Astrophys 348:233–248
- Bryan GL, Norman ML, O'Shea BW, et al (2014) ENZO: An Adaptive Mesh Refinement Code for Astrophysics. Astrophys J Suppl 211:19. https://doi.org/10.1088/0067-0049/211/2/19, arXiv:1307.2265 [astro-ph.IM]
- Buntemeyer L, Banerjee R, Peters T, et al (2016) Radiation hydrodynamics using characteristics on adaptive decomposed domains for massively parallel star formation simulations. New Astron 43:49–69. https://doi.org/10.1016/j.newast.2015.07.002, arXiv:1501.04501

- Burge CA, Van Loo S, Falle SAEG, et al (2016) Ambipolar diffusion regulated collapse of filaments threaded by perpendicular magnetic fields. Astron Astrophys 596:A28. https://doi.org/10.1051/0004-6361/201629039, arXiv:1609.06879 [astro-ph.GA]
- Burgers JM (1948) A mathematical model illustrating the theory of turbulence. Advances in Applied Mechanics 1:171–199
- Burkhart B (2018) The Star Formation Rate in the Gravoturbulent Interstellar Medium. Astrophys J 863(2):118. https://doi.org/10.3847/1538-4357/aad002, arXiv:1801.05428 [astro-ph.GA]
- Burkhart B, Mocz P (2019) The Self-gravitating Gas Fraction and the Critical Density for Star Formation. Astrophys J 879(2):129. https://doi.org/10.3847/1538-4357/ab25ed, arXiv:1805.11104 [astro-ph.GA]
- Bustard C, Zweibel EG (2021) Cosmic-Ray Transport, Energy Loss, and Influence in the Multiphase Interstellar Medium. Astrophys J 913(2):106. https://doi.org/10.3847/1538-4357/abf64c, arXiv:2012.06585 [astro-ph.HE]
- Cabedo V, Maury A, Girart JM, et al (2023) Magnetically regulated collapse in the B335 protostar? II. Observational constraints on gas ionization and magnetic field coupling. Astron Astrophys 669:A90. https://doi.org/10.1051/0004-6361/202243813, arXiv:2204.10043 [astro-ph.GA]
- Camenzind M (1990) Magnetized Disk-Winds and the Origin of Bipolar Outflows. In: Klare G (ed) Reviews in Modern Astronomy, pp 234–265
- Caprioli D (2015) Cosmic-ray acceleration and propagation. In: 34th International Cosmic Ray Conference (ICRC2015), p 8, https://doi.org/10.22323/1.236.0008, arXiv:1510.07042
- Cesarsky CJ, Volk HJ (1978) Cosmic Ray Penetration into Molecular Clouds. Astron Astrophys 70:367
- Chabrier G (2003) Galactic Stellar and Substellar Initial Mass Function. Publ Astron Soc Pacific 115:763–795. https://doi.org/10.1086/376392, arXiv:astro-ph/0304382
- Chabrier G (2005) The Initial Mass Function: from Salpeter 1955 to 2005. In: Corbelli E, Palla F, Zinnecker H (eds) The Initial Mass Function 50 Years Later, p 41, astro-ph/0409465
- Chan TK, Kereš D, Hopkins PF, et al (2019) Cosmic ray feedback in the FIRE simulations: constraining cosmic ray propagation with GeV  $\gamma$ -ray emission. Mon Not R Astron Soc 488(3):3716–3744. https://doi.org/10.1093/mnras/stz1895, arXiv:1812.10496 [astro-ph.GA]

- Chirakkara RA, Federrath C, Seta A (2024) AHKASH: a new Hybrid particle-in-cell code for simulations of astrophysical collisionless plasma. Mon Not R Astron Soc https://doi.org/10.1093/mnras/stae2188, arXiv:2409.12151 [astro-ph.IM]
- Clark PC, Glover SCO, Klessen RS (2012) TreeCol: a novel approach to estimating column densities in astrophysical simulations. Mon Not R Astron Soc 420(1):745–756. https://doi.org/10.1111/j.1365-2966.2011.20087.x, arXiv:1109.3861 [astro-ph.GA]
- Commerçon B, Hennebelle P, Henning T (2011) Collapse of Massive Magnetized Dense Cores Using Radiation Magnetohydrodynamics: Early Fragmentation Inhibition. Astrophys J Lett 742:L9. https://doi.org/10.1088/2041-8205/742/1/L9, arXiv:1110.2955 [astro-ph.SR]
- Commerçon B, Marcowith A, Dubois Y (2019) Cosmic-ray propagation in the bistable interstellar medium. I. Conditions for cosmic-ray trapping. Astron Astrophys 622:A143. https://doi.org/10.1051/0004-6361/201833809, arXiv:1811.11509 [astro-ph.GA]
- Courant R, Friedrichs K, Lewy H (1928) Über die partiellen Differenzengleichungen der mathematischen Physik. Mathematische Annalen 100:32–74
- Cunningham AJ, Klein RI, Krumholz MR, et al (2011) Radiation-hydrodynamic Simulations of Massive Star Formation with Protostellar Outflows. Astrophys J 740:107. https://doi.org/10.1088/0004-637X/740/2/107, arXiv:1104.1218 [astro-ph.SR]
- Cure M, Araya I (2023) Radiation-Driven Wind Hydrodynamics of Massive Stars: A Review. arXiv e-prints arXiv:2305.11666. arXiv:2305.11666 [astro-ph.SR]
- Dale JE, Bonnell IA (2008) The effect of stellar winds on the formation of a protocluster. Mon Not R Astron Soc 391:2–13. https://doi.org/10.1111/j.1365-2966. 2008.13802.x, arXiv:0808.1510
- Dale JE, Ercolano B, Clarke CJ (2007) A new algorithm for modelling photoionizing radiation in smoothed particle hydrodynamics. Mon Not R Astron Soc 382(4):1759–1767. https://doi.org/10.1111/j.1365-2966.2007.12486.x, arXiv:0705.3396 [astro-ph]
- Dale JE, Ercolano B, Bonnell IA (2013) Ionization-induced star formation V. Triggering in partially unbound clusters. Mon Not R Astron Soc 431(2):1062–1076. https://doi.org/10.1093/mnras/stt236, arXiv:1302.1342 [astro-ph.GA]
- Davis SW, Stone JM, Jiang YF (2012) A Radiation Transfer Solver for Athena Using Short Characteristics. Astrophys J Suppl 199(1):9. https://doi.org/10.1088/0067-0049/199/1/9, arXiv:1201.2222 [astro-ph.IM]
- Derigs D, Winters AR, Gassner GJ, et al (2016) A novel high-order, entropy stable, 3D AMR MHD solver with guaranteed positive pressure. J Comput Phys 317:223–256. https://doi.org/10.1016/j.jcp.2016.04.048, arXiv:1605.03572 [astro-ph.GA]

- Dhruv A, Jain R, O'Neal J, et al (2023) Framework and Methodology for Verification of a Complex Scientific Simulation Software, Flash-X. World Congress in Computer Science, Computer Engineering, & Applied Computing (CSCE'23) arXiv:2308.16180. https://doi.org/10.48550/arXiv.2308.16180, arXiv:2308.16180 [cs.SE]
- Dong C, Wang L, Huang YM, et al (2022) Reconnection-driven energy cascade in magnetohydrodynamic turbulence. Science Advances 8(49):eabn7627. https://doi.org/10.1126/sciadv.abn7627, arXiv:2210.10736 [astro-ph.SR]
- Drury LOC, Strong AW (2017) Power requirements for cosmic ray propagation models involving diffusive reacceleration; estimates and implications for the damping of interstellar turbulence. Astron Astrophys 597:A117. https://doi.org/10.1051/0004-6361/201629526, arXiv:1608.04227 [astro-ph.HE]
- Dubey A, Fisher R, Graziani C, et al (2008) Challenges of Extreme Computing using the FLASH code. In: Pogorelov NV, Audit E, Zank GP (eds) Numerical Modeling of Space Plasma Flows, p 145
- Dubey A, Weide K, O'Neal J, et al (2022) Flash-X: A multiphysics simulation software instrument. SoftwareX 19:101168. https://doi.org/10.1016/j.softx.2022. 101168, arXiv:2208.11630 [physics.comp-ph]
- Dubois Y, Commerçon B (2016) An implicit scheme for solving the anisotropic diffusion of heat and cosmic rays in the RAMSES code. Astron Astrophys 585:A138. https://doi.org/10.1051/0004-6361/201527126, arXiv:1509.07037 [astro-ph.GA]
- Dullemond CP, Turolla R (2000) An efficient algorithm for two-dimensional radiative transfer in axisymmetric circumstellar envelopes and disks. Astron Astrophys 360:1187–1202. arXiv:astro-ph/0003456
- Elmegreen BG, Scalo J (2004) Interstellar Turbulence I: Observations and Processes. Annu Rev Astron Astrophys 42(1):211–273. https://doi.org/10.1146/annurev.astro.41.011802.094859, arXiv:astro-ph/0404451 [astro-ph]
- Ercolano B, Young PR, Drake JJ, et al (2008) X-Ray Enabled MOCASSIN: A Three-dimensional Code for Photoionized Media. Astrophys J Suppl 175(2):534–542. https://doi.org/10.1086/524378, arXiv:0710.2103 [astro-ph]
- Eswaran V, Pope SB (1988) An examination of forcing in direct numerical simulations of turbulence. Computers and Fluids 16:257–278
- Evoli C, Gaggero D, Vittino A, et al (2017) Cosmic-ray propagation with DRAGON2: I. numerical solver and astrophysical ingredients. J Cosmol Astropart Phys 2017(2):015. https://doi.org/10.1088/1475-7516/2017/02/015, arXiv:1607.07886 [astro-ph.HE]

- Falgout RD, Yang UM (2002) hypre: A library of high performance preconditioners. In: Sloot PMA, Hoekstra AG, Tan CJK, et al (eds) Computational Science ICCS 2002. Springer, Berlin, Heidelberg, pp 632–641
- Federrath C (2013) On the universality of supersonic turbulence. Mon Not R Astron Soc 436:1245–1257. https://doi.org/10.1093/mnras/stt1644, arXiv:1306.3989 [astro-ph.SR]
- Federrath C (2016) On the universality of interstellar filaments: theory meets simulations and observations. Mon Not R Astron Soc 457:375–388. https://doi.org/10.1093/mnras/stv2880, arXiv:1510.05654 [astro-ph.SR]
- Federrath C, Klessen RS (2012) The Star Formation Rate of Turbulent Magnetized Clouds: Comparing Theory, Simulations, and Observations. Astrophys J 761:156. https://doi.org/10.1088/0004-637X/761/2/156, arXiv:1209.2856 [astro-ph.SR]
- Federrath C, Klessen RS, Schmidt W (2008) The Density Probability Distribution in Compressible Isothermal Turbulence: Solenoidal versus Compressive Forcing. Astrophys J Lett 688:L79–L82. https://doi.org/10.1086/595280
- Federrath C, Banerjee R, Clark PC, et al (2010a) Modeling Collapse and Accretion in Turbulent Gas Clouds: Implementation and Comparison of Sink Particles in AMR and SPH. Astrophys J 713:269–290. https://doi.org/10.1088/0004-637X/713/1/269, arXiv:1001.4456
- Federrath C, Roman-Duval J, Klessen RS, et al (2010b) Comparing the statistics of interstellar turbulence in simulations and observations. Solenoidal versus compressive turbulence forcing. Astron Astrophys 512:A81. https://doi.org/10.1051/0004-6361/200912437
- Federrath C, Banerjee R, Seifried D, et al (2011a) Implementing and comparing sink particles in AMR and SPH. In: J. Alves, B. G. Elmegreen, J. M. Girart, & V. Trimble (ed) Computational Star Formation, pp 425–428, https://doi.org/10.1017/S1743921311000755, arXiv:1007.2504
- Federrath C, Chabrier G, Schober J, et al (2011b) Mach Number Dependence of Turbulent Magnetic Field Amplification: Solenoidal versus Compressive Flows. Phys Rev Lett 107(11):114504. https://doi.org/10.1103/PhysRevLett.107.114504, arXiv:1109.1760 [physics.flu-dyn]
- Federrath C, Schober J, Bovino S, et al (2014a) The Turbulent Dynamo in Highly Compressible Supersonic Plasmas. Astrophys J Lett 797(2):L19. https://doi.org/10.1088/2041-8205/797/2/L19, arXiv:1411.4707 [astro-ph.GA]
- Federrath C, Schrön M, Banerjee R, et al (2014b) Modeling Jet and Outflow Feedback during Star Cluster Formation. Astrophys J 790:128. https://doi.org/10.1088/0004-637X/790/2/128, arXiv:1406.3625 [astro-ph.SR]

- Federrath C, Rathborne JM, Longmore SN, et al (2016) The Link between Turbulence, Magnetic Fields, Filaments, and Star Formation in the Central Molecular Zone Cloud G0.253+0.016. Astrophys J 832:143. https://doi.org/10.3847/0004-637X/832/2/143, arXiv:1609.05911
- Federrath C, Krumholz M, Hopkins PF (2017) Converging on the Initial Mass Function of Stars. In: Journal of Physics Conference Series, p 012007, https://doi.org/10.1088/1742-6596/837/1/012007
- Federrath C, Klessen RS, Iapichino L, et al (2021) The sonic scale of interstellar turbulence. Nature Astronomy 5:365–371. https://doi.org/10.1038/s41550-020-01282-z, arXiv:2011.06238 [astro-ph.GA]
- Federrath C, Roman-Duval J, Klessen RS, et al (2022) TG: Turbulence Generator. Astrophysics Source Code Library, record ascl:2204.001, ascl:2204.001
- Fitz Axen M, Offner SSS, Gaches BAL, et al (2021a) Transport of Protostellar Cosmic Rays in Turbulent Dense Cores. Astrophys J 915(1):43. https://doi.org/10.3847/1538-4357/abfc55, arXiv:2105.00028 [astro-ph.GA]
- Fitz Axen M, Speicher J, Hungerford A, et al (2021b) Cosmic ray transport in mixed magnetic fields and their role on the observed anisotropies. Mon Not R Astron Soc 500(3):3497–3510. https://doi.org/10.1093/mnras/staa3500, arXiv:2101.07759 [astro-ph.HE]
- Fitz Axen M, Offner S, Hopkins PF, et al (2024) Suppressed Cosmic-Ray Energy Densities in Molecular Clouds from Streaming Instability-regulated Transport. Astrophys J 973(1):16. https://doi.org/10.3847/1538-4357/ad675a, arXiv:2407.17597 [astro-ph.GA]
- Fitz Axen M, Offner S, Hopkins PF, et al (2025) Gauging the Impact of Cosmic Ray Feedback on the Stellar Initial Mass Function. Astrophys J sub(1):16. https://doi.org/TBD, arXiv:TBD [astro-ph.GA]
- Frank A, Ray TP, Cabrit S, et al (2014) Jets and Outflows from Star to Cloud: Observations Confront Theory. In: Beuther H, Klessen RS, Dullemond CP, et al (eds) Protostars and Planets VI. University of Arizona Press, pp 451–474, https://doi.org/10.2458/azu\_uapress\_9780816531240-ch020, arXiv:1402.3553
- Frank M, Hauck CD, Olbrant E (2012) Perturbed, Entropy-Based Closure for Radiative Transfer. arXiv e-prints arXiv:1208.0772 [physics.comp-ph]
- Fraschetti F, Giacalone J (2012) Early-time Velocity Autocorrelation for Charged Particles Diffusion and Drift in Static Magnetic Turbulence. Astrophys J 755(2):114. https://doi.org/10.1088/0004-637X/755/2/114, arXiv:1206.6494 [astro-ph.HE]

- Fraschetti F, Drake JJ, Cohen O, et al (2018) Mottled Protoplanetary Disk Ionization by Magnetically Channeled T Tauri Star Energetic Particles. Astrophys J 853(2):112. https://doi.org/10.3847/1538-4357/aaa48b, arXiv:1710.01323 [astro-ph.HE]
- Frisch U (1995) Turbulence, the legacy of A. N. Kolmogorov. Cambridge University Press
- Fryxell B, Olson K, Ricker P, et al (2000) FLASH: An Adaptive Mesh Hydrodynamics Code for Modeling Astrophysical Thermonuclear Flashes. Astrophys J Suppl 131:273–334. https://doi.org/10.1086/317361
- Gaches BAL, Offner SSR (2018) Exploration of Cosmic-ray Acceleration in Protostellar Accretion Shocks and a Model for Ionization Rates in Embedded Protoclusters. Astrophys J 861(2):87. https://doi.org/10.3847/1538-4357/aac94d, arXiv:1805.03215 [astro-ph.GA]
- Gaches BAL, Offner SSR, Bisbas TG (2019) The Astrochemical Impact of Cosmic Rays in Protoclusters. I. Molecular Cloud Chemistry. Astrophys J 878(2):105. https://doi.org/10.3847/1538-4357/ab20c7, arXiv:1905.02232 [astro-ph.GA]
- Gaches BAL, Walch S, Lazarian A (2021) Cosmic-Ray Acceleration from Turbulence in Molecular Clouds. Astrophys J Lett 917(2):L39. https://doi.org/10.3847/2041-8213/ac1b2f, arXiv:2108.03250 [astro-ph.HE]
- Gaches BAL, Walch S, Wünsch R, et al (2023) Tree-based solvers for adaptive mesh refinement code FLASH IV. An X-ray radiation scheme to couple discrete and diffuse X-ray emission sources to the thermochemistry of the interstellar medium. Mon Not R Astron Soc 522(3):4674–4690. https://doi.org/10.1093/mnras/stad1206, arXiv:2301.13237 [astro-ph.IM]
- Gaches BAL, Grassi T, Vogt-Geisse S, et al (2024) The Astrochemistry Low-energy Electron Cross-Section (ALeCS) database. I. Semi-empirical electron-impact ionization cross-section calculations and ionization rates. Astron Astrophys 684:A41. https://doi.org/10.1051/0004-6361/202348293, arXiv:2310.10739 [astro-ph.GA]
- Galishnikova AK, Kunz MW, Schekochihin AA (2022) Tearing Instability and Current-Sheet Disruption in the Turbulent Dynamo. Physical Review X 12(4):041027. https://doi.org/10.1103/PhysRevX.12.041027, arXiv:2201.07757 [astro-ph.HE]
- Gatto A, Walch S, Naab T, et al (2017) The SILCC project III. Regulation of star formation and outflows by stellar winds and supernovae. Mon Not R Astron Soc 466(2):1903–1924. https://doi.org/10.1093/mnras/stw3209, arXiv:1606.05346 [astro-ph.GA]

- Geen S, Hennebelle P, Tremblin P, et al (2015a) Photoionization feedback in a self-gravitating, magnetized, turbulent cloud. Mon Not R Astron Soc 454(4):4484–4502. https://doi.org/10.1093/mnras/stv2272, arXiv:1507.02981 [astro-ph.GA]
- Geen S, Rosdahl J, Blaizot J, et al (2015b) A detailed study of feedback from a massive star. Mon Not R Astron Soc 448(4):3248–3264. https://doi.org/10.1093/mnras/stv251, arXiv:1412.0484 [astro-ph.GA]
- Geen S, Hennebelle P, Tremblin P, et al (2016) Feedback in Clouds II: UV photoionization and the first supernova in a massive cloud. Mon Not R Astron Soc 463(3):3129–3142. https://doi.org/10.1093/mnras/stw2235, arXiv:1607.05487 [astro-ph.GA]
- Geen S, Soler JD, Hennebelle P (2017) Interpreting the star formation efficiency of nearby molecular clouds with ionizing radiation. Mon Not R Astron Soc 471(4):4844–4855. https://doi.org/10.1093/mnras/stx1765, arXiv:1703.10071 [astro-ph.GA]
- Genovese L, Deutsch T, Neelov A, et al (2006) Efficient solution of poisson's equation with free boundary conditions. J Chem Phys 125(7):074105. https://doi.org/10.1063/1.2335442
- Girichidis P, Federrath C, Banerjee R, et al (2011) Importance of the initial conditions for star formation I. Cloud evolution and morphology. Mon Not R Astron Soc 413:2741–2759. https://doi.org/10.1111/j.1365-2966.2011.18348.x, arXiv:1008.5255 [astro-ph.SR]
- Girichidis P, Federrath C, Allison R, et al (2012a) Importance of the initial conditions for star formation III. Statistical properties of embedded protostellar clusters. Mon Not R Astron Soc 420:3264–3280. https://doi.org/10.1111/j.1365-2966.2011. 20250.x, arXiv:1111.5440 [astro-ph.SR]
- Girichidis P, Federrath C, Banerjee R, et al (2012b) Importance of the initial conditions for star formation II. Fragmentation-induced starvation and accretion shielding. Mon Not R Astron Soc 420:613–626. https://doi.org/10.1111/j. 1365-2966.2011.20073.x, arXiv:1110.1924 [astro-ph.SR]
- Girichidis P, Naab T, Walch S, et al (2014) Anisotropic transport and early dynamical impact of Cosmic Rays around Supernova remnants. arXiv e-prints arXiv:1406.4861. https://doi.org/10.48550/arXiv.1406.4861, arXiv:1406.4861 [astro-ph.HE]
- Girichidis P, Naab T, Walch S, et al (2016) Launching Cosmic-Ray-driven Outflows from the Magnetized Interstellar Medium. Astrophys J Lett 816(2):L19. https://doi.org/10.3847/2041-8205/816/2/L19, arXiv:1509.07247 [astro-ph.GA]
- Girichidis P, Pfrommer C, Hanasz M, et al (2020) Spectrally resolved cosmic ray hydrodynamics I. Spectral scheme. Mon Not R Astron Soc 491(1):993–1007. https://doi.org/10.1007/https://doi.org/10.1

- //doi.org/10.1093/mnras/stz2961, arXiv:1909.12840 [astro-ph.HE]
- Gjergo E, Zhang Z, Kroupa P, et al (2025) Massive Star Formation at Supersolar Metallicities: Constraints on the Initial Mass Function. arXiv e-prints arXiv:2509.20440. https://doi.org/10.48550/arXiv.2509.20440, arXiv:2509.20440 [astro-ph.GA]
- Glover SCO, Mac Low MM (2007a) Simulating the Formation of Molecular Clouds. I. Slow Formation by Gravitational Collapse from Static Initial Conditions. Astrophys J Suppl 169:239–268. https://doi.org/10.1086/512238, arXiv:astro-ph/0605120
- Glover SCO, Mac Low MM (2007b) Simulating the Formation of Molecular Clouds. II. Rapid Formation from Turbulent Initial Conditions. Astrophys J 659:1317–1337. https://doi.org/10.1086/512227, arXiv:astro-ph/0605121
- Glover SCO, Federrath C, Mac Low M, et al (2010) Modelling CO formation in the turbulent interstellar medium. Mon Not R Astron Soc 404:2–29. https://doi.org/10.1111/j.1365-2966.2009.15718.x, arXiv:0907.4081
- Gnedin NY, Abel T (2001) Multi-dimensional cosmological radiative transfer with a Variable Eddington Tensor formalism. New Astron 6(7):437–455. https://doi.org/10.1016/S1384-1076(01)00068-9, arXiv:astro-ph/0106278 [astro-ph]
- González M, Vaytet N, Commerçon B, et al (2015) Multigroup radiation hydrodynamics with flux-limited diffusion and adaptive mesh refinement. Astron Astrophys 578:A12. https://doi.org/10.1051/0004-6361/201525971, arXiv:1504.01894 [astroph.IM]
- Górski KM, Hivon E, Banday AJ, et al (2005) HEALPix: A Framework for High-Resolution Discretization and Fast Analysis of Data Distributed on the Sphere. Astrophys J 622(2):759–771. https://doi.org/10.1086/427976, arXiv:astro-ph/0409513 [astro-ph]
- Gotoh T, Fukayama D, Nakano T (2002) Velocity field statistics in homogeneous steady turbulence obtained using a high-resolution direct numerical simulation. Physics of Fluids 14(3):1065–1081. https://doi.org/10.1063/1.1448296
- Grisdale K, Agertz O, Renaud F, et al (2018) Physical properties and scaling relations of molecular clouds: the effect of stellar feedback. Mon Not R Astron Soc 479(3):3167–3180. https://doi.org/10.1093/mnras/sty1595, arXiv:1801.03104 [astro-ph.GA]
- Grudić MY, Guszejnov D, Hopkins PF, et al (2021) STARFORGE: Towards a comprehensive numerical model of star cluster formation and feedback. Mon Not R Astron Soc 506(2):2199–2231. https://doi.org/10.1093/mnras/stab1347, arXiv:2010.11254 [astro-ph.IM]

- Grudić MY, Guszejnov D, Offner SSR, et al (2022) The dynamics and outcome of star formation with jets, radiation, winds, and supernovae in concert. Mon Not R Astron Soc 512(1):216–232. https://doi.org/10.1093/mnras/stac526, arXiv:2201.00882 [astro-ph.GA]
- Guszejnov D, Krumholz MR, Hopkins PF (2016) The necessity of feedback physics in setting the peak of the initial mass function. Mon Not R Astron Soc 458:673–680. https://doi.org/10.1093/mnras/stw315, arXiv:1510.05040 [astro-ph.SR]
- Guszejnov D, Hopkins PF, Krumholz MR (2017) Protostellar feedback in turbulent fragmentation: consequences for stellar clustering and multiplicity. Mon Not R Astron Soc 468(4):4093–4106. https://doi.org/10.1093/mnras/stx725, arXiv:1610.00772 [astro-ph.GA]
- Guszejnov D, Hopkins PF, Grudić MY, et al (2018) Isothermal Fragmentation: Is there a low-mass cut-off? Mon Not R Astron Soc 480:182-191. https://doi.org/10. 1093/mnras/sty1847, arXiv:1804.08574
- Guszejnov D, Grudić MY, Hopkins PF, et al (2021) STARFORGE: the effects of protostellar outflows on the IMF. Mon Not R Astron Soc 502(3):3646–3663. https://doi.org/10.1093/mnras/stab278, arXiv:2010.11249 [astro-ph.GA]
- Guszejnov D, Grudić MY, Offner SSR, et al (2022) Effects of the environment and feedback physics on the initial mass function of stars in the STARFORGE simulations. Mon Not R Astron Soc 515(4):4929–4952. https://doi.org/10.1093/mnras/stac2060, arXiv:2205.10413 [astro-ph.GA]
- Haid S, Walch S, Naab T, et al (2016) Supernova blast waves in wind-blown bubbles, turbulent, and power-law ambient media. Mon Not R Astron Soc 460(3):2962–2978. https://doi.org/10.1093/mnras/stw1082, arXiv:1604.04395 [astro-ph.GA]
- Haid S, Walch S, Seifried D, et al (2019) SILCC-Zoom: The early impact of ionizing radiation on forming molecular clouds. Mon Not R Astron Soc 482(3):4062–4083. https://doi.org/10.1093/mnras/sty2938, arXiv:1810.08210 [astro-ph.GA]
- Hanasz M, Lesch H, Naab T, et al (2013) Cosmic Rays Can Drive Strong Outflows from Gas-rich High-redshift Disk Galaxies. Astrophys J Lett 777(2):L38. https://doi.org/10.1088/2041-8205/777/2/L38, arXiv:1310.3273 [astro-ph.GA]
- Harding JP, Fryer CL, Mendel S (2016) Explaining TeV Cosmic-Ray Anisotropies with Non-diffusive Cosmic-Ray Propagation. Astrophys J 822(2):102. https://doi.org/10.3847/0004-637X/822/2/102, arXiv:1510.02487 [astro-ph.HE]
- Harries TJ (2015) Radiation-hydrodynamical simulations of massive star formation using Monte Carlo radiative transfer I. Algorithms and numerical methods. Mon Not R Astron Soc 448(4):3156–3166. https://doi.org/10.1093/mnras/stv158, arXiv:1501.05754 [astro-ph.SR]

- Harries TJ, Haworth TJ, Acreman D, et al (2019) The TORUS radiation transfer code. Astronomy and Computing 27:63. https://doi.org/10.1016/j.ascom.2019.03.002, arXiv:1903.06672 [astro-ph.SR]
- Haugen NE, Brandenburg A, Dobler W (2004a) Simulations of nonhelical hydromagnetic turbulence. Phys Rev Lett 70(1):016308. https://doi.org/10.1103/PhysRevE. 70.016308, arXiv:astro-ph/0307059 [astro-ph]
- Haugen NEL, Brandenburg A (2004) Suppression of small scale dynamo action by an imposed magnetic field. Phys Rev Lett 70(3):036408. https://doi.org/10.1103/PhysRevE.70.036408, arXiv:astro-ph/0402281 [astro-ph]
- Haugen NEL, Brandenburg A, Mee AJ (2004b) Mach number dependence of the onset of dynamo action. Mon Not R Astron Soc 353:947–952. https://doi.org/10.1111/j. 1365-2966.2004.08127.x
- Haworth TJ, Glover SCO, Koepferl CM, et al (2018) Synthetic observations of star formation and the interstellar medium. New Astron Rev 82:1–58. https://doi.org/10.1016/j.newar.2018.06.001, arXiv:1711.05275 [astro-ph.GA]
- Hayes JC, Norman ML (2003) Beyond Flux-limited Diffusion: Parallel Algorithms for Multidimensional Radiation Hydrodynamics. Astrophys J Suppl 147(1):197–220. https://doi.org/10.1086/374658, arXiv:astro-ph/0207260 [astro-ph]
- He CC, Ricotti M (2023) Massive pre-stellar cores in radiation-magneto-turbulent simulations of molecular clouds. Mon Not R Astron Soc 522(4):5374–5392. https://doi.org/10.1093/mnras/stad1289, arXiv:2210.11629 [astro-ph.GA]
- He CC, Wibking BD, Krumholz MR (2024a) A novel numerical method for mixed-frame multigroup radiation-hydrodynamics with GPU acceleration implemented in the QUOKKA code. Mon Not R Astron Soc 535(4):3059–3076. https://doi.org/10.1093/mnras/stae2580, arXiv:2407.18304 [astro-ph.GA]
- He CC, Wibking BD, Krumholz MR (2024b) An asymptotically correct implicit-explicit time integration scheme for finite volume radiation-hydrodynamics. Mon Not R Astron Soc 531(1):1228–1242. https://doi.org/10.1093/mnras/stae1244, arXiv:2404.08247 [astro-ph.IM]
- Hennebelle P, Chabrier G (2008) Analytical Theory for the Initial Mass Function: CO Clumps and Prestellar Cores. Astrophys J 684:395–410. https://doi.org/10.1086/589916, arXiv:0805.0691
- Hennebelle P, Chabrier G (2009) Analytical Theory for the Initial Mass Function. II. Properties of the Flow. Astrophys J 702:1428–1442. https://doi.org/10.1088/0004-637X/702/2/1428, arXiv:0907.2765

- Hennebelle P, Chabrier G (2011) Analytical Star Formation Rate from Gravoturbulent Fragmentation. Astrophys J Lett 743:L29. https://doi.org/10.1088/2041-8205/743/2/L29, arXiv:1110.0033 [astro-ph.GA]
- Hennebelle P, Chabrier G (2013) Analytical Theory for the Initial Mass Function. III. Time Dependence and Star Formation Rate. Astrophys J 770:150. https://doi.org/10.1088/0004-637X/770/2/150, arXiv:1304.6637 [astro-ph.GA]
- Hennebelle P, Falgarone E (2012) Turbulent molecular clouds. Astron Astrophys Rev 20:55. https://doi.org/10.1007/s00159-012-0055-y, arXiv:1211.0637 [astro-ph.GA]
- Hennebelle P, Fromang S (2008) Magnetic processes in a collapsing dense core. I. Accretion and ejection. Astron Astrophys 477:9–24. https://doi.org/10.1051/0004-6361:20078309, arXiv:0709.2886
- Hennebelle P, Commerçon B, Lee YN, et al (2020) What Is the Role of Stellar Radiative Feedback in Setting the Stellar Mass Spectrum? Astrophys J 904(2):194. https://doi.org/10.3847/1538-4357/abbfab, arXiv:2010.03539 [astro-ph.GA]
- Hennebelle P, Lebreuilly U, Colman T, et al (2022) Influence of magnetic field and stellar radiative feedback on the collapse and the stellar mass spectrum of a massive star-forming clump. Astron Astrophys 668:A147. https://doi.org/10.1051/0004-6361/202243803, arXiv:2210.12475 [astro-ph.GA]
- Hennebelle P, Brucy N, Colman T (2024) Inefficient star formation in high Mach number environments: I. The turbulent support analytical model. Astron Astrophys 690:A43. https://doi.org/10.1051/0004-6361/202450524, arXiv:2404.17368 [astro-ph.GA]
- Hirose S, Krolik JH, Stone JM (2006) Vertical Structure of Gas Pressure-dominated Accretion Disks with Local Dissipation of Turbulence and Radiative Transport. Astrophys J 640(2):901–917. https://doi.org/10.1086/499153, arXiv:astro-ph/0510741 [astro-ph]
- Hopkins AM (2018) The Dawes Review 8: Measuring the Stellar Initial Mass Function. ArXiv e-prints arXiv:1807.09949
- Hopkins PF (2012) An excursion-set model for the structure of giant molecular clouds and the interstellar medium. Mon Not R Astron Soc 423:2016–2036. https://doi.org/10.1111/j.1365-2966.2012.20730.x
- Hopkins PF (2013a) A general class of Lagrangian smoothed particle hydrodynamics methods and implications for fluid mixing problems. Mon Not R Astron Soc 428:2840–2856. https://doi.org/10.1093/mnras/sts210, arXiv:1206.5006 [astro-ph.IM]

- Hopkins PF (2013b) A general theory of turbulent fragmentation. Mon Not R Astron Soc 430:1653–1693. https://doi.org/10.1093/mnras/sts704, arXiv:1210.0903 [astro-ph.CO]
- Hopkins PF (2015) A new class of accurate, mesh-free hydrodynamic simulation methods. Mon Not R Astron Soc 450(1):53–110. https://doi.org/10.1093/mnras/stv195, arXiv:1409.7395 [astro-ph.CO]
- Hopkins PF (2025) Cosmic Rays on Galaxy Scales: Progress and Pitfalls for CR-MHD Dynamical Models. arXiv e-prints arXiv:2509.07104. https://doi.org/10.48550/arXiv.2509.07104, arXiv:2509.07104 [astro-ph.GA]
- Hopkins PF, Grudić MY (2019) Numerical problems in coupling photon momentum (radiation pressure) to gas. Mon Not R Astron Soc 483(3):4187–4196. https://doi.org/10.1093/mnras/sty3089, arXiv:1803.07573 [astro-ph.GA]
- Hopkins PF, Wetzel A, Kereš D, et al (2018) How to model supernovae in simulations of star and galaxy formation. Mon Not R Astron Soc 477(2):1578–1603. https://doi.org/10.1093/mnras/sty674, arXiv:1707.07010 [astro-ph.GA]
- Hopkins PF, Chan TK, Squire J, et al (2021a) Effects of different cosmic ray transport models on galaxy formation. Mon Not R Astron Soc 501(3):3663–3669. https://doi.org/10.1093/mnras/staa3692, arXiv:2004.02897 [astro-ph.GA]
- Hopkins PF, Squire J, Chan TK, et al (2021b) Testing physical models for cosmic ray transport coefficients on galactic scales: self-confinement and extrinsic turbulence at ~GeV energies. Mon Not R Astron Soc 501(3):4184–4213. https://doi.org/10.1093/mnras/staa3691, arXiv:2002.06211 [astro-ph.HE]
- Hopkins PF, Butsky IS, Panopoulou GV, et al (2022) First predicted cosmic ray spectra, primary-to-secondary ratios, and ionization rates from MHD galaxy formation simulations. Mon Not R Astron Soc 516(3):3470–3514. https://doi.org/10.1093/mnras/stac1791, arXiv:2109.09762 [astro-ph.HE]
- Hopkins PF, Grudic MY, Kremer K, et al (2024) FORGE'd in FIRE III: The IMF in Quasar Accretion Disks from STARFORGE. The Open Journal of Astrophysics 7:71. https://doi.org/10.33232/001c.122857, arXiv:2404.08046 [astro-ph.GA]
- Hu CY, Naab T, Walch S, et al (2016) Star formation and molecular hydrogen in dwarf galaxies: a non-equilibrium view. Mon Not R Astron Soc 458(4):3528–3553. https://doi.org/10.1093/mnras/stw544, arXiv:1510.05644 [astro-ph.GA]
- Hu Y, Xu S, Stone JM, et al (2022) Turbulent Magnetic Field Amplification by the Interaction of a Shock Wave and Inhomogeneous Medium. Astrophys J 941(2):133. https://doi.org/10.3847/1538-4357/ac9ebc, arXiv:2207.06941 [astro-ph.GA]

- Hubber D, Batty C, McLeod A, et al (2011a) SEREN: A SPH code for star and planet formation simulations. Astrophysics Source Code Library, record ascl:1102.010
- Hubber DA, Batty CP, McLeod A, et al (2011b) SEREN a new SPH code for star and planet formation simulations. Algorithms and tests. Astron Astrophys 529:A27. https://doi.org/10.1051/0004-6361/201014949, arXiv:1102.0721 [astro-ph.SR]
- Hubber DA, Walch S, Whitworth AP (2013) An improved sink particle algorithm for SPH simulations. Mon Not R Astron Soc 430(4):3261–3275. https://doi.org/10.1093/mnras/stt128, arXiv:1301.4520 [astro-ph.IM]
- Ibáñez-Mejía JC, Mac Low MM, Klessen RS, et al (2017) Feeding versus Falling: The Growth and Collapse of Molecular Clouds in a Turbulent Interstellar Medium. Astrophys J 850(1):62. https://doi.org/10.3847/1538-4357/aa93fe, arXiv:1705.01779 [astro-ph.GA]
- Ishihara T, Kaneda Y, Morishita K, et al (2020) Second-order velocity structure functions in direct numerical simulations of turbulence with  $R_{\lambda}$  up to 2250. Phys Rev Fluids 5(10):104608. https://doi.org/10.1103/PhysRevFluids.5.104608
- Jappsen AK, Klessen RS, Larson RB, et al (2005) The stellar mass spectrum from non-isothermal gravoturbulent fragmentation. Astron Astrophys 435:611–623. https://doi.org/10.1051/0004-6361:20042178, arXiv:astro-ph/0410351
- Jerabkova T, Romano D, Kroupa P, et al (2025) Cosmic Threads: Interlinking the Stellar Initial Mass Function from Star-Birth to Galaxies. arXiv e-prints arXiv:2509.06886. https://doi.org/10.48550/arXiv.2509.06886, arXiv:2509.06886 [astro-ph.GA]
- Jiang YF, Oh SP (2018) A New Numerical Scheme for Cosmic-Ray Transport. Astrophys J 854(1):5. https://doi.org/10.3847/1538-4357/aaa6ce, arXiv:1712.07117 [astro-ph.HE]
- Jiang YF, Stone JM, Davis SW (2012) A Godunov Method for Multidimensional Radiation Magnetohydrodynamics Based on a Variable Eddington Tensor. Astrophys J Suppl 199(1):14. https://doi.org/10.1088/0067-0049/199/1/14, arXiv:1201.2223 [astro-ph.HE]
- Jones MO, Bate MR (2018) Sink particle radiative feedback in smoothed particle hydrodynamics models of star formation. Mon Not R Astron Soc 480(2):2562–2577. https://doi.org/10.1093/mnras/sty1969, arXiv:1807.09849 [astro-ph.SR]
- Jørgensen JK, Belloche A, Garrod RT (2020) Astrochemistry During the Formation of Stars. Annu Rev Astron Astrophys 58:727–778. https://doi.org/10.1146/annurev-astro-032620-021927, arXiv:2006.07071 [astro-ph.SR]

- Kang C, Kimm T, Han D, et al (2025) Impact of star formation models on the growth of simulated galaxies at high redshifts. Astron Astrophys 693:A149. https://doi.org/10.1051/0004-6361/202451502, arXiv:2407.12090 [astro-ph.GA]
- Kannan R, Vogelsberger M, Marinacci F, et al (2019) AREPO-RT: radiation hydrodynamics on a moving mesh. Mon Not R Astron Soc 485(1):117–149. https://doi.org/10.1093/mnras/stz287, arXiv:1804.01987 [astro-ph.IM]
- Kempski P, Fielding DB, Quataert E, et al (2025) Self-Similar Cosmic-Ray Transport in High-Resolution Magnetohydrodynamic Turbulence. Astrophys J Lett arXiv:2507.10651. https://doi.org/10.48550/arXiv.2507.10651, arXiv:2507.10651 [astro-ph.HE]
- Kim CG, Ostriker EC (2017) Three-phase Interstellar Medium in Galaxies Resolving Evolution with Star Formation and Supernova Feedback (TIGRESS): Algorithms, Fiducial Model, and Convergence. Astrophys J 846(2):133. https://doi.org/10.3847/1538-4357/aa8599, arXiv:1612.03918 [astro-ph.GA]
- Kim JG, Kim WT, Ostriker EC, et al (2017) Modeling UV Radiation Feedback from Massive Stars. I. Implementation of Adaptive Ray-tracing Method and Tests. Astrophys J 851(2):93. https://doi.org/10.3847/1538-4357/aa9b80, arXiv:1711.06277 [astro-ph.IM]
- Kim JG, Kim WT, Ostriker EC (2018) Modeling UV Radiation Feedback from Massive Stars. II. Dispersal of Star-forming Giant Molecular Clouds by Photoionization and Radiation Pressure. Astrophys J 859(1):68. https://doi.org/10.3847/1538-4357/aabe27, arXiv:1804.04664 [astro-ph.GA]
- Kim JG, Kim WT, Ostriker EC (2019) Modeling UV Radiation Feedback from Massive Stars. III. Escape of Radiation from Star-forming Giant Molecular Clouds. Astrophys J 883(1):102. https://doi.org/10.3847/1538-4357/ab3d3d, arXiv:1908.07549 [astro-ph.GA]
- Kim JG, Ostriker EC, Filippova N (2021) Star Formation Efficiency and Dispersal of Giant Molecular Clouds with UV Radiation Feedback: Dependence on Gravitational Boundedness and Magnetic Fields. Astrophys J 911(2):128. https://doi.org/10.3847/1538-4357/abe934, arXiv:2011.07772 [astro-ph.GA]
- Kissmann R (2014) PICARD: A novel code for the Galactic Cosmic Ray propagation problem. Astroparticle Physics 55:37–50. https://doi.org/10.1016/j.astropartphys. 2014.02.002, arXiv:1401.4035 [astro-ph.HE]
- Kitsionas S, Federrath C, Klessen RS, et al (2009) Algorithmic comparisons of decaying, isothermal, supersonic turbulence. Astron Astrophys 508:541–560. https://doi.org/10.1051/0004-6361/200811170, arXiv:0810.4599

- Klassen M, Peters T, Pudritz RE (2012) H II Region Variability and Pre-main-sequence Evolution. Astrophys J 758(2):137. https://doi.org/10.1088/0004-637X/758/2/137, arXiv:1208.6001 [astro-ph.GA]
- Klassen M, Kuiper R, Pudritz RE, et al (2014) A General Hybrid Radiation Transport Scheme for Star Formation Simulations on an Adaptive Grid. Astrophys J 797(1):4. https://doi.org/10.1088/0004-637X/797/1/4, arXiv:1410.4259 [astro-ph.GA]
- Klepitko A, Walch S, Wünsch R, et al (2023) Tree-based solvers for adaptive mesh refinement code FLASH III: a novel scheme for radiation pressure on dust and gas and radiative transfer from diffuse sources. Mon Not R Astron Soc 521(1):160–184. https://doi.org/10.1093/mnras/stad385, arXiv:2204.09072 [astro-ph.IM]
- Klessen RS (2001) The Formation of Stellar Clusters: Mass Spectra from Turbulent Molecular Cloud Fragmentation. Astrophys J 556:837–846. https://doi.org/10.1086/321626, arXiv:astro-ph/0104127
- Klessen RS, Heitsch F, Mac Low MM (2000) Gravitational Collapse in Turbulent Molecular Clouds. I. Gasdynamical Turbulence. Astrophys J 535:887–906. https://doi.org/10.1086/308891, arXiv:astro-ph/9911068
- Koch EW, Ward CG, Offner S, et al (2017) Identifying tools for comparing simulations and observations of spectral-line data cubes. Mon Not R Astron Soc 471(2):1506–1530. https://doi.org/10.1093/mnras/stx1671, arXiv:1707.05415 [astro-ph.GA]
- Koch EW, Rosolowsky EW, Boyden RD, et al (2019) TURBUSTAT: Turbulence Statistics in Python. Astron J 158(1):1. https://doi.org/10.3847/1538-3881/ab1cc0, arXiv:1904.10484 [astro-ph.IM]
- Kolmogorov AN (1941) Dissipation of energy in locally isotropic turbulence. Dokl Akad Nauk SSSR 32:16–18
- Königl A, Pudritz RE (2000) Disk Winds and the Accretion-Outflow Connection. Protostars and Planets IV p 759. astro-ph/9903168
- Koo BC, McKee CF (1992) Dynamics of Wind Bubbles and Superbubbles. II. Analytic Theory. Astrophys J 388:103. https://doi.org/10.1086/171133
- Koyama H, Inutsuka Si (2002) An Origin of Supersonic Motions in Interstellar Clouds. Astrophys J Lett 564(2):L97–L100. https://doi.org/10.1086/338978, arXiv:astro-ph/0112420 [astro-ph]
- Kravtsov AV, Klypin AA, Khokhlov AM (1997) Adaptive Refinement Tree: A New High-Resolution N-Body Code for Cosmological Simulations. Astrophys J Suppl 111(1):73–94. https://doi.org/10.1086/313015, arXiv:astro-ph/9701195 [astro-ph]

- Kravtsov AV, Klypin A, Hoffman Y (2002) Constrained Simulations of the Real Universe. II. Observational Signatures of Intergalactic Gas in the Local Supercluster Region. Astrophys J 571(2):563–575. https://doi.org/10.1086/340046, arXiv:astro-ph/0109077 [astro-ph]
- Kriel N, Beattie JR, Seta A, et al (2022) Fundamental scales in the kinematic phase of the turbulent dynamo. Mon Not R Astron Soc 513(2):2457–2470. https://doi.org/10.1093/mnras/stac969, arXiv:2204.00828 [astro-ph.SR]
- Kriel N, Beattie JR, Federrath C, et al (2025) Fundamental MHD scales II. The kinematic phase of the supersonic small-scale dynamo. Mon Not R Astron Soc 537(3):2602–2629. https://doi.org/10.1093/mnras/staf188, arXiv:2310.17036 [astro-ph.GA]
- Kritsuk AG, Nordlund Å, Collins D, et al (2011) Comparing Numerical Methods for Isothermal Magnetized Supersonic Turbulence. Astrophys J 737:13. https://doi.org/10.1088/0004-637X/737/1/13, arXiv:1103.5525 [astro-ph.SR]
- Kroupa P (2001) On the variation of the initial mass function. Mon Not R Astron Soc 322:231–246. https://doi.org/10.1046/j.1365-8711.2001.04022.x, arXiv:astro-ph/0009005
- Kroupa P, Weidner C, Pflamm-Altenburg J, et al (2013) 'The Stellar and Sub-Stellar Initial Mass Function of Simple and Composite Populations' in Planets, Stars and Stellar Systems. Volume 5: Galactic Structure and Stellar Populations. In: Oswalt TD, Gilmore G (eds) Planets, Stars and Stellar Systems. Volume 5: Galactic Structure and Stellar Populations. Springer, p 115, https://doi.org/10.1007/978-94-007-5612-0\_4
- Kroupa P, Gjergo E, Jerabkova T, et al (2026) The initial mass function of stars. In: Encyclopedia of Astrophysics, pp 173–210, https://doi.org/10.1016/B978-0-443-21439-4.00035-3
- Krumholz MR, McKee CF (2005) A General Theory of Turbulence-regulated Star Formation, from Spirals to Ultraluminous Infrared Galaxies. Astrophys J 630:250–268. https://doi.org/10.1086/431734, arXiv:astro-ph/0505177
- Krumholz MR, McKee CF, Klein RI (2004) Embedding Lagrangian Sink Particles in Eulerian Grids. Astrophys J 611:399–412. https://doi.org/10.1086/421935, arXiv:astro-ph/0312612
- Krumholz MR, Klein RI, McKee CF (2007a) Radiation-Hydrodynamic Simulations of Collapse and Fragmentation in Massive Protostellar Cores. Astrophys J 656:959–979. https://doi.org/10.1086/510664, arXiv:astro-ph/0609798
- Krumholz MR, Klein RI, McKee CF, et al (2007b) Equations and Algorithms for Mixed-frame Flux-limited Diffusion Radiation Hydrodynamics. Astrophys J

- 667(1):626-643. https://doi.org/10.1086/520791, arXiv:astro-ph/0611003 [astro-ph]
- Krumholz MR, Klein RI, McKee CF, et al (2009) The Formation of Massive Star Systems by Accretion. Science 323(5915):754. https://doi.org/10.1126/science.1165857, arXiv:0901.3157 [astro-ph.SR]
- Krumholz MR, Klein RI, McKee CF (2012) Radiation-hydrodynamic Simulations of the Formation of Orion-like Star Clusters. II. The Initial Mass Function from Winds, Turbulence, and Radiation. Astrophys J 754:71. https://doi.org/10.1088/0004-637X/754/1/71, arXiv:1203.2620 [astro-ph.SR]
- Krumholz MR, Myers AT, Klein RI, et al (2016) What physics determines the peak of the IMF? Insights from the structure of cores in radiation-magnetohydrodynamic simulations. Mon Not R Astron Soc 460:3272–3283. https://doi.org/10.1093/mnras/stw1236, arXiv:1603.04557
- Krumholz MR, Crocker RM, Sampson ML (2022) Cosmic ray interstellar propagation tool using Itô Calculus (CRIPTIC): software for simultaneous calculation of cosmic ray transport and observational signatures. Mon Not R Astron Soc 517(1):1355–1380. https://doi.org/10.1093/mnras/stac2712, arXiv:2207.13838 [astro-ph.HE]
- Krumholz MR, Crocker RM, Offner SSR (2023) The cosmic ray ionization and  $\gamma$ -ray budgets of star-forming galaxies. Mon Not R Astron Soc 520(4):5126–5143. https://doi.org/10.1093/mnras/stad459, arXiv:2211.03488 [astro-ph.GA]
- Kuffmeier M, Haugbølle T, Nordlund Å (2017) Zoom-in Simulations of Protoplanetary Disks Starting from GMC Scales. Astrophys J 846(1):7. https://doi.org/10.3847/1538-4357/aa7c64, arXiv:1611.10360 [astro-ph.SR]
- Kuiper R, Hosokawa T (2018) First hydrodynamics simulations of radiation forces and photoionization feedback in massive star formation. Astron Astrophys 616:A101. https://doi.org/10.1051/0004-6361/201832638, arXiv:1804.10211 [astro-ph.GA]
- Kuiper R, Klessen RS (2013) The reliability of approximate radiation transport methods for irradiated disk studies. Astron Astrophys 555:A7. https://doi.org/10.1051/0004-6361/201321404, arXiv:1305.2197 [astro-ph.SR]
- Kuiper R, Klahr H, Dullemond C, et al (2010) Fast and accurate frequency-dependent radiation transport for hydrodynamics simulations in massive star formation. Astron Astrophys 511:A81. https://doi.org/10.1051/0004-6361/200912355, arXiv:1001.3301 [astro-ph.SR]
- Lancaster L, Ostriker EC, Kim JG, et al (2021a) Efficiently Cooled Stellar Wind Bubbles in Turbulent Clouds. I. Fractal Theory and Application to Starforming Clouds. Astrophys J 914(2):89. https://doi.org/10.3847/1538-4357/abf8ab, arXiv:2104.07691 [astro-ph.GA]

- Lancaster L, Ostriker EC, Kim JG, et al (2021b) Efficiently Cooled Stellar Wind Bubbles in Turbulent Clouds. II. Validation of Theory with Hydrodynamic Simulations. Astrophys J 914(2):90. https://doi.org/10.3847/1538-4357/abf8ac, arXiv:2104.07722 [astro-ph.GA]
- Lane HB, Grudić MY, Guszejnov D, et al (2022) Less wrong: a more realistic initial condition for simulations of turbulent molecular clouds. Mon Not R Astron Soc 510(4):4767–4778. https://doi.org/10.1093/mnras/stab3739, arXiv:2110.14816 [astro-ph.GA]
- Lazarian A, Xu S (2021) Diffusion of Cosmic Rays in MHD Turbulence with Magnetic Mirrors. Astrophys J 923(1):53. https://doi.org/10.3847/1538-4357/ac2de9, arXiv:2106.08362 [astro-ph.HE]
- Lazarian A, Xu S (2022) Damping of Alfvén Waves in MHD Turbulence and Implications for Cosmic Ray Streaming Instability and Galactic Winds. Frontiers in Physics 10:702799. https://doi.org/10.3389/fphy.2022.702799, arXiv:2201.05168 [astro-ph.GA]
- Lazarian A, Eyink GL, Jafari A, et al (2020) 3D turbulent reconnection: Theory, tests, and astrophysical implications. Phys Plasmas 27(1):012305. https://doi.org/10.1063/1.5110603, arXiv:2001.00868 [astro-ph.HE]
- Lebreuilly U, Hennebelle P, Colman T, et al (2021) Protoplanetary Disk Birth in Massive Star-forming Clumps: The Essential Role of the Magnetic Field. Astrophys J Lett 917(1):L10. https://doi.org/10.3847/2041-8213/ac158c, arXiv:2107.08491 [astro-ph.SR]
- Lebreuilly U, Hennebelle P, Maury A, et al (2024) Influence of protostellar outflows on star and protoplanetary disk formation in a massive star-forming clump. Astron Astrophys 683:A13. https://doi.org/10.1051/0004-6361/202347913, arXiv:2309.05397 [astro-ph.SR]
- Lee D, Deane AE, Federrath C (2009) A New Multidimensional Unsplit MHD Solver in FLASH3. In: N. V. Pogorelov, E. Audit, P. Colella, & G. P. Zank (ed) Numerical Modeling of Space Plasma Flows: ASTRONUM-2008, p 243
- Lee YN, Offner SSR, Hennebelle P, et al (2020) The Origin of the Stellar Mass Distribution and Multiplicity. Space Sci Rev 216(4):70. https://doi.org/10.1007/s11214-020-00699-2, arXiv:2006.05778 [astro-ph.GA]
- Leidi G, Birke C, Andrassy R, et al (2022) A finite-volume scheme for modeling compressible magnetohydrodynamic flows at low Mach numbers in stellar interiors. Astron Astrophys 668:A143. https://doi.org/10.1051/0004-6361/202244665, arXiv:2210.01641 [astro-ph.SR]

- Lesur GRJ, Baghdadi S, Wafflard-Fernandez G, et al (2023) IDEFIX: A versatile performance-portable Godunov code for astrophysical flows. Astron Astrophys 677:A9. https://doi.org/10.1051/0004-6361/202346005, arXiv:2304.13746 [astro-ph.IM]
- Levermore CD (1984) Relating Eddington factors to flux limiters. J Quant Spectrosc Radiat Transf 31(2):149–160. https://doi.org/10.1016/0022-4073(84)90112-2
- Levermore CD, Pomraning GC (1981) A flux-limited diffusion theory. Astrophys J 248:321–334. https://doi.org/10.1086/159157
- Li P, Cunningham A, Gaches B, et al (2021) ORION2: A magnetohydrodynamics code for star formation. J Open Source Softw 6(68):3771. https://doi.org/10.21105/joss.03771
- Li PS, McKee CF, Klein RI, et al (2008) Sub-Alfvénic Nonideal MHD Turbulence Simulations with Ambipolar Diffusion. I. Turbulence Statistics. Astrophys J 684:380–394. https://doi.org/10.1086/589874, arXiv:0805.0597
- Li PS, Myers A, McKee CF (2012) Ambipolar Diffusion Heating in Turbulent Systems. Astrophys J 760(1):33. https://doi.org/10.1088/0004-637X/760/1/33, arXiv:1210.0700 [astro-ph.SR]
- Li Y, Klessen RS, Mac Low MM (2003) The Formation of Stellar Clusters in Turbulent Molecular Clouds: Effects of the Equation of State. Astrophys J 592:975–985. https://doi.org/10.1086/375780, arXiv:astro-ph/0210479
- Li ZY, Nakamura F (2006) Cluster Formation in Protostellar Outflow-driven Turbulence. Astrophys J Lett 640:L187–L190. https://doi.org/10.1086/503419, astro-ph/0512278
- Lucy LB (1999) Computing radiative equilibria with Monte Carlo techniques. Astron Astrophys 344:282-288
- Mac Low MM (1999) The Energy Dissipation Rate of Supersonic, Magnetohydrodynamic Turbulence in Molecular Clouds. Astrophys J 524:169–178. https://doi.org/10.1086/307784, arXiv:astro-ph/9809177
- Mac Low MM, Klessen RS (2004) Control of star formation by supersonic turbulence. Rev Mod Phys 76(1):125–194. https://doi.org/10.1103/RevModPhys.76.125, arXiv:astro-ph/0301093 [astro-ph]
- Machida MN, Basu S (2019) The First Two Thousand Years of Star Formation. Astrophys J 876(2):149. https://doi.org/10.3847/1538-4357/ab18a7, arXiv:1904.04424 [astro-ph.SR]

- Machida MN, Matsumoto T, Inutsuka S (2008) Magnetohydrodynamics of Population III Star Formation. Astrophys J 685:690–704. https://doi.org/10.1086/591074, arXiv:0803.1224
- Mandal A, Federrath C, Körtgen B (2020) Molecular cloud formation by compression of magnetized turbulent gas subjected to radiative cooling. Mon Not R Astron Soc 493(3):3098–3113. https://doi.org/10.1093/mnras/staa468, arXiv:1910.13762 [astro-ph.GA]
- Mathew SS, Federrath C (2020) Implementation of stellar heating feedback in simulations of star cluster formation: effects on the initial mass function. Mon Not R Astron Soc 496(4):5201–5210. https://doi.org/10.1093/mnras/staa1931, arXiv:2007.01875 [astro-ph.GA]
- Mathew SS, Federrath C (2021) The IMF and multiplicity of stars from gravity, turbulence, magnetic fields, radiation, and outflow feedback. Mon Not R Astron Soc 507(2):2448–2467. https://doi.org/10.1093/mnras/stab2338, arXiv:2106.06521 [astro-ph.GA]
- Mathew SS, Federrath C, Seta A (2023) The role of the turbulence driving mode for the initial mass function. Mon Not R Astron Soc 518(4):5190–5214. https://doi.org/10.1093/mnras/stac3415, arXiv:2208.08802 [astro-ph.GA]
- Mathew SS, Federrath C, Seta A (2025) The influence of the cloud virial parameter on the initial mass function. Mon Not R Astron Soc 536(2):1932–1947. https://doi.org/10.1093/mnras/stae2692, arXiv:2410.13137 [astro-ph.GA]
- Matzner CD, McKee CF (2000) Efficiencies of Low-Mass Star and Star Cluster Formation. Astrophys J 545:364–378. https://doi.org/10.1086/317785, arXiv:astro-ph/0007383
- Mauxion J, Lesur G, Maret S (2024) Modeling the secular evolution of embedded protoplanetary disks. Astron Astrophys 686:A253. https://doi.org/10.1051/0004-6361/202348405, arXiv:2403.16753 [astro-ph.SR]
- Mayer AC, Naab T, Caselli P, et al (2025) Protostellar disks in their natural habitat the formation of protostars and their accretion disks in the turbulent and magnetized interstellar medium. Mon Not R Astron Soc https://doi.org/10.1093/mnras/staf1404, arXiv:2506.14394 [astro-ph.GA]
- Mayer M, Duschl WJ (2005) Rosseland and Planck mean opacities for primordial matter. Mon Not R Astron Soc 358(2):614–631. https://doi.org/10.1111/j.1365-2966. 2005.08826.x, arXiv:astro-ph/0411613 [astro-ph]
- McKee CF, Ostriker EC (2007) Theory of Star Formation. Annu Rev Astron Astrophys 45:565–687. https://doi.org/10.1146/annurev.astro.45.051806.110602, arXiv:0707.3514

- McKee CF, Ostriker JP (1977) A theory of the interstellar medium: three components regulated by supernova explosions in an inhomogeneous substrate. Astrophys J 218:148–169. https://doi.org/10.1086/155667
- Mee AJ, Brandenburg A (2006) Turbulence from localized random expansion waves. Mon Not R Astron Soc 370:415–419. https://doi.org/10.1111/j.1365-2966.2006. 10476.x
- Menon SH, Federrath C, Krumholz MR, et al (2022) VETTAM: a scheme for radiation hydrodynamics with adaptive mesh refinement using the variable Eddington tensor method. Mon Not R Astron Soc 512(1):401–423. https://doi.org/10.1093/mnras/stac485, arXiv:2202.08778 [astro-ph.IM]
- Menon SH, Federrath C, Krumholz MR (2023) Outflows driven by direct and reprocessed radiation pressure in massive star clusters. Mon Not R Astron Soc 521(4):5160–5176. https://doi.org/10.1093/mnras/stad856, arXiv:2210.02818 [astro-ph.GA]
- Mignon-Risse R, González M, Commerçon B, et al (2020) A new hybrid radiative transfer method for massive star formation. Astron Astrophys 635:A42. https://doi.org/10.1051/0004-6361/201936605, arXiv:2001.10886 [astro-ph.IM]
- Mignone A, Bodo G, Vaidya B, et al (2018) A Particle Module for the PLUTO Code. I. An Implementation of the MHD-PIC Equations. Astrophys J 859(1):13. https://doi.org/10.3847/1538-4357/aabccd, arXiv:1804.01946 [astro-ph.HE]
- Mihalas D, Auer L (2001) On laboratory-frame radiation hydrodynamics. J Quant Spectrosc Radiat Transf 71(1):61–97. https://doi.org/10.1016/S0022-4073(01) 00013-9
- Mihalas D, Mihalas BW (1984) Foundations of radiation hydrodynamics. Oxford University Press
- Miyoshi T, Kusano K (2005) A multi-state HLL approximate Riemann solver for ideal magnetohydrodynamics. J Comput Phys 208:315–344. https://doi.org/10.1016/j.jcp.2005.02.017
- Mohapatra R, Federrath C, Sharma P (2022) Multiphase turbulence in galactic haloes: effect of the driving. Mon Not R Astron Soc 514(3):3139–3159. https://doi.org/10.1093/mnras/stac1610, arXiv:2206.03602 [astro-ph.GA]
- Monaghan JJ (1988) An introduction to SPH. Comput Phys Commun 48:89–96. https://doi.org/10.1016/0010-4655(88)90026-4
- Monaghan JJ, Lattanzio JC (1985) A refined particle method for astrophysical problems. Astron Astrophys 149(1):135–143

- Murray SD, Castor JI, Klein RI, et al (1994) Accretion Disk Coronae in High-Luminosity Systems. Astrophys J 435:631. https://doi.org/10.1086/174842, arXiv:astro-ph/9405016 [astro-ph]
- Nakamura F, Li ZY (2007) Protostellar Turbulence Driven by Collimated Outflows. Astrophys J 662:395–412. https://doi.org/10.1086/517515, astro-ph/0703152
- Nakamura F, Li ZY (2011) Clustered Star Formation in Magnetic Clouds: Properties of Dense Cores Formed in Outflow-driven Turbulence. Astrophys J 740:36. https://doi.org/10.1088/0004-637X/740/1/36, arXiv:1107.3616 [astro-ph.SR]
- Nakamura F, Kamada Y, Kamazaki T, et al (2011) The Molecular Outflows in the  $\rho$  Ophiuchi Main Cloud: Implications for Turbulence Generation. Astrophys J 726:46. https://doi.org/10.1088/0004-637X/726/1/46, arXiv:1010.2290 [astro-ph.SR]
- Nakano T, Hasegawa T, Morino JI, et al (2000) Evolution of Protostars Accreting Mass at Very High Rates: Is Orion IRc2 a Huge Protostar? Astrophys J 534:976–983. https://doi.org/10.1086/308765
- Nam DG, Federrath C, Krumholz MR (2021) Testing the turbulent origin of the stellar initial mass function. Mon Not R Astron Soc 503(1):1138–1148. https://doi.org/10.1093/mnras/stab505, arXiv:2102.08564 [astro-ph.GA]
- Noebauer UM, Sim SA (2019) Monte Carlo radiative transfer. Living Rev Comput Astrophys 5:1. https://doi.org/10.1007/s41115-019-0004-9, arXiv:1907.09840 [astro-ph.IM]
- Nordlund Å, Ramsey JP, Popovas A, et al (2018) DISPATCH: a numerical simulation framework for the exa-scale era I. Fundamentals. Mon Not R Astron Soc 477(1):624–638. https://doi.org/10.1093/mnras/sty599, arXiv:1705.10774 [astro-ph.IM]
- Offner SSR, Arce HG (2015) Impact of Winds from Intermediate-mass Stars on Molecular Cloud Structure and Turbulence. Astrophys J 811(2):146. https://doi.org/10.1088/0004-637X/811/2/146, arXiv:1508.07008 [astro-ph.GA]
- Offner SSR, Chaban J (2017) Impact of Protostellar Outflows on Turbulence and Star Formation Efficiency in Magnetized Dense Cores. Astrophys J 847(2):104. https://doi.org/10.3847/1538-4357/aa8996, arXiv:1709.01086 [astro-ph.GA]
- Offner SSR, Liu Y (2018) Turbulent action at a distance due to stellar feedback in magnetized clouds. Nature Astronomy 2:896–900. https://doi.org/10.1038/s41550-018-0566-1, arXiv:1809.03513 [astro-ph.SR]
- Offner SSR, Klein RI, McKee CF, et al (2009) The Effects of Radiative Transfer on Low-Mass Star Formation. Astrophys J 703:131–149. https://doi.org/10.1088/0004-637X/703/1/131, arXiv:0904.2004 [astro-ph.SR]

- Offner SSR, Kratter KM, Matzner CD, et al (2010) The Formation of Low-mass Binary Star Systems Via Turbulent Fragmentation. Astrophys J 725(2):1485–1494. https://doi.org/10.1088/0004-637X/725/2/1485, arXiv:1010.3702 [astro-ph.SR]
- Offner SSR, Robitaille TP, Hansen CE, et al (2012) Observing Simulated Protostars with Outflows: How Accurate Are Protostellar Properties Inferred from SEDs? Astrophys J 753:98. https://doi.org/10.1088/0004-637X/753/2/98, arXiv:1205.0246 [astro-ph.SR]
- Omukai K, Tsuribe T, Schneider R, et al (2005) Thermal and Fragmentation Properties of Star-forming Clouds in Low-Metallicity Environments. Astrophys J 626:627–643. https://doi.org/10.1086/429955, arXiv:astro-ph/0503010
- Osterbrock DE, Ferland GJ (2006) Astrophysics of gaseous nebulae and active galactic nuclei. University Science Books
- Owen ER, On AYL, Lai SP, et al (2021) Observational Signatures of Cosmic-Ray Interactions in Molecular Clouds. Astrophys J 913(1):52. https://doi.org/10.3847/1538-4357/abee1a, arXiv:2103.06542 [astro-ph.GA]
- Padoan P, Nordlund Å (2002) The Stellar Initial Mass Function from Turbulent Fragmentation. Astrophys J 576:870–879. https://doi.org/10.1086/341790
- Padoan P, Nordlund Å (2011) The Star Formation Rate of Supersonic Magnetohydrodynamic Turbulence. Astrophys J 730(1):40. https://doi.org/10.1088/0004-637X/730/1/40, arXiv:0907.0248 [astro-ph.GA]
- Padoan P, Federrath C, Chabrier G, et al (2014) The Star Formation Rate of Molecular Clouds. In: Beuther H, Klessen RS, Dullemond CP, et al (eds) Protostars and Planets VI. University of Arizona Press, pp 77–100, https://doi.org/10.2458/azu-uapress\_9780816531240-ch004, arXiv:1312.5365
- Padoan P, Pan L, Haugbølle T, et al (2016) Supernova Driving. I. The Origin of Molecular Cloud Turbulence. Astrophys J 822:11. https://doi.org/10.3847/0004-637X/822/1/11, arXiv:1509.04663
- Padovani M, Ivlev AV, Galli D, et al (2020) Impact of Low-Energy Cosmic Rays on Star Formation. Space Sci Rev 216(2):29. https://doi.org/10.1007/s11214-020-00654-1, arXiv:2002.10282 [astro-ph.GA]
- Pan L, Padoan P, Haugbølle T, et al (2016) Supernova Driving. II. Compressive Ratio in Molecular-cloud Turbulence. Astrophys J 825:30. https://doi.org/10.3847/0004-637X/825/1/30, arXiv:1510.04742
- Pandey P, Lenker SCII, Lopez LA, et al (2025) Explosive Dispersal Outflows as a New Class of Fermi Gamma-Ray Sources: The Case of DR21. arXiv e-prints arXiv:2509.02679. https://doi.org/10.48550/arXiv.2509.02679, arXiv:2509.02679

- [astro-ph.HE]
- Passot T, Vázquez-Semadeni E (1998) Density probability distribution in one-dimensional polytropic gas dynamics. Phys Rev Lett 58(4):4501–4510. https://doi.org/10.1103/PhysRevE.58.4501, arXiv:physics/9802019 [physics.flu-dyn]
- Pavlovski G, Smith MD, Mac Low MM (2006) Hydrodynamical simulations of the decay of high-speed molecular turbulence II. Divergence from isothermality. Mon Not R Astron Soc 368:943–958. https://doi.org/10.1111/j.1365-2966.2006.10172.x, arXiv:astro-ph/0504504
- Pelletier G, Pudritz RE (1992) Hydromagnetic disk winds in young stellar objects and active galactic nuclei. Astrophys J 394:117–138. https://doi.org/10.1086/171565
- Pencil Code Collaboration, Brandenburg A, Johansen A, et al (2021) The Pencil Code, a modular MPI code for partial differential equations and particles: multipurpose and multiuser-maintained. J Open Source Softw 6(58):2807. https://doi.org/10.21105/joss.02807, arXiv:2009.08231 [astro-ph.IM]
- Peters T, Banerjee R, Klessen RS, et al (2010) H II Regions: Witnesses to Massive Star Formation. Astrophys J 711:1017–1028. https://doi.org/10.1088/0004-637X/711/2/1017, arXiv:1001.2470
- Petkova MA, Vandenbroucke B, Bonnell IA, et al (2021) Modelling of ionizing feedback with smoothed particle hydrodynamics and Monte Carlo radiative transfer on a Voronoi grid. Mon Not R Astron Soc 507(1):858–878. https://doi.org/10.1093/mnras/stab2178, arXiv:2109.13953 [astro-ph.GA]
- Pillsworth R, Roscoe E, Pudritz RE, et al (2025) Filamentary Hierarchies and Superbubbles. I. Characterizing Filament Properties across a Simulated Spiral Galaxy. Astrophys J 987(1):20. https://doi.org/10.3847/1538-4357/add68a, arXiv:2504.01099 [astro-ph.GA]
- Pineda JE, Sipilä O, Segura-Cox DM, et al (2024) Probing the physics of star formation (ProPStar). I. First resolved maps of the electron fraction and cosmic-ray ionization rate in NGC 1333. Astron Astrophys 686:A162. https://doi.org/10.1051/0004-6361/202347997, arXiv:2402.16202 [astro-ph.GA]
- Price DJ, Federrath C (2010) A comparison between grid and particle methods on the statistics of driven, supersonic, isothermal turbulence. Mon Not R Astron Soc 406:1659–1674. https://doi.org/10.1111/j.1365-2966.2010.16810.x [astro-ph.GA]
- Price DJ, Monaghan JJ (2007) An energy-conserving formalism for adaptive gravitational force softening in smoothed particle hydrodynamics and N-body codes. Mon Not R Astron Soc 374:1347–1358. https://doi.org/10.1111/j.1365-2966.2006.11241.x, arXiv:astro-ph/0610872

- Price DJ, Wurster J, Tricco TS, et al (2018) Phantom: A Smoothed Particle Hydrodynamics and Magnetohydrodynamics Code for Astrophysics. Publ Astron Soc Australia 35:e031. https://doi.org/10.1017/pasa.2018.25, arXiv:1702.03930 [astro-ph.IM]
- Pudritz RE, Norman CA (1986) Bipolar hydromagnetic winds from disks around protostellar objects. Astrophys J 301:571–586. https://doi.org/10.1086/163924
- Pudritz RE, Ouyed R, Fendt C, et al (2007) Disk Winds, Jets, and Outflows: Theoretical and Computational Foundations. Protostars and Planets V pp 277–294. arXiv:astro-ph/0603592
- Raskutti S, Ostriker EC, Skinner MA (2016) Numerical Simulations of Turbulent Molecular Clouds Regulated by Radiation Feedback Forces. I. Star Formation Rate and Efficiency. Astrophys J 829(2):130. https://doi.org/10.3847/0004-637X/829/2/130, arXiv:1608.04469 [astro-ph.GA]
- Raskutti S, Ostriker EC, Skinner MA (2017) Numerical Simulations of Turbulent Molecular Clouds Regulated by Radiation Feedback Forces. II. Radiation-Gas Interactions and Outflows. Astrophys J 850(2):112. https://doi.org/10.3847/1538-4357/aa965e, arXiv:1711.06737 [astro-ph.GA]
- Reissl S, Wolf S, Brauer R (2016) Radiative transfer with POLARIS. I. Analysis of magnetic fields through synthetic dust continuum polarization measurements. Astron Astrophys 593:A87. https://doi.org/10.1051/0004-6361/201424930, arXiv:1604.05305 [astro-ph.IM]
- Ricker PM (2008) A Direct Multigrid Poisson Solver for Oct-Tree Adaptive Meshes. Astrophys J Suppl 176:293–300. https://doi.org/10.1086/526425, arXiv:0710.4397
- Rijkhorst EJ, Plewa T, Dubey A, et al (2006) Hybrid characteristics: 3D radiative transfer for parallel adaptive mesh refinement hydrodynamics. Astron Astrophys 452(3):907–920. https://doi.org/10.1051/0004-6361:20053401, arXiv:astro-ph/0505213 [astro-ph]
- Rincon F, Califano F, Schekochihin AA, et al (2016) Turbulent dynamo in a collisionless plasma. Proc Natl Acad Sci 113(15):3950–3953. https://doi.org/10.1073/pnas. 1525194113, arXiv:1512.06455 [astro-ph.CO]
- Robitaille TP (2011) HYPERION: an open-source parallelized three-dimensional dust continuum radiative transfer code. Astron Astrophys 536:A79. https://doi.org/10.1051/0004-6361/201117150, arXiv:1112.1071 [astro-ph.IM]
- Rodríguez-Kamenetzky A, Carrasco-González C, Araudo A, et al (2017) The Highly Collimated Radio Jet of HH 80-81: Structure and Nonthermal Emission. Astrophys J 851(1):16. https://doi.org/10.3847/1538-4357/aa9895, arXiv:1711.02554 [astro-ph.HE]

- Rogers H, Pittard JM (2013) Feedback from winds and supernovae in massive stellar clusters I. Hydrodynamics. Mon Not R Astron Soc 431(2):1337–1351. https://doi.org/10.1093/mnras/stt255, arXiv:1302.2443 [astro-ph.SR]
- Rosdahl J, Teyssier R (2015) A scheme for radiation pressure and photon diffusion with the M1 closure in RAMSES-RT. Mon Not R Astron Soc 449(4):4380–4403. https://doi.org/10.1093/mnras/stv567, arXiv:1411.6440 [astro-ph.IM]
- Rosdahl J, Blaizot J, Aubert D, et al (2013) RAMSES-RT: radiation hydrodynamics in the cosmological context. Mon Not R Astron Soc 436(3):2188–2231. https://doi.org/10.1093/mnras/stt1722, arXiv:1304.7126 [astro-ph.CO]
- Rosen AL, Krumholz MR, McKee CF, et al (2016) An unstable truth: how massive stars get their mass. Mon Not R Astron Soc 463(3):2553–2573. https://doi.org/10.1093/mnras/stw2153, arXiv:1607.03117 [astro-ph.SR]
- Rosen AL, Krumholz MR, Oishi JS, et al (2017) Hybrid Adaptive Ray-Moment Method (HARM<sup>2</sup>): A highly parallel method for radiation hydrodynamics on adaptive grids. J Comput Phys 330:924–942. https://doi.org/10.1016/j.jcp.2016.10.048, arXiv:1607.01802 [astro-ph.IM]
- Rosen AL, Li PS, Zhang Q, et al (2019) Massive-star Formation via the Collapse of Subvirial and Virialized Turbulent Massive Cores. Astrophys J 887(2):108. https://doi.org/10.3847/1538-4357/ab54c6, arXiv:1902.10153 [astro-ph.SR]
- Rosen AL, Offner SSR, Sadavoy SI, et al (2020) Zooming in on Individual Star Formation: Low- and High-Mass Stars. Space Sci Rev 216(4):62. https://doi.org/10.1007/s11214-020-00688-5, arXiv:2005.07717 [astro-ph.SR]
- Rudd DH, Zentner AR, Kravtsov AV (2008) Effects of Baryons and Dissipation on the Matter Power Spectrum. Astrophys J 672(1):19–32. https://doi.org/10.1086/523836, arXiv:astro-ph/0703741 [astro-ph]
- Ruszkowski M, Pfrommer C (2023) Cosmic ray feedback in galaxies and galaxy clusters. Astron Astrophys Rev 31(1):4. https://doi.org/10.1007/s00159-023-00149-2, arXiv:2306.03141 [astro-ph.HE]
- Ruszkowski M, Yang HYK, Zweibel E (2017) Global Simulations of Galactic Winds Including Cosmic-ray Streaming. Astrophys J 834(2):208. https://doi.org/10.3847/1538-4357/834/2/208, arXiv:1602.04856 [astro-ph.GA]
- Salem M, Bryan GL (2014) Cosmic ray driven outflows in global galaxy disc models. Mon Not R Astron Soc 437(4):3312–3330. https://doi.org/10.1093/mnras/stt2121, arXiv:1307.6215 [astro-ph.CO]
- Salpeter EE (1955) The Luminosity Function and Stellar Evolution. Astrophys J 121:161. https://doi.org/10.1086/145971

- Scalo J, Elmegreen BG (2004) Interstellar Turbulence II: Implications and Effects. Annu Rev Astron Astrophys 42(1):275–316. https://doi.org/10.1146/annurev.astro. 42.120403.143327, arXiv:astro-ph/0404452 [astro-ph]
- Schekochihin AA, Cowley SC, Taylor SF, et al (2004) Simulations of the Small-Scale Turbulent Dynamo. Astrophys J 612(1):276–307. https://doi.org/10.1086/422547, arXiv:astro-ph/0312046 [astro-ph]
- Schekochihin AA, Iskakov AB, Cowley SC, et al (2007) Fluctuation dynamo and turbulent induction at low magnetic Prandtl numbers. New J Phys 9:300. https://doi.org/10.1088/1367-2630/9/8/300 [physics.flu-dyn]
- Schlickeiser R (1989) Cosmic-Ray Transport and Acceleration. I. Derivation of the Kinetic Equation and Application to Cosmic Rays in Static Cold Media. Astrophys J 336:243. https://doi.org/10.1086/167009
- Schlickeiser R, Lerche I (1985) Cosmic gas dynamics. I Basic equations and the dynamics of hot interstellar matter. Astron Astrophys 151(1):151–156
- Schmidt W, Federrath C, Hupp M, et al (2009) Numerical simulations of compressively driven interstellar turbulence. I. Isothermal gas. Astron Astrophys 494(1):127–145. https://doi.org/10.1051/0004-6361:200809967, arXiv:0809.1321 [astro-ph]
- Sedov LI (1959) Similarity and Dimensional Methods in Mechanics. New York: Academic Press
- Seifried D, Pudritz RE, Banerjee R, et al (2012) Magnetic fields during the early stages of massive star formation II. A generalized outflow criterion. Mon Not R Astron Soc 422:347–366. https://doi.org/10.1111/j.1365-2966.2012.20610.x, arXiv:1109.4379 [astro-ph.SR]
- Seifried D, Walch S, Girichidis P, et al (2017) SILCC-Zoom: the dynamic and chemical evolution of molecular clouds. Mon Not R Astron Soc 472(4):4797–4818. https://doi.org/10.1093/mnras/stx2343, arXiv:1704.06487 [astro-ph.GA]
- Semenov D, Henning T, Helling C, et al (2003) Rosseland and Planck mean opacities for protoplanetary discs. Astron Astrophys 410:611–621. https://doi.org/10.1051/0004-6361:20031279, arXiv:astro-ph/0308344 [astro-ph]
- Semenov VA (2024) Capturing Turbulence with Numerical Dissipation: a Simple Dynamical Model for Unresolved Turbulence in Hydrodynamic Simulations. arXiv e-prints arXiv:2410.23339. https://doi.org/10.48550/arXiv.2410.23339, arXiv:2410.23339 [astro-ph.GA]
- Semenov VA, Kravtsov AV, Gnedin NY (2016) Nonuniversal Star Formation Efficiency in Turbulent ISM. Astrophys J 826(2):200. https://doi.org/10.3847/0004-637X/826/2/200, arXiv:1512.03101 [astro-ph.GA]

- Seta A, Federrath C (2021) Saturation mechanism of the fluctuation dynamo in supersonic turbulent plasmas. Phys Rev Fluids 6(10):103701. https://doi.org/10.1103/PhysRevFluids.6.103701, arXiv:2109.11698 [astro-ph.GA]
- Seta A, Federrath C (2022) Turbulent dynamo in the two-phase interstellar medium. Mon Not R Astron Soc 514(1):957–976. https://doi.org/10.1093/mnras/stac1400, arXiv:2202.08324 [astro-ph.GA]
- Sharda P, Menon SH (2025) Population III star formation in the presence of turbulence, magnetic fields, and ionizing radiation feedback. Mon Not R Astron Soc 540(2):1745–1764. https://doi.org/10.1093/mnras/staf803, arXiv:2405.18265 [astro-ph.GA]
- Sharda P, Krumholz MR, Federrath C (2019) The role of the H<sub>2</sub> adiabatic index in the formation of the first stars. Mon Not R Astron Soc 490(1):513–526. https://doi.org/10.1093/mnras/stz2618, arXiv:1909.06269 [astro-ph.GA]
- Shestakov AI, Offner SSR (2008) A multigroup diffusion solver using pseudo transient continuation for a radiation-hydrodynamic code with patch-based AMR. J Comput Phys 227(3):2154–2186. https://doi.org/10.1016/j.jcp.2007.09.019, arXiv:0710.4509 [astro-ph]
- Shibata K, Uchida Y (1985) A magnetodynamic mechanism for the formation of astrophysical jets. I Dynamical effects of the relaxation of nonlinear magnetic twists. Publ Astron Soc Japan 37:31–46
- Shibata K, Uchida Y (1986) A magnetodynamic mechanism for the formation of astrophysical jets. II Dynamical processes in the accretion of magnetized mass in rotation. Publ Astron Soc Japan 38:631–660
- Shivakumar LM, Federrath C (2025) Numerical viscosity and resistivity in MHD turbulence simulations. Mon Not R Astron Soc 537(4):2961–2986. https://doi.org/10.1093/mnras/staf160, arXiv:2311.10350 [astro-ph.SR]
- Shu FH, Adams FC, Lizano S (1987) Star formation in molecular clouds Observation and theory. Annu Rev Astron Astrophys 25:23–81. https://doi.org/10.1146/annurev.aa.25.090187.000323
- Skilling J (1975) Cosmic ray streaming I. Effect of Alfvén waves on particles. Mon Not R Astron Soc 172:557–566. https://doi.org/10.1093/mnras/172.3.557
- Skinner MA, Ostriker EC (2013) A Two-moment Radiation Hydrodynamics Module in Athena Using a Time-explicit Godunov Method. Astrophys J Suppl 206(2):21. https://doi.org/10.1088/0067-0049/206/2/21, arXiv:1306.0010 [astro-ph.IM]
- Skinner MA, Ostriker EC (2015) Numerical Simulations of Turbulent Molecular Clouds Regulated by Reprocessed Radiation Feedback from Nascent Super Star

- Clusters. Astrophys J 809(2):187. https://doi.org/10.1088/0004-637X/809/2/187, arXiv:1507.06366 [astro-ph.GA]
- Smith A, Kannan R, Tsang BTH, et al (2020) AREPO-MCRT: Monte Carlo Radiation Hydrodynamics on a Moving Mesh. Astrophys J 905(1):27. https://doi.org/10.3847/1538-4357/abc47e, arXiv:2008.01750 [astro-ph.GA]
- Smith N (2014) Mass Loss: Its Effect on the Evolution and Fate of High-Mass Stars. Annu Rev Astron Astrophys 52:487–528. https://doi.org/10.1146/annurev-astro-081913-040025, arXiv:1402.1237 [astro-ph.SR]
- Springel V (2005) The cosmological simulation code GADGET-2. Mon Not R Astron Soc 364(4):1105–1134. https://doi.org/10.1111/j.1365-2966.2005.09655.x, arXiv:astro-ph/0505010 [astro-ph]
- Springel V (2010) E pur si muove: Galilean-invariant cosmological hydrodynamical simulations on a moving mesh. Mon Not R Astron Soc 401:791–851. https://doi.org/10.1111/j.1365-2966.2009.15715.x, arXiv:0901.4107 [astro-ph.CO]
- St-Onge DA, Kunz MW (2018) Fluctuation Dynamo in a Collisionless, Weakly Magnetized Plasma. Astrophys J Lett 863(2):L25. https://doi.org/10.3847/2041-8213/aad638, arXiv:1806.11162 [astro-ph.HE]
- Stamatellos D, Whitworth AP, Hubber DA (2012) Episodic accretion, protostellar radiative feedback, and their role in low-mass star formation. Mon Not R Astron Soc 427(2):1182–1193. https://doi.org/10.1111/j.1365-2966.2012.22038.x, arXiv:1209.0765 [astro-ph.GA]
- Stone JM, Norman ML (1992) ZEUS-2D: A radiation magnetohydrodynamics code for astrophysical flows in two space dimensions. I The hydrodynamic algorithms and tests. Astrophys J Suppl 80:753–790. https://doi.org/10.1086/191680
- Stone JM, Ostriker EC, Gammie CF (1998) Dissipation in Compressible Magnetohydrodynamic Turbulence. Astrophys J Lett 508:L99–L102. https://doi.org/10.1086/311718, arXiv:astro-ph/9809357
- Stone JM, Tomida K, White CJ, et al (2020) The Athena++ Adaptive Mesh Refinement Framework: Design and Magnetohydrodynamic Solvers. Astrophys J Suppl 249(1):4. https://doi.org/10.3847/1538-4365/ab929b, arXiv:2005.06651 [astro-ph.IM]
- Stone JM, Mullen PD, Fielding D, et al (2024) AthenaK: A Performance-Portable Version of the Athena++ AMR Framework. Astrophys J Suppl arXiv:2409.16053. https://doi.org/10.48550/arXiv.2409.16053, submitted, arXiv:2409.16053 [astro-ph.IM]

- Strong AW, Moskalenko IV (1998) Propagation of Cosmic-Ray Nucleons in the Galaxy. Astrophys J 509(1):212–228. https://doi.org/10.1086/306470, arXiv:astro-ph/9807150 [astro-ph]
- Sur S, Schleicher DRG, Banerjee R, et al (2010) The Generation of Strong Magnetic Fields During the Formation of the First Stars. Astrophys J Lett 721:L134–L138. https://doi.org/10.1088/2041-8205/721/2/L134 [astro-ph.CO]
- Tamburro D, Rix HW, Leroy AK, et al (2009) What is Driving the HI Velocity Dispersion? Astron J 137:4424–4435. https://doi.org/10.1088/0004-6256/137/5/4424, arXiv:0903.0183
- Taylor G (1950) The Formation of a Blast Wave by a Very Intense Explosion. I. Theoretical Discussion. Proc R Soc London Ser A 201(1065):159–174. https://doi.org/10.1098/rspa.1950.0049
- Teyssier R (2002) Cosmological hydrodynamics with adaptive mesh refinement. A new high resolution code called RAMSES. Astron Astrophys 385:337–364. https://doi.org/10.1051/0004-6361:20011817, arXiv:astro-ph/0111367 [astro-ph]
- Teyssier R, Commerçon B (2019) Numerical Methods for Simulating Star Formation. Front Astron Space Sci 6:51. https://doi.org/10.3389/fspas.2019.00051, arXiv:1907.08542 [astro-ph.IM]
- Thomas T, Pfrommer C (2019) Cosmic-ray hydrodynamics: Alfvén-wave regulated transport of cosmic rays. Mon Not R Astron Soc 485(3):2977–3008. https://doi.org/10.1093/mnras/stz263, arXiv:1805.11092 [astro-ph.HE]
- Thomas T, Pfrommer C (2022) Comparing different closure relations for cosmic ray hydrodynamics. Mon Not R Astron Soc 509(4):4803–4816. https://doi.org/10.1093/mnras/stab3079, arXiv:2105.08090 [astro-ph.HE]
- Thomas T, Pfrommer C, Pakmor R (2021) A finite volume method for two-moment cosmic ray hydrodynamics on a moving mesh. Mon Not R Astron Soc 503(2):2242–2264. https://doi.org/10.1093/mnras/stab397, arXiv:2010.11960 [astro-ph.HE]
- Tisza L (1942) Supersonic Absorption and Stokes' Viscosity Relation. Phys Rev 61:531–536. https://doi.org/10.1103/PhysRev.61.531
- Tomida K, Tomisaka K, Matsumoto T, et al (2013) Radiation Magnetohydrodynamic Simulations of Protostellar Collapse: Protostellar Core Formation. Astrophys J 763(1):6. https://doi.org/10.1088/0004-637X/763/1/6, arXiv:1206.3567 [astro-ph.SR]
- Tritsis A, Federrath C, Willacy K, et al (2022) Non-ideal magnetohydrodynamic simulations of subcritical pre-stellar cores with non-equilibrium chemistry. Mon Not R Astron Soc 510(3):4420–4435. https://doi.org/10.1093/mnras/stab3740,

- arXiv:2112.11462 [astro-ph.GA]
- Tritsis A, Basu S, Federrath C (2025a) Projection-angle effects when "observing" a turbulent magnetized collapsing molecular cloud: I. Chemistry and line transfer. Astron Astrophys 695:A18. https://doi.org/10.1051/0004-6361/202452013, arXiv:2503.01963 [astro-ph.GA]
- Tritsis A, Basu S, Federrath C (2025b) Projection-angle effects when "observing" a turbulent magnetized collapsing molecular cloud: II. Magnetic field. Astron Astrophys 696:A35. https://doi.org/10.1051/0004-6361/202453265
- Troccoli E, Federrath C (2025) The statistics and structure of dissipation in subsonic and supersonic turbulence. Mon Not R Astron Soc
- Trottenberg U, Oosterlee CW, Schüller A (2001) Multigrid, Texts in Applied Mathematics. Bd., vol 33. Academic Press, with contributions by A. Brandt, P. Oswald and K. Stüben
- Truelove JK, Klein RI, McKee CF, et al (1997) The Jeans Condition: A New Constraint on Spatial Resolution in Simulations of Isothermal Self-gravitational Hydrodynamics. Astrophys J Lett 489:L179. https://doi.org/10.1086/316779
- Tsang BTH, Milosavljević M (2015) Radiation pressure driving of a dusty atmosphere. Mon Not R Astron Soc 453(1):1108–1120. https://doi.org/10.1093/mnras/stv1707, arXiv:1506.05121 [astro-ph.GA]
- Turk MJ, Abel T, O'Shea B (2009) The Formation of Population III Binaries from Cosmological Initial Conditions. Science 325(5940):601. https://doi.org/10.1126/science.1173540, arXiv:0907.2919 [astro-ph.CO]
- Turk MJ, Oishi JS, Abel T, et al (2012) Magnetic Fields in Population III Star Formation. Astrophys J 745:154. https://doi.org/10.1088/0004-637X/745/2/154, arXiv:1112.4479 [astro-ph.CO]
- Uchida Y, Shibata K (1985) Magnetodynamical acceleration of CO and optical bipolar flows from the region of star formation. Publ Astron Soc Japan 37:515–535
- Vandenbroucke B, Wood K (2018) The Monte Carlo photoionization and movingmesh radiation hydrodynamics code CMACIONIZE. Astronomy and Computing 23:40. https://doi.org/10.1016/j.ascom.2018.02.005
- Vázquez-Semadeni E, Ballesteros-Paredes J, Klessen RS (2003) A Holistic Scenario of Turbulent Molecular Cloud Evolution and Control of the Star Formation Efficiency: First Tests. Astrophys J Lett 585:L131–L134. https://doi.org/10.1086/374325, arXiv:astro-ph/0301546

- Vázquez-Semadeni E, Gómez GC, Jappsen AK, et al (2007) Molecular Cloud Evolution. II. From Cloud Formation to the Early Stages of Star Formation in Decaying Conditions. Astrophys J 657(2):870–883. https://doi.org/10.1086/510771, arXiv:astro-ph/0608375 [astro-ph]
- Vázquez-Semadeni E, Palau A, Ballesteros-Paredes J, et al (2019) Global hierarchical collapse in molecular clouds. Towards a comprehensive scenario. Mon Not R Astron Soc 490(3):3061–3097. https://doi.org/10.1093/mnras/stz2736, arXiv:1903.11247 [astro-ph.GA]
- Verliat A, Hennebelle P, González M, et al (2022) Influence of protostellar jets and HII regions on the formation and evolution of stellar clusters. Astron Astrophys 663:A6. https://doi.org/10.1051/0004-6361/202141765, arXiv:2202.02237 [astro-ph.GA]
- Verner DA, Ferland GJ, Korista KT, et al (1996) Atomic Data for Astrophysics. II. New Analytic Fits for Photoionization Cross Sections of Atoms and Ions. Astrophys J 465:487. https://doi.org/10.1086/177435, arXiv:astro-ph/9601009 [astro-ph]
- Waagan K, Federrath C, Klingenberg C (2011) A robust numerical scheme for highly compressible magnetohydrodynamics: Nonlinear stability, implementation and tests. J Comput Phys 230:3331–3351. https://doi.org/10.1016/j.jcp.2011.01.026 [astro-ph.IM]
- Walch S, Naab T (2015) The energy and momentum input of supernova explosions in structured and ionized molecular clouds. Mon Not R Astron Soc 451(3):2757–2771. https://doi.org/10.1093/mnras/stv1155, arXiv:1410.0011 [astro-ph.GA]
- Walch S, Whitworth AP, Girichidis P (2012) The influence of the turbulent perturbation scale on pre-stellar core fragmentation and disc formation. Mon Not R Astron Soc 419:760–770. https://doi.org/10.1111/j.1365-2966.2011.19741.x, arXiv:1109.0280 [astro-ph.GA]
- Wang P, Li ZY, Abel T, et al (2010) Outflow Feedback Regulated Massive Star Formation in Parsec-Scale Cluster-Forming Clumps. Astrophys J 709:27–41. https://doi.org/10.1088/0004-637X/709/1/27, arXiv:0908.4129 [astro-ph.SR]
- Wardle M, Königl A (1993) The structure of protostellar accretion disks and the origin of bipolar flows. Astrophys J 410:218–238. https://doi.org/10.1086/172739
- Watt J, Federrath C, Birke C, et al (2025) Mitigating numerical dissipation in simulations of subsonic turbulent flows. Mon Not R Astron Soc
- Weaver R, McCray R, Castor J, et al (1977) Interstellar bubbles. II. Structure and evolution. Astrophys J 218:377–395. https://doi.org/10.1086/155692
- Wibking BD, Krumholz MR (2022) QUOKKA: a code for two-moment AMR radiation hydrodynamics on GPUs. Mon Not R Astron Soc 512(1):1430–1449. https://doi.

- Winner G, Pfrommer C, Girichidis P, et al (2019) Evolution of cosmic ray electron spectra in magnetohydrodynamical simulations. Mon Not R Astron Soc 488(2):2235–2252. https://doi.org/10.1093/mnras/stz1792, arXiv:1903.01467 [astro-ph.HE]
- Wise JH, Abel T (2011) ENZO+MORAY: radiation hydrodynamics adaptive mesh refinement simulations with adaptive ray tracing. Mon Not R Astron Soc 414(4):3458-3491. https://doi.org/10.1111/j.1365-2966.2011.18646.x, arXiv:1012.2865 [astro-ph.IM]
- Wolfire MG, Hollenbach D, McKee CF, et al (1995) The neutral atomic phases of the interstellar medium. Astrophys J 443:152–168. https://doi.org/10.1086/175510
- Wünsch R (2024) Radiation transport methods in star formation simulations. Frontiers in Astronomy and Space Sciences 11:1346812. https://doi.org/10.3389/fspas. 2024.1346812, arXiv:2403.05410 [astro-ph.IM]
- Wünsch R, Walch S, Dinnbier F, et al (2018) Tree-based solvers for adaptive mesh refinement code FLASH I: gravity and optical depths. Mon Not R Astron Soc 475(3):3393–3418. https://doi.org/10.1093/mnras/sty015, arXiv:1708.06142 [astro-ph.IM]
- Wünsch R, Walch S, Dinnbier F, et al (2021) Tree-based solvers for adaptive mesh refinement code FLASH II: radiation transport module TreeRay. Mon Not R Astron Soc 505(3):3730–3754. https://doi.org/10.1093/mnras/stab1482, arXiv:2105.09644 [astro-ph.IM]
- Xu G (1995) A New Parallel N-Body Gravity Solver: TPM. Astrophys J Suppl 98:355. https://doi.org/10.1086/192166, arXiv:astro-ph/9409021 [astro-ph]
- Xu S, Lazarian A (2022) Shock Acceleration with Oblique and Turbulent Magnetic Fields. Astrophys J 925(1):48. https://doi.org/10.3847/1538-4357/ac3824, arXiv:2111.04759 [astro-ph.HE]
- Xu W, Kunz MW (2021a) Formation and evolution of protostellar accretion discs I. Angular-momentum budget, gravitational self-regulation, and numerical convergence. Mon Not R Astron Soc 502(4):4911–4929. https://doi.org/10.1093/mnras/stab314, arXiv:2101.00131 [astro-ph.SR]
- Xu W, Kunz MW (2021b) Formation and evolution of protostellar accretion discs II. From 3D simulation to a simple semi-analytic model of Class 0/I discs. Mon Not R Astron Soc 508(2):2142–2168. https://doi.org/10.1093/mnras/stab2715, arXiv:2109.07535 [astro-ph.SR]

- Yan H, Lazarian A (2004) Cosmic-Ray Scattering and Streaming in Compressible Magnetohydrodynamic Turbulence. Astrophys J 614(2):757–769. https://doi.org/10.1086/423733, arXiv:astro-ph/0408172 [astro-ph]
- Yang TQ, Federrath C (2025) Protostellar disc structure and dynamics during star formation from cloud-scale initial conditions. Mon Not R Astron Soc 541(2):1969–1987. https://doi.org/10.1093/mnras/staf1088, arXiv:2501.07626 [astro-ph.SR]
- Zamora-Avilés M, Vázquez-Semadeni E (2014) An Evolutionary Model for Collapsing Molecular Clouds and their Star Formation Activity. II. Mass Dependence of the Star Formation Rate. Astrophys J 793(2):84. https://doi.org/10.1088/0004-637X/793/2/84, arXiv:1308.4918 [astro-ph.SR]
- Zhang C, Xu S (2023) Numerical Testing of Mirror Diffusion of Cosmic Rays. Astrophys J Lett 959(1):L8. https://doi.org/10.3847/2041-8213/ad0fe5, arXiv:2311.18001 [astro-ph.HE]
- Zhang W, Almgren A, Beckner V, et al (2019) AMReX: a framework for block-structured adaptive mesh refinement. J Open Source Softw 4(37):1370. https://doi.org/10.21105/joss.01370
- Zhao B, Tomida K, Hennebelle P, et al (2020) Formation and Evolution of Disks Around Young Stellar Objects. Space Sci Rev 216(3):43. https://doi.org/10.1007/s11214-020-00664-z, arXiv:2004.01342 [astro-ph.SR]
- Zhao B, Pudritz RE, Pillsworth R, et al (2024) Filamentary Hierarchies and Superbubbles: Galactic Multiscale Magnetohydrodynamic Simulations of Giant Molecular Cloud to Star Cluster Formation. Astrophys J 974(2):240. https://doi.org/10.3847/1538-4357/ad67e2, arXiv:2405.18474 [astro-ph.GA]
- Zhao X, Bai XN, Ostriker EC (2025) Cosmic Ray Magnetohydrodynamics: A New Two-Moment Framework with Numerical Implementation. arXiv e-prints arXiv:2509.04387. https://doi.org/10.48550/arXiv.2509.04387, arXiv:2509.04387 [astro-ph.HE]
- Ziegler U (2008) The NIRVANA code: Parallel computational MHD with adaptive mesh refinement. Comput Phys Commun 179(4):227–244. https://doi.org/10.1016/j.cpc.2008.02.017
- Zier O, Kannan R, Smith A, et al (2024) Adapting AREPO-RT for exascale computing: GPU acceleration and efficient communication. Mon Not R Astron Soc 533(1):268–286. https://doi.org/10.1093/mnras/stae1837, arXiv:2404.17630 [astro-ph.IM]
- Zinnecker H, Yorke HW (2007) Toward Understanding Massive Star Formation. Annu Rev Astron Astrophys 45:481–563. https://doi.org/10.1146/annurev.astro.44. 051905.092549, arXiv:0707.1279

Zweibel EG (2013) The microphysics and macrophysics of cosmic rays. Phys Plasmas 20(5):055501. https://doi.org/10.1063/1.4807033

Zweibel EG (2017) The basis for cosmic ray feedback: Written on the wind. Phys Plasmas 24(5):055402. https://doi.org/10.1063/1.4984017